ENVIRONMENTAL DEPENDENCE OF MASS-DIMENSION RELATIONSHIPS AND INVESTIGATION OF MICROPHYSICAL OBSERVATIONS OF A SOUTHERN HEMISPHERE ATMOSPHERIC RIVER

BY

JOSEPH A. FINLON

DISSERTATION

Submitted in partial fulfillment of the requirements
for the degree of Doctor of Philosophy in Atmospheric Sciences
in the Graduate College of the
University of Illinois at Urbana-Champaign, 2019

Urbana, Illinois

Doctoral Committee:

Professor Robert Rauber, Co-Chair
Professor Greg McFarquhar, University of Oklahoma, Co-Chair
Associate Professor Stephen Nesbitt
Professor Sonia Lasher-Trapp

Abstract

Ice microphysical processes have a profound impact on the weather and climate given their ability to change radiative, thermodynamic, and precipitation properties. Their representation in models and remote sensing retrievals, however, is highly uncertain given the variable nature of ice particle properties, even in similar environmental conditions, that are typically held constant or represented as a simple function of environmental variables in models. Further, microphysical measurements through clouds, which can provide the basis for assumptions made within models and remote sensing retrievals, can also contain uncertainties based on the statistical counting of particles and uncertainties in the measurements themselves.

To improve how empirical parameters characterizing ice microphysical properties can be represented in models or retrieval schemes, a technique was developed that considers multiple coefficients from a mass-dimension (m-D) relationship as equally plausible solutions for a given environment. The technique incorporates microphysical observations from imaging probes and bulk mass probes as well as measurements from a ground-based radar to compare how quantities derived from ice particle size distributions (PSDs), such as ice water content and reflectivity, relate to the other measurements for a range of m-D coefficients. The equally plausible solutions derived using this framework are presented as a surface in an (a,b) phase space, and can be applied to a microphysics parameterization or retrieval scheme that supports random selection among a range of potential empirical parameters.

Since weather and climate models are also limited by the lack of measurements made in some regions of the world, the second focus of this thesis was the result of a field campaign conducted in the Southern Ocean to collect more observations of boundary layer clouds. For one of the research flights, microphysical observations were collected at various depths within an atmospheric river and represent a unique dataset for Southern Hemisphere atmospheric rivers. The precipitation structures, microphysical processes, and vertical motions observed within the atmospheric river could offer potential areas of model improvement by comparing simulations of these systems to observations made during flight.

To my parents, wife, and dog Annabelle

Acknowledgments

First, I would like to express my sincere gratitude to my advisors Prof. Robert Rauber and Prof. Greg McFarquhar for their valuable time and mentorship over the years. Their expertise in radar meteorology and cloud microphysics has allowed me to pursue research that combines both areas of discipline in a meaningful way. I am also grateful to the other members of my doctoral committee, Prof. Stephen Nesbitt and Prof. Sonia Lasher-Trapp, for their valuable feedback.

I'd like to thank the Department of Atmospheric Sciences at the University of Illinois for its dedication to supporting its students. I'd also like to thank my research group, including past members of the PLOWS group and current members for their helpful feedback and insightful discussions. I'd also like to acknowledge the dedication of the SESE IT staff for their support of the school computing resources of which the data processing and analysis pertaining to this thesis would not have been possible.

Finally, this project would not have been possible without the help of funding agencies. I acknowledge funding from the U.S. Department of Energy under Grants DE-SC0014065 and DE-SC0016476 (through UCAR subcontract SUBAWD000397), from the NASA Precipitation Measurement Missions grant NNX16AD80G, and from the National Science Foundation grants AGS-1247404 and AGS-1762096.

Contents

Chapter 1

Background and motivation

This chapter provides necessary background on cloud microphysics from observational and modeling perspectives. First, the current state of microphysical measurements is discussed with emphasis on optical array probe (OAP) operating principals, limitations, processing techniques, and uncertainties in microphysical properties, including mass-dimension *m-D* relationships. Second, the current state of microphysical parameterizations within numerical models is discussed with emphasis on uncertainties in the representation of ice particle mass. This chapter concludes with scientific questions addressed by this thesis.

1.1 Uncertainties in microphysical observations

In an effort to better understand the microphysical properties of ice and the processes governing these properties, numerous field projects involving research aircraft have been conducted since the early 1960s (Baumgardner et al., 2017). While substantial progress has been made in the instrumentation used and processing techniques employed, uncertainties arising from current measurement limitations of OAPs are described below to provide motivation for the scientific questions addressed in section 1.3.

Two-dimensional (2D) OAPs contain a linear array of photodiodes that detect the light intensity cast by a laser beam. If this light source is to any degree obstructed by a particle passing through the instrument's sample volume, then a subset of photodiodes are shadowed and converted to a one-dimensional length based on the number of photodiodes shadowed multiplied by the resolution of an individual photodiode (Knollenberg and Knollenberg, 1970). OAPs additionally contain fast-response electronics that permit the status of the photodiode array to be monitored for each time step, thus providing particle information along two dimensions. From here, information regarding the particle size, shape, and other morphological characteristics can be obtained. When this process is repeated for numerous particles during flight, distributions of particle sizes and bulk properties such as number concentration or ice water content can be derived.

Current limitations of OAPs lead to various sources of measurement uncertainty depending on the size, habit, and

phase of the particle. One source of uncertainty concerns how a particle's depth of field is defined as a function of its size when the nominal depth of field is smaller than the distance between the arms of an OAP (McFarquhar et al., 2017). When particles are outside the focal plane of the OAP, particles are susceptible to being improperly sized due to uncertainties in the particle's depth of field (Korolev et al., 1998). Another source of measurement uncertainty arises from the shattering of ice crystals on the tips of the OAP's arms and subsequently entering the instrument sample volume (Korolev et al., 2013a). While inclusion of anti-shattering tips in conjunction with shattering algorithms have been shown to reduce the presence of shattered artifacts (e.g., Field et al., 2006; Jackson et al., 2014), the processing methods used to mitigate these artifacts may differ among the various software packages.

Numerous studies have leveraged the microphysical data to relate a particle's mass *m* to its maximum dimension *D* as a power law of the form $m = aD^b$. Through these mass-dimension (*m-D*) relations a single pair of *a* and *b* coefficients that best matches the mass, integrated over all particles, to an independent bulk measurement such as radar reflectivity, or measured bulk mass, is determined. These relationships are derived for different environments and using different techniques to derive the (*a,b*) coefficients, and is further discussed in chapter 2. Studies that only consider a single pair of *a* and *b* coefficients for a given environment are unable to account for the variability in microphysical properties occurring for different environments and the inherent uncertainties caused by the limitations of OAPs. Further, relating a particle's mass, a three-dimensional property, to its size based on 2D images introduces another uncertainty as the particle's volumetric characteristics are not available. Jackson et al. (2012) observed that there is up to a 50% uncertainty in estimating particle mass from 2D particle images, further necessitating an approach that goes beyond characterizing particle mass using a single *m-D* relationship for a given environment.

1.2 Representation of microphysical properties in models and remote sensing retrievals

1.2.1 Microphysical properties in models

The representation of cloud processes has been a long-standing and prominent source of uncertainty in regional-scale and global climate models (Intergovernmental Panel on Climate Change, 2014, and references therein) for decades. These uncertainties are impacted by a lack of understanding of some microphysical processes, particularly those involving ice-phase particles, and by the lack of observations in some regions of the world. Discussion below (1) explains how a recent field project aims to improve model representation of Southern Ocean clouds, and (2) provides an overview for how empirically-derived *m-D* relationships are used in models today.

Improving model representation of Southern Ocean clouds

Clouds over the Southern Ocean (SO) are poorly represented in global climate model simulations (Trenberth et al., 2010), and recent analyses of model simulations indicate that a lack of simulated clouds in the cold sectors of cyclones is a major contributor to microphysical uncertainty in the SO (Marchand et al., 2014). A key objective of SOCRATES was to examine the dynamical, physical, and radiative interactions of mixed-phase clouds in the SO.

On 28–29 January 2018 a unique opportunity was presented to sample an atmospheric river (AR) extending from northwest Australia to south of New Zealand. Radar and microphysical measurements were made for 2 passes through the AR including observations at various depths of the precipitation band as the aircraft descended. The lack of *in situ* measurements of ARs affecting Australia and the SO (Knippertz et al., 2013) combined with the scarcity of observations from imaging probes in these systems altogether make these measurements valuable from the perspective of microphysical parameterization improvements. Results from this event are discussed in chapter 4.

Model representation of *m-D* relations

The majority of microphysical parameterizations developed and used today are bulk schemes that use the prognostic mass mixing ratio (and number concentration for double-moment schemes) to determine the PSD. These schemes, particularly ones that resolve ice processes, rely on assumptions such as *m-D* relations to determine the terminal fall speeds, microphysical process rates, and parameters of the PSD (Gettelman et al., 2010; Morrison et al., 2011). For example, the a and b coefficients affect the shape λ and intercept N_0 parameters of the gamma distribution in the Morrison double-moment scheme as given by

$$\lambda = \left[\frac{aN\Gamma(b+1)}{q}\right]^{\frac{1}{b}} \text{and} \tag{1.1}$$

$$N_0 = N\lambda, \tag{1.2}$$

where q is the mass mixing ratio and N is the number concentration in kg^{-1}. Few studies have investigated the sensitivity of a and b coefficients representing *m-D* relationships on output from model simulations. For the studies that have investigated this sensitivity, differences of 20 to 50% in the modeled precipitation rate (McCumber et al., 1991) while other studies attributed differences in model simulations to the influence of a particle's mass on terminal fall velocities (e.g., Mitchell, 1996; Erfani and Mitchell, 2016).

Most bulk microphysical schemes to date do not account for complexity regarding particle mass, and some apply a simple spherical ice assumption to the a and b coefficients (Morrison et al., 2011). Instead, a single, fixed set of coefficients from mass-Dimension (m-D) and fall speed-Dimension (V-D) relationships are typically assigned to each ice phase class (e.g., cloud ice, snow, and graupel/hail). These empirically-derived relations are typically taken from

observational studies that targeted specific environmental conditions with some consisting of a small particle dataset for which best fit relations are derived (e.g., Locatelli and Hobbs, 1974), and subsequently applied to a parameterization irrespective of the type of weather phenomenon being simulated. Thus, these microphysical parameterizations are largely unable to adequately represent the variability of observed cloud conditions, especially within a vertical column where ice crystal habits can be influenced by the temperature.

1.2.2 Remote sensing retrieval representation of *m-D* relations

The retrieval of cloud and precipitation properties from spaceborne platforms is of great interest to the atmospheric sciences community given their ability to provide vertical profiles of precipitation structure for large regions of the globe. As successor to the Tropical Rainfall Measuring Mission (TRMM) mission, the Global Precipitation Measurement (GPM) mission aims to profile colder regions of the globe, where ice processes are more important to the formation of precipitation systems, by providing measurements on a global scale (Skofronick-Jackson et al., 2017).

One of the instruments installed for GPM was a Dual-Frequency Precipitation Radar (DPR) to provide estimates of the characteristic size of particles as well as their distribution. While DPR is able to provide three-dimensional measurements of precipitation structure, retrieval of microphysical properties require assumptions such as the relationship between particle mass and its size based on emperical relations derived in field experiments as mentioned earlier. Currently, these retrievals do not employ *m-D* relations that account for the variability of cloud conditions or the uncertainties inherent in the microphysical measurements that derive these relations.

1.3 Research questions

1.3.1 Research questions and tasks

The scientific questions investigated during this research are as follows:

1. How do temperature and other environmental variables influence the mass-dimension relationships of ice hydrometeors when accounting for microphysical variability and measurement uncertainties?

2. What are the microphysical properties occurring within a Southern Hemisphere AR that govern the distribution of particle sizes, shapes, and habits at various depths within the cloud?

To answer these scientific questions, the following innovations were necessary:

1. Development of a robust algorithm that computes the χ^2 difference between reflectivity and ice water content from the PSD and those directly measured by a bulk mass probe and radar. The χ^2 were computed for a range of a and b coefficients with fine incremental spacing.

2. Utilizing optical array probe software developed at the University of Illinois and the University of Oklahoma to obtain size and morphological properties of individual particles.

1.3.2 Organization of the thesis

Chapter 2 presents a novel approach used to determine the range of *a* and *b* coefficients within an *m-D* relationship for environments with similar environmental conditions that are considered equally plausible solutions when considering the natural variability and measurement uncertainties. This approach is applied to 3 mesoscale convective system events from MC3E. This work was published in *Atmospheric Chemistry and Physics*, entitled "A novel approach to characterize the variability in mass-Dimension relationships: results from MC3E" (Finlon et al., 2019).

Chapter 3 expands upon the technique detailed in chapter 2 and is applied to 19 research flights spanning 3 GPM ground validation field experiments to further test whether temperature and ice water content influence the *m-D* relations. This work is in preparation for *Journal of Applied Meteorology and Climatology* and will be entitled "Environmental dependence of mass-dimension relationships from three GPM ground validation campaigns".

Chapter 4 explores the microphysical properties and resulting precipitation structure of a Southern Hemisphere AR that was sampled during the SOCRATES campaign. This work is in preparation for *Journal of Geophysical Research* and will be entitled "Structure of an atmospheric river over Australia and the Southern Ocean. Part II: Microphysical evolution of the seeder-feeder process".

Chapter 5 summarizes the findings and outlines the implications of representing an environment with multiple *m-D* relations and the unique microphysical observations obtained within a Southern Hemisphere AR, and proposes avenues for future scientific research that are alluded to throughout this dissertation.

Chapter 2

A novel approach to characterize the variability in mass-Dimension relationships: results from MC3E

This chapter uses a novel approach to determine which parameters from a mass-dimension relationship are considered as equally plausible solutions for environments of similar temperature during the Mid-latitude Continental Convective Clouds Experiment. The material contained within this chapter was published in Finlon et al. (2019).

2.1 Introduction

Mass-dimension (*m-D*) relations are required to link bulk microphysical properties, such as total water content (*TWC*) and forward model radar reflectivity factor (*Z*), to ice crystal particle size distributions (PSDs). These relations are extensively assumed in both numerical models and remote sensing retrievals and relate a particle's mass (m) to its size, typically defined by its maximum dimension projected onto a 2-D plane (D), by means of a power law in the form $m = aD^b$. Past studies have suggested the exponent b is related to the exponent in surface area-dimension relationships (Fontaine et al., 2014) or to a particle's fractal dimension (Schmitt and Heymsfield, 2010). The prefactor a has some dependence on b and on the particle density.

Prior *m-D* relationships have been determined using cloud probe data obtained in a variety of environmental conditions. Figure 2.1a shows how *m-D* coefficients derived from previous studies vary depending on the types of clouds sampled. A full list of these *m-D* coefficients and their corresponding references is available as a supplement. Coefficients derived using data over mountainous terrain (e.g., Nakaya and Terada, 1935; Locatelli and Hobbs, 1974), cirrus clouds (e.g., Heymsfield, 1972; Hogan et al., 2000), convective clouds (e.g., Liu and Curry, 2000; Cazenave et al., 2016; Leroy et al., 2016), regions of large scale ascent (e.g., Szyrmer and Zawadzki, 2010), and computer-generated shapes (e.g., Matrosov, 2007; Olson et al., 2016) are shown. A total of 119 relations are shown in Fig. 2.1. The range of a in Fig. 2.1a spans five orders of magnitude, with variations in a spanning 3 orders of magnitude or more even for measurements obtained in the same cloud type. The exponent b ranges between one and three within the same environments. The relations in Fig. 2.1 were derived using data collected by different types and versions of cloud probes, using different algorithms to process the data. McFarquhar et al. (2017) have shown that it can be

difficult to disentangle the dependence of derived microphysical parameters on environmental conditions from the dependence on the probes used to collect and the methods to process the data.

Figure 2.1b shows that *m-D* coefficients also vary depending on the technique used to derive the *m-D* relations. In some studies the maximum dimension of frozen hydrometeors was recorded before the crystal was melted and the single particle mass subsequently measured (Magono and Nakamura, 1965; Zikmunda and Vali, 1972; Mitchell et al., 1990), whereas other studies used measurements of either bulk mass measured by an evaporation probe (Heymsfield et al., 2002; Cotton et al., 2013; Xu and Mace, 2017) or bulk Z observed by a collocated radar measurement (McFarquhar et al., 2007b; Maahn et al., 2015) in combination with in situ measured PSDs. Further, Wu and McFarquhar (2016) showed inconsistencies in how *D* is defined (Mitchell and Arnott, 1994; Brown and Francis, 1995; McFarquhar and Heymsfield, 1996; Heymsfield et al., 2013; Lawson et al., 2015; Korolev and Field, 2015) can also impact *m-D* relations. For example, they noted ice water content (*IWC*) values derived using various definitions of *D* ranged between 60 and 160% of the *IWC* derived using a smallest enclosing circle to define *D*.

Remote sensing retrieval schemes and model microphysical parameterization schemes are sensitive to the choice of *m-D* relationship. For example, Delanoë and Hogan (2010) showed that differences in the mean extinction, *IWC*, and effective radius retrieved from spaceborne remote sensors were 28, 9, and 30%, respectively, depending on whether *m-D* relations of spherical aggregates (Brown and Francis, 1995, hereafter BF95) or bullet rosettes (Mitchell, 1996) were used. McCumber et al. (1991) showed time series of modeled precipitation rate with differences of 20 to 50% depending on assumptions about particle density, which are affected by the *m-D* relation. Later studies (e.g., Mitchell, 1996; Erfani and Mitchell, 2016) attributed differences in model output to the influence of particle mass on terminal fall velocities.

Although many studies have established *m-D* relations for specific cases, a universal *m-D* relationship has not been found nor can a single relation be expected to represent the wide range of crystal habits and sizes within clouds occurring at different temperatures, locations, or formed by different mechanisms. Moreover, a single relationship cannot account for the natural variability of cloud properties such as particle size, shape, and density that occurs even in similar environmental conditions. Thus, some alternate approach is more appropriate for modeling and remote sensing studies that considers multiple *m-D* relations over many retrievals or model simulations to evaluate the variability in the ensemble results.

While previous studies (e.g., McFarquhar et al., 2007a; Heymsfield et al., 2010; Mascio et al., 2017) have considered how *m-D* relations vary with environmental conditions, such as temperature, the derived relations were fixed regardless of potential fluctuations for that environment. Further uncertainties were associated with measurement errors induced by shattering of large ice crystals on probe tips and subsequent detection within the probe's sample volume (Field et al., 2003), the processing techniques used (McFarquhar et al., 2017), and from the statistical count-

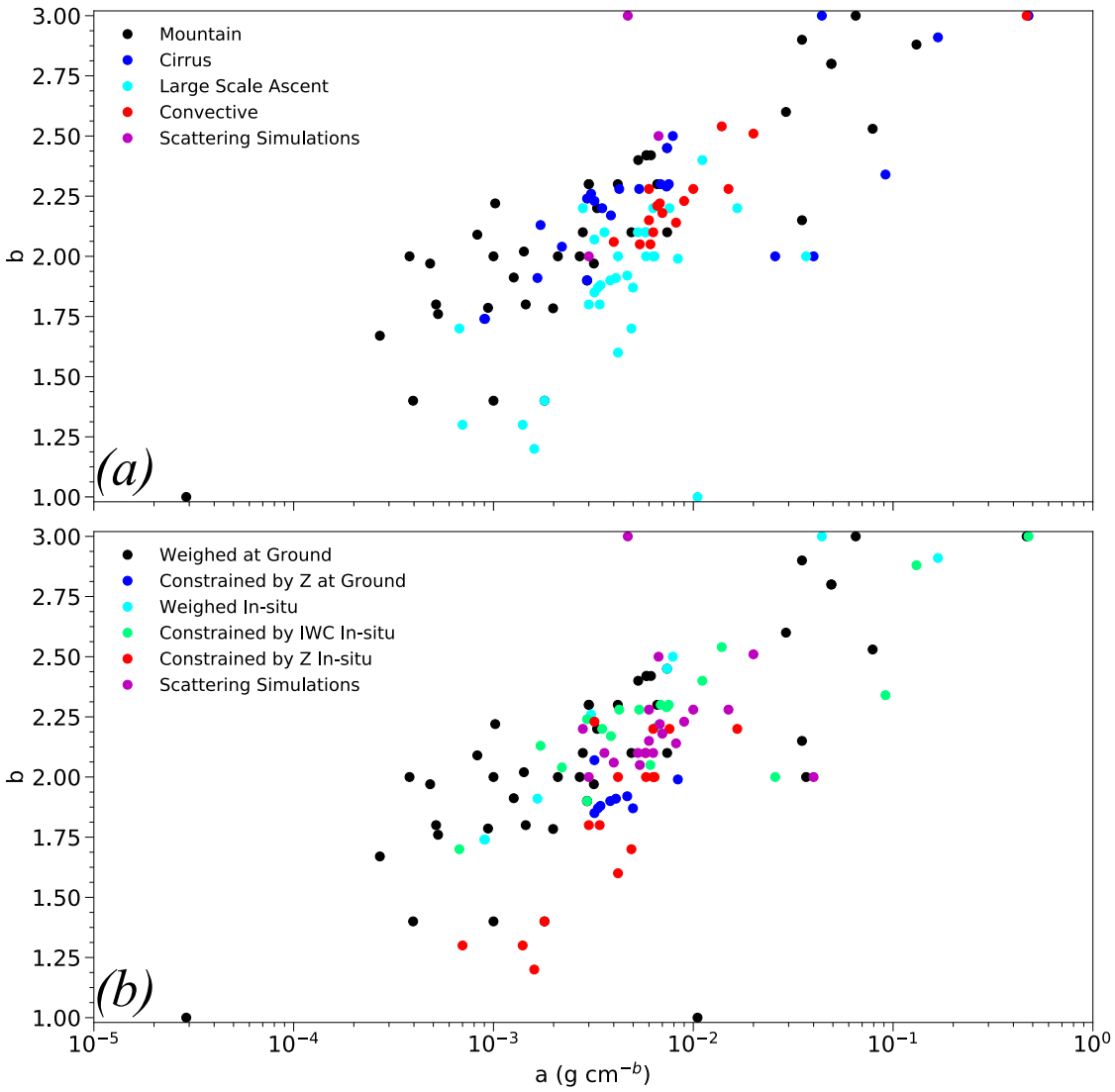

Figure 2.1: Distribution of a and b coefficients used to characterize $m = aD^b$ relationship from past studies. Points colored by the (a) environment in which measurements were made and (b) technique used to derive the relations.

ing of particles (e.g., Hallett, 2003; McFarquhar et al., 2007b). The approach by Fontaine et al. (2014) evaluated the variability in the prefactor a for an assumed exponent b for two field projects, but ultimately still derived a single *m-D* relationship for each dataset based on the mean conditions.

Extending the approach of McFarquhar et al. (2015), which derived a volume of equally realizable solutions within the phase space of the three gamma fit parameters (concentration N_0, shape μ, and slope λ) characterizing PSDs, a novel approach is used here to determine equally valid *m-D* relations for a given environment. Data from a variety of environments sampled during the Mid-latitude Continental Convective Clouds Experiment (MC3E) are used to establish a surface of equally plausible a and b coefficients in (a,b) phase space using a technique that minimizes the chi-square difference between the *TWC* and *Z* derived from the PSDs measured by optical array probes (OAPs) and

that directly measured by a *TWC* probe and radar.

The remainder of this chapter is organized as follows. Section 2.2 outlines the datasets used and the methodology to process the radar and microphysics data, while Sect. 2.3 describes the technique employed to determine the surfaces of *m-D* coefficients. A brief description of the MC3E cases used in this study is provided in Sect. 2.4, and the surfaces of coefficients are derived and discussed in Sect. 2.5. A summary of the technique and its implications for numerical modeling and remote sensing retrieval schemes are given in Sect. 2.6.

2.2 Data and methodology

The data in this study were collected within mesoscale convective systems (MCSs) during the 2011 Mid-latitude Continental Convective Clouds Experiment (MC3E; Jensen et al., 2016). The study presented here uses data from cloud microphysical instruments aboard the University of North Dakota (UND) Cessna Citation II aircraft and from the Vance Air Force Base, OK (KVNX) Weather Surveillance Radar-1988 Doppler (WSR-88D) radar.

2.2.1 Identification of coincident aircraft/radar data

The use of airborne microphysical measurements and radar data collected from the ground allowed sampling of the same region of the cloud from microphysical and remote sensing perspectives. Use of the Airborne Weather Observation Toolkit (https://github.com/swnesbitt/AWOT) radar matching algorithm and the Python ARM Radar Toolkit (Py-ART; Helmus and Collis, 2016) permitted calculation of radar *Z* in the vicinity of the aircraft for each second of in situ cloud distributions measured during flight. The algorithm organizes all radar gates in a 3-Dimensional space (Maneewongvatana and Mount, 1999) for efficient acquisition of radar parameters at nearby radar range gates. The Barnes (1964) interpolation technique is then applied to data at the eight nearest gates within 500 m of the aircraft's location, ignoring vertically adjacent gates beyond a range of 65 km as the beamwidth exceeds the 500 m threshold, to obtain an averaged *Z* at the aircraft location.

To compare microphysical properties with radar-measured Z for constant altitude flight legs at similar environmental temperature, only those times when the radar and microphysical datasets are coincident and the temperature varies by less than 1 $^{\circ}\mathrm{C}$ were considered. To reduce uncertainty due to counting statistics in the measured PSDs, microphysical data were averaged over a 10 s period. Each 10 s period determined required radar echo and microphysical data for all 1 s samples to ensure that the aircraft and matched radar *Z* were completely in cloud during the 10 s period. The *TWC* measurements and matched radar *Z* were then averaged over the same 10 s period, with each 10 s interval assigned as a coincident point. Table 2.1 lists the start and end times, mean altitude, and temperature for each of the 16 constant-temperature flight legs flown when the UND Citation was in cloud. Observations where the mean

TWC for a 10 s interval < 0.05 g m^{-3} were ignored as the values were considered either below the noise threshold of the Nevzorov probe or optically thin cloud. To further constrain the study to periods when clouds were dominated by ice phase hydrometeors such that *TWC* $\approx$ *IWC* and to reduce the impact of liquid phase hydrometeors on the derived *TWC* and *Z*, observations were excluded from the analysis if the concentration from the cloud droplet probe exceeded 10 cm^{-3} at any point during the 10 s interval which usually corresponds to the presence of water (Heymsfield et al., 2011). Of the coincident observations considered, 13% were excluded from the analysis based on these criteria. A total of 489 coincident observations were retained for this analysis.

Table 2.1: List of constant temperature flight legs used in the analysis for which coincident data between the ground-based radar and UND Citation exist. Start and end times, mean altitude, and temperature displayed.

Mean Temp. [°C]	Mean Alt. [km]	Start Time [UTC]	End Time [UTC]
25 April 2011			
-22.0	6.8	11:42:50	11:49:00
-26.5	7.4	11:05:20	11:14:45
-26.5	7.4	11:21:20	11:34:05
-35.5	8.3	10:03:05	10:08:45
-35.5	8.3	10:11:10	10:20:15
-35.5	8.3	10:28:30	10:35:45
-35.5	8.3	10:51:15	10:59:10
20 May 2011			
-5.5	5.0	13:41:25	13:52:00
-10.5	5.9	13:54:05	14:00:05
-16.0	6.9	14:35:30	14:40:35
-23.0	7.9	14:16:30	14:32:15
23 May 2011			
-25.0	7.9	21:49:55	21:55:15
-25.0	7.9	22:06:45	22:11:00
-34.5	9.1	22:32:50	22:37:15
-34.5	9.1	22:41:35	22:48:20
-34.5	9.1	22:58:40	23:03:40

2.2.2 Radar measurements

Data from the KVNX S-band (10 cm wavelength) radar were used in this study. Although the NASA dual-polarization (N-Pol) S-band Doppler radar was deployed during MC3E, mechanical issues prevented reliable collection of data for two of the three events examined here. Radars at other wavelengths collected data during MC3E. However, attenuation through liquid portions of the cloud (e.g., Bringi et al., 1990; Park et al., 2005; Matrosov, 2008) and non-Rayleigh scattering by larger particles (e.g., Lemke and Quante, 1999; Matrosov, 2007) could not be accounted for, and prompted exclusive use of the S-band radar.

Radar reflectivity factor values for gates near the UND Citation (Sect. 2.2.1) were used to obtain the average value of *Z* using the radar matching algorithm only if the following criteria were met: correlation coefficient $\rho_{HV} \geq 0.75$, sigma differential phase *SDP* $\leq 12\ \mathrm{deg}^2\ \mathrm{km}^{-2}$, differential reflectivity -2 $\leq Z_{DR} \leq 3$ dB, and reflectivity texture (defined as the standard deviation in *Z* of the nearest 5 gates) < 7 dBZ. These ranges represent acceptable values for echoes based on previous studies (Bringi and Chandrasekar, 2001). Radar gates not meeting these criteria were masked, reducing the likelihood of including gates with excessive signal noise due to clutter or weak signal, contamination by the aircraft, or other factors. For instances where the matched *Z* changed by more than 2 dBZ for subsequent 1 s points (fewer than one percent of the observations), all radar gates factored into the radar matching algorithm were inspected by eye to ensure that no outlier values were responsible for the jump in the matched *Z*. Of the observations that were manually inspected, all appeared spatially consistent with no outliers present, and as such remained in the averaging routine of the matching algorithm discussed in Sect. 2.2.1.

2.2.3 Microphysical measurements

During MC3E the Citation aircraft sampled clouds in situ, with most data collected in ice phase clouds between the melting layer and cloud top (Jensen et al., 2016). A suite of microphysical instruments was installed on the aircraft, including OAPs, which were used to image particles and derive PSDs, and a TWC probe. Specifics on the instrumentation and steps used to process the data are described below.

OAP data

A cloud imaging probe (CIP), a 2D cloud (2D-C) probe, and a High Volume Precipitation Spectrometer Version 3 (HVPS-3) sized particles by shadowing photodiode arrays attached to fast response electronics. Data from the 2D-C and HVPS-3 were combined to create a composite PSD, permitting particles between 150 μm and 19.2 mm to be considered in the analysis. The 2D-C was used instead of the CIP in the analysis even though the CIP has a larger sample volume because the inclusion of anti-shattering tips on the 2D-C reduced the impact of shattered artifacts (e.g., Korolev et al., 2011). Previous studies (Korolev et al., 2011, 2013b; Jackson et al., 2014) have shown that use of algorithms to identify shattered artifacts are sometimes needed even when the OAP is equipped with anti-shattering tips. Artifacts are identified by examining the frequency distribution of the times between which particles enter the sample volume (inter-arrival time; Field et al., 2006). When artifacts are present, this distribution follows a bimodal distribution with naturally-occurring particles having a mode with longer inter-arrival times and shattered artifacts having a mode with shorter inter-arrival times (e.g., Field et al., 2003). During MC3E there was only one mode in the inter-arrival time distribution corresponding to the naturally-occurring particles (Wu and McFarquhar, 2016) at all times, suggesting there were few shattered artifacts. Therefore, no shattering removal algorithm was used for the 2D-C

and HVPS. Following Wu and McFarquhar (2016), the number distribution function *N(D)* was determined using the 2D-C for particles with $D < 1$ mm and the HVPS-3 for $D > 1$ mm. The 1 mm cutoff was chosen since *N(D)* for the two OAPs agreed on average within 5 percent for $0.8 \leq D \leq 1.2$ mm, and was used for all PSDs irrespective of periods when the difference between *N(D)* for the OAPs exceeded 5% in the overlap region. Given uncertainties in the probe's sample area and limitations of its depth of field for smaller particle sizes (Baumgardner and Korolev, 1997), particles with $D < 150$ μm were not included in the analysis.

The OAP data were processed using the University of Illinois/Oklahoma OAP Processing Software (UIOOPS; McFarquhar et al., 2018a). Numerous morphological properties were calculated (e.g., particle maximum dimension, projected area, perimeter, area ratio, and habit) for individual particles, and PSDs were determined for each second of flight. Following Heymsfield and Baumgardner (1985) and Field (1999), only particles imaged with their center within the OAP's field of view were considered as otherwise there is too much uncertainty in particle size. Particles were identified as having their center within the field of view if their maximum dimension along the time direction exceeded the largest length where the particle potentially touched the edge of the photodiode array.

TWC data

The *TWC* was determined from the Nevzorov probe using the power required to melt or evaporate ice particles impinging on the inside of a cone (e.g., Nevzorov, 1980; Korolev et al., 1998). The probe used had a deeper cone than previous designs with a 60° vertex angle (as opposed to a 120° angle) that prevented many particles from bouncing out of the cone. Because previous studies suggested that particles with $D > 4$ mm can bounce out of even the deeper cone (Wang et al., 2015), *TWC* may be underestimated when such particles are present. However, Korolev et al. (2013a) showed that the ratio of the Nevzorov *IWC* to that derived from the measured PSDs using the BF95 relation did not significantly vary with particle maximum dimension. Of the coincident points belonging to constant altitude flight legs in this study, 79.2% of the observations had cumulative mass estimates using the BF95 relation from particles with $D \leq 4$ mm contributing at least 80% to the total mass. Therefore, measurements of *TWC* were included irrespective of whether $D_{\text{max}} > 4$ mm.

2.3 Development of equally plausible (*a,b*) surfaces

In this section, a method for determining a surface of equally realizable solutions for *m-D* coefficients in the phase space of (*a,b*) coefficients is described. The surface of these coefficients is determined through a procedure that minimizes the χ^2 differences between the *TWC* and *Z* derived from *N(D)* and that directly measured by the Nevzorov and ground-based radar, respectively. The minimization procedure is carried out for each constant-temperature flight

leg (defined by temperature varying by less than 1 °C) for the MC3E cases studied. This approach follows that of McFarquhar et al. (2015) who developed volumes of equally realizable N_0, μ, and λ characterizing observed *N(D)* as gamma distributions for observations obtained during the Indirect and Semi-Direct Aerosol Campaign (ISDAC) and the NASA African Monsoon Multidisciplinary Analyses project (NAMMA).

For an individual 10 s sample, the *TWC* and *Z* derived from the PSD for a specific *a* and *b* is given by TWC_{SD} and Z_{SD}, respectively, as

$$TWC_{SD} = \sum_{j=1}^{N} (aD^b) N(D_j) dD_j \text{ and} \tag{2.1}$$

$$Z_{SD} = \left(\frac{6}{\pi \rho_{ice}}\right) \frac{|K_{ice}|^2}{|K_w|^2} \sum_{j=1}^{N} (aD^b)^2 N(D_j) dD_j \tag{2.2}$$

following the method of Hogan et al. (2006) and accounting for the different dielectric constants for water ($|K_w|^2 = 0.93$) and ice ($|K_{ice}|^2 = 0.17$). Uncertainties in TWC_{SD} and Z_{SD} are discussed later in this section. The metric defining the difference between the *TWC* and *Z* derived from *N(D)* for a specific *a* and *b* and that directly measured by the Nevzorov and ground-based radar, respectively, is given by TWC_{diff} and Z_{diff} as follows:

$$TWC_{diff} = \left[\frac{TWC - TWC_{SD}(a,b)}{\sqrt{TWC \times TWC_{SD}(a,b)}}\right]^2 \text{ and} \tag{2.3}$$

$$Z_{diff} = \left[\frac{\sqrt{Z} - \sqrt{Z_{SD}(a,b)}}{\sqrt{\sqrt{Z} \times \sqrt{Z_{SD}(a,b)}}}\right]^2. \tag{2.4}$$

In this study, TWC_{diff} and Z_{diff} are computed for all points in the domain of values encompassing $5 \times 10^{-4} < a < 0.35$ g cm^{-b} and $0.20 < b < 5.00$ at increments of 5×10^{-4} g cm^{-b} and 0.01, respectively.

Given a priori assumptions of *Z* being proportional to the square of a particle's mass, the square root of reflectivity was used in Eq. (2.4) so that TWC_{diff} would be similar to Z_{diff} on average and each would have approximately equal weight in determining *a* and *b*. Although radar *Z* measurements involve a significantly greater sample volume than that of OAPs and a bulk content probe, TWC_{diff} and Z_{diff} were not weighted proportionally to the sample volume in order to ensure that both bulk moments had some impact on the derived *a* and *b*. Given that larger ice crystals are fractionally more important than small crystals in determining Z_{SD} than TWC_{SD} and given varying contributions of larger crystals to Z_{SD} and TWC_{SD}, TWC_{diff} has a greater impact on the χ^2 minimization procedure some of the time while Z_{diff} does at other times. The ratios between Z_{diff} and TWC_{diff} for each flight leg are given in Table 2.2, and range between 0.32 and 8.58 with a mean of 2.62 for the 16 flight legs. No attempt is made to force equal weight for Z_{diff} and TWC_{diff} for each coincident point because there are periods when cloud properties influence *TWC* differently

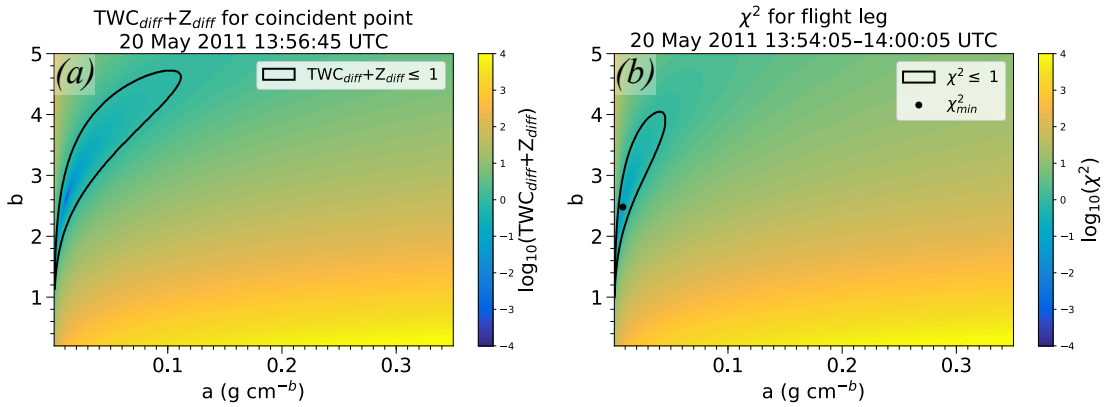

Figure 2.2: $TWC_{\text{diff}} + Z_{\text{diff}}$ in (a,b) phase space for (a) a 10 s coincident point beginning 13:56:15 UTC on 20 May 2011 and (b) integrated over the encompassing flight leg between 13:54:14 and 13:59:35 UTC and normalized by the number of observations N. The black dot in (b) denotes the a and b minimizing χ^2.

than Z.

Table 2.2: List of constant temperature flight legs and the ratio between Z_{diff} and TWC_{diff} valid at the (a,b) that minimize χ^2.

25 April 2011		20 May 2011		23 May 2011	
Times [UTC]	$\frac{Z_{\text{diff}}}{TWC_{\text{diff}}}$	Times [UTC]	$\frac{Z_{\text{diff}}}{TWC_{\text{diff}}}$	Times [UTC]	$\frac{Z_{\text{diff}}}{TWC_{\text{diff}}}$
11:42:50–11:49:00	2.02	13:41:25–13:52:00	4.92	21:49:55–21:55:15	1.52
11:05:20–11:14:45	0.81	13:54:05–14:00:05	6.31	22:06:45–22:11:00	1.82
11:21:20–11:34:05	1.62	14:35:30–14:40:35	3.2	22:32:50–22:37:15	0.99
10:03:05–10:08:45	0.8	14:16:30–14:32:15	3.99	22:41:35–22:48:20	1.82
10:11:10–10:20:15	1.5			22:58:40–23:03:40	0.32
10:28:30–10:35:45	8.58				
10:51:15–10:59:10	1.76				

At first, the sum of $TWC_{\text{diff}} + Z_{\text{diff}}$ is used to identify (a,b) values that characterize an individual 10 s data point. An example of $TWC_{\text{diff}} + Z_{\text{diff}}$ computed in (a,b) phase space for a 10 s averaged PSD measured beginning at 13:56:45 UTC on 20 May 2011 is shown in Fig. 2.2a. The color representing $TWC_{\text{diff}} + Z_{\text{diff}}$ is shaded on a logarithmic scale to more easily show the range of values. The smallest swath of values, arbitrarily chosen as being $TWC_{\text{diff}} + Z_{\text{diff}} \leq 1$ within the region outlined black, spans b values of 1.13 to 4.72. The curvature in the outlined region highlights the correlation of a and b showing that similar m can be obtained using very different b by adjusting a accordingly. Considering both TWC_{diff} and Z_{diff} allows the shape and placement of the smallest swath of values to adjust according to two different moments of the PSD since conditions impact TWC differently than Z. Using two constraints on the χ^2 minimization technique therefore provides additional insight into the microphysical properties as discussed in Sect. 2.5.

The chi-square statistic for a flight leg, defined as

$$\chi^2(a,b) = \frac{1}{N}\sum_{i=1}^{N}\left[TWC_{\text{diff}}(i) + Z_{\text{diff}}(i)\right], \tag{2.5}$$

involves a summation over all N 10 s coincident observations represented by the index *i* and normalized by N. When χ^2 is computed by summing over all N points in the flight leg, the region with the smallest χ^2 ($\chi^2 \leq 1$; outlined region in Fig. 2.2b) is smaller than the region in Fig. 2.2a which shows χ^2 for a single point, because different (*a,b*) minimize χ^2 for each of the individual PSDs in the 5 minute period depicted. Therefore, overall the χ^2 values are higher than the $TWC_{\text{diff}} + Z_{\text{diff}}$ computed for each (*a,b*). The point in Fig. 2.2b corresponds to the *a* and *b* point that minimizes χ^2, hereafter represented as χ^2_{min}, which represents the most likely *a* and *b* value.

To represent the uncertainty in the derived coefficients for each flight leg, all *a* and *b* fulfilling $\chi^2 \leq \chi^2_{\text{min}} + \Delta\chi^2$ are assumed to be equally plausible solutions. Analagous to McFarquhar et al. (2015), the confidence region is defined as $\Delta\chi^2 = \max(\chi^2_{\text{min}}, \Delta\chi^2_1, \Delta\chi^2_2)$. The χ^2_{min} characterizes the robustness of the minimization procedure affected by the natural parameter variability over a flight leg, $\Delta\chi^2_1$ represents uncertainties in the PSD due to statistical sampling uncertainties, and $\Delta\chi^2_2$ represents measurement uncertainties. Similar to their study, $\Delta\chi^2_1$ is determined here as

$$\Delta\chi^2_1 = \frac{1}{N}\sum_{i=1}^{N}\begin{array}{l}\frac{1}{2}\left\{\left[\frac{TWC_{\text{SD,min}}(i) - TWC_{\text{SD}}(i)}{\sqrt{TWC_{\text{SD,min}}(i)\times TWC_{\text{SD}}(i)}}\right]^2 + \left[\frac{\sqrt{Z_{\text{SD,min}}(i)} - \sqrt{Z_{\text{SD}}(i)}}{\sqrt{\sqrt{Z_{\text{SD,min}}(i)}\times\sqrt{Z_{\text{SD}}(i)}}}\right]^2\right\} + \\ \frac{1}{2}\left\{\left[\frac{TWC_{\text{SD,max}}(i) - TWC_{\text{SD}}(i)}{\sqrt{TWC_{\text{SD,max}}(i)\times TWC_{\text{SD}}(i)}}\right]^2 + \left[\frac{\sqrt{Z_{\text{SD,max}}(i)} - \sqrt{Z_{\text{SD}}(i)}}{\sqrt{\sqrt{Z_{\text{SD,max}}(i)}\times\sqrt{Z_{\text{SD}}(i)}}}\right]^2\right\}.\end{array} \tag{2.6}$$

The different terms in Eq. (2.6) represent the difference in the minimum and maximum *TWC* or *Z* derived from the minimum and maximum *N(D)* using the most likely (*a,b*) minimizing χ^2 ($TWC_{\text{SD,min}}$ and $TWC_{\text{SD,max}}$ or $Z_{\text{SD,min}}$ and $Z_{\text{SD,max}}$) and that derived from the measured *N(D)* (TWC_{SD} or Z_{SD}). Following McFarquhar et al. (2015), the minimum and maximum *N(D)* are determined by subtracting or adding the square root of the number of particles counted in each size bin to the number of particles counted in the bin when computing *N(D)*. This technique represents uncertainty in the actual particle counts for each size bin as given by Poisson statistics (Hallett, 2003; McFarquhar et al., 2007b).

Estimates of the measurement uncertainty from the OAPs, Nevzorov probe, and ground-based radar also influence

the uncertainty in the derived coefficients. The uncertainty due to measurement error $\Delta\chi_2^2$ is defined as

$$\Delta\chi_2^2 = \frac{1}{N}\sum_{i=1}^{N} \begin{aligned} &\frac{1}{2}\left\{ \left[\frac{TWC_{\text{SD,meas\_min}}(i) - TWC_{\text{SD}}(i)}{\sqrt{TWC_{\text{SD,meas\_min}}(i) \times TWC_{\text{SD}}(i)}}\right]^2 + \left[\frac{\sqrt{Z_{\text{SD,meas\_min}}(i)} - \sqrt{Z_{\text{SD}}(i)}}{\sqrt{\sqrt{Z_{\text{SD,meas\_min}}(i)} \times \sqrt{Z_{\text{SD}}(i)}}}\right]^2 + \left[\frac{TWC_{\text{meas\_min}}(i) - TWC(i)}{\sqrt{TWC_{\text{meas\_min}}(i) \times TWC(i)}}\right]^2 + \right. \\ &\left. \left[\frac{\sqrt{Z_{\text{meas\_min}}(i)} - \sqrt{Z(i)}}{\sqrt{\sqrt{Z_{\text{meas\_min}}(i)} \times \sqrt{Z(i)}}}\right]^2 \right\} + \frac{1}{2}\left\{ \left[\frac{TWC_{\text{SD,meas\_max}}(i) - TWC_{\text{SD}}(i)}{\sqrt{TWC_{\text{SD,meas\_max}}(i) \times TWC_{\text{SD}}(i)}}\right]^2 + \left[\frac{\sqrt{Z_{\text{SD,meas\_max}}(i)} - \sqrt{Z_{\text{SD}}(i)}}{\sqrt{\sqrt{Z_{\text{SD,meas\_max}}(i)} \times \sqrt{Z_{\text{SD}}(i)}}}\right]^2 + \right. \\ &\left. \left[\frac{TWC_{\text{meas\_max}}(i) - TWC(i)}{\sqrt{TWC_{\text{meas\_max}}(i) \times TWC(i)}}\right]^2 + \left[\frac{\sqrt{Z_{\text{meas\_max}}(i)} - \sqrt{Z(i)}}{\sqrt{\sqrt{Z_{\text{meas\_max}}(i)} \times \sqrt{Z(i)}}}\right]^2 \right\}. \end{aligned} \tag{2.7}$$

The terms $TWC_{\text{SD,meas\_min}}$, $TWC_{\text{SD,meas\_max}}$, $Z_{\text{SD,meas\_min}}$, and $Z_{\text{SD,meas\_max}}$ represent the minimum and maximum *TWC* or *Z* derived using a 50% uncertainty in the measured *N(D)*. This uncertainty follows Heymsfield et al. (2013) where up to a 50% difference in the number concentration for particles with $D > 0.1$ mm was determined. Uncertainties in the bulk measurements of *TWC* and *Z* must also be considered in the generation of the uncertainty surfaces with the minimum and maximum possible bulk values represented as $TWC_{\text{meas\_min}}$, $TWC_{\text{meas\_max}}$, $Z_{\text{meas\_min}}$, and $Z_{\text{meas\_max}}$. Following Korolev et al. (2013a), it was assumed that there was a 2% uncertainty when $D_{\text{max}} \leq 4$ mm and a 8% uncertainty for other periods to address the possibility of particles bouncing out of the cone of the Nevzorov probe. A radar reflectivity uncertainty of 1 dB (Krajewski and Ciach, 2003) is subtracted from or added to the measured *Z* to determine $Z_{\text{meas\_min}}$ and $Z_{\text{meas\_max}}$.

Figure 2.3 illustrates the frequency distribution of the ratio between χ^2_{min} and $\Delta\chi_1^2$ (blue shading) and between χ^2_{min} and $\Delta\chi_2^2$ (red shading) for all 16 flight legs. Of all 16 legs considered, 15 have a ratio between χ^2_{min} and $\Delta\chi_1^2$ greater than 1, meaning $\chi^2_{\text{min}} > \Delta\chi_1^2$, and 50% of the observations have ratios greater than 10. For 5 of the 16 legs, the ratio between χ^2_{min} and $\Delta\chi_2^2$ is greater than 1 indicating that the χ^2 obtained from the (*a,b*) minimization procedure is greater than the difference between moments derived from the minimum and maximum *N(D)* and from the minimum and maximum *TWC* and *Z* due to measurement errors for nearly a third of the periods in this study. This means that the natural parameter variability over a flight leg is sometimes more important for the derived uncertainty of *m-D* coefficients, whereas at other times measurement errors are more important. This is further discussed in Sect. 2.5.

At first, the *b* coefficients greater than 3 shown in Fig. 2.2 may seem counter intuitive as the mass of a particle cannot be greater than that of an ice sphere. Further, a particle's density would increase with increasing *D* for $b > 3$. But, due to the covariability of *a* and *b*, $b > 3$ does not necessarily imply the particle has a mass greater than a sphere. Nevertheless, equally plausible *b* values greater than 3 were closely inspected as past studies (e.g., Fontaine et al., 2014) have disregarded $b > 3$ as a possible exponent in an *m-D* relation. To investigate the impact of $b > 3$, a linear sequence of *b* values in the plausible surface was generated for each flight leg and the 5$^{\text{th}}$, 25$^{\text{th}}$, 50$^{\text{th}}$, 75$^{\text{th}}$, and 95$^{\text{th}}$ percentiles of *b* were determined. The corresponding *a* from each of these *b* was identified, and the cumulative

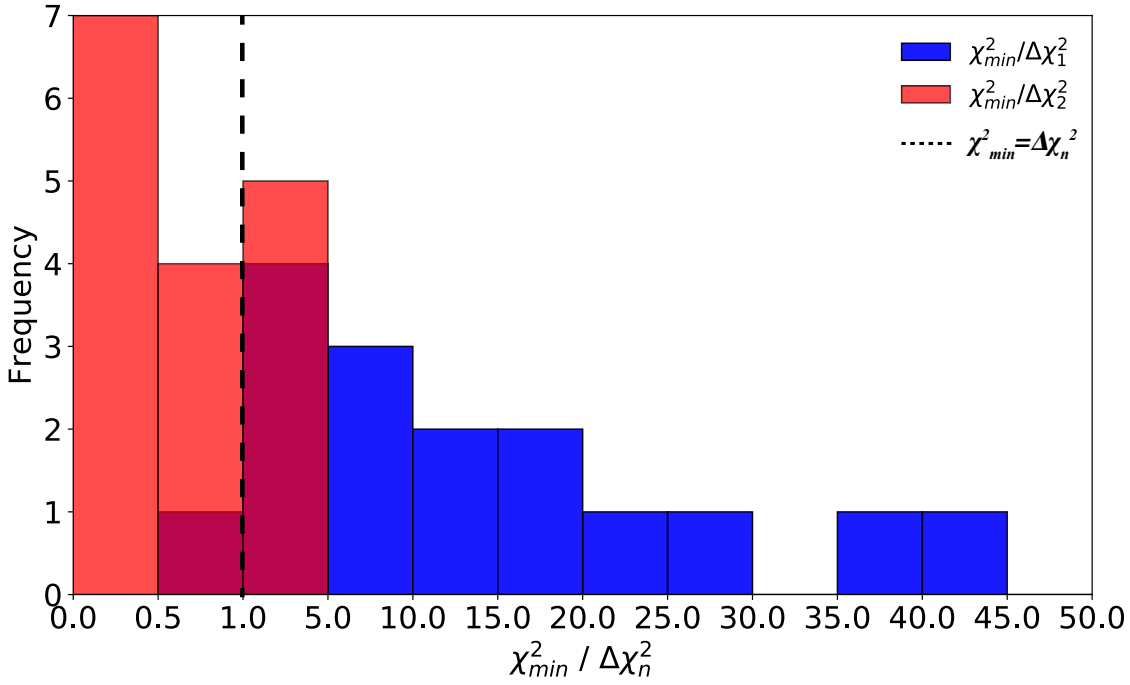

Figure 2.3: Frequency of $\chi^2_{min}/\Delta\chi^2_1$ (blue shading) and $\chi^2_{min}/\Delta\chi^2_2$ (red shading), where χ^2_{min}, $\Delta\chi^2_1$, and $\Delta\chi^2_2$ derived for each flight leg used in analysis.

reflectivity distribution functions, defined as

$$Z_c(D) = \left(\frac{6}{\pi \times \rho_{\text{ice}}}\right)^2 \frac{|K_{\text{ice}}|^2}{|K_w|^2} \int_0^D (aD'^b)^2 \, N(D') \, dD', \tag{2.8}$$

were computed using the mean *N(D)* for the period and the particle mass derived with these *a* and *b*. Figure 2.4 shows an example of the $Z_c(D)$ over the range of particle sizes observed from the -23 °C flight leg on 20 May 2011 using these *a* and *b* coefficients. The $Z_c(D)$ derived using BF95 coefficients, with the prefactor *a* ($= 0.002$ g cm$^{-1.9}$) modified following the correction factor of Hogan et al. (2012) applicable for the definition of *D* used here, is also shown for reference. It is worth noting that the modified BF95 coefficients may reasonably resolve the particle mass for *some* particle sizes for the PSD depicted in Fig. 2.4. While the lower values of *a* and *b* yield larger $Z_c(D)$ for smaller *D* than do the larger values of *a* and *b*, the derived total reflectivity $Z_t = \int_{D_{min}}^{D_{max}} Z(D)\, dD$ for the 5$^{\text{th}}$ and 95$^{\text{th}}$ percentiles of *b* are within 11.38 mm^6 m^{-3} of the mean matched radar *Z* of 18.36 mm^6 m^{-3} (12.64 dBZ), a difference of 62 percent of the mean. In contrast, the difference of the mean from the Z_t computed with modified BF95 coefficients is much higher, 88.6%, suggesting values of $b > 3$ are indeed giving plausible results for the range of particle sizes observed.

When the seven flight legs that have some values of $b > 3$ in the surface of equally plausible solutions are consid-

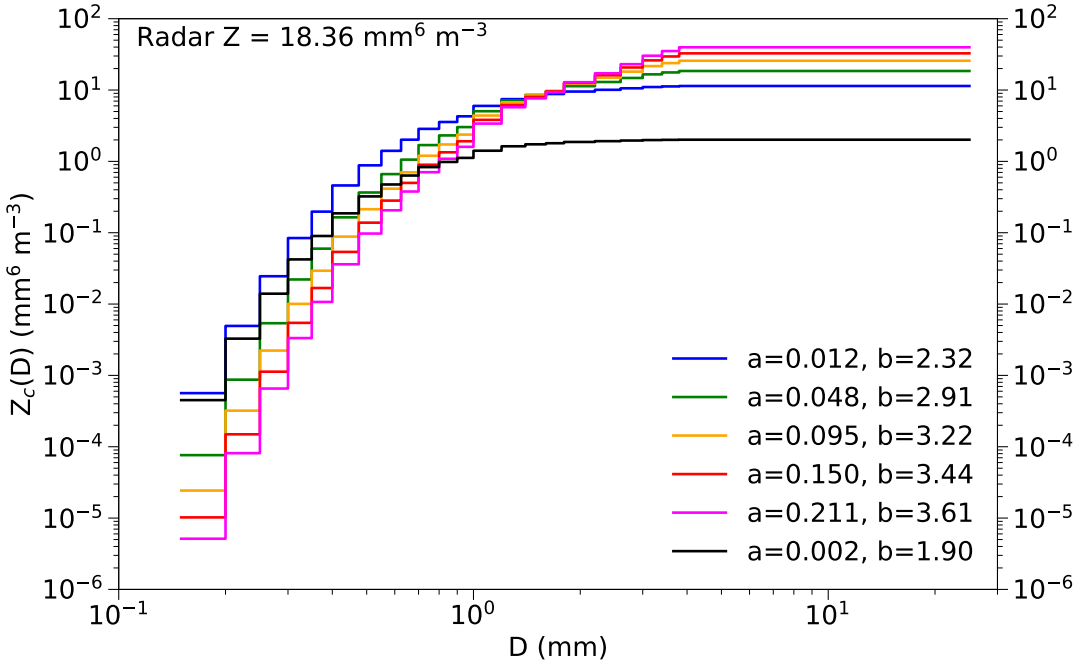

Figure 2.4: $Z_c(D)$ as a function of D derived using modified m-D coefficients from BF95 (black) and from the 5th (blue), 25th (green), 50th (orange), 75th (red), and 95th (magenta) percentiles from the set of equally plausible m-D coefficients in order of increasing b and a values for the 14:16:30–14:32:15 UTC flight leg on 20 May 2011. Mean radar reflectivity matched at the aircraft's position for the same period is listed in top left.

ered, Z values for the 5th and 95th percentiles of b are within 82.4% of the mean matched radar Z. While this value is greater than the 50.5% difference for the other flight legs and for the period illustrated in Fig. 2.4, Z values for the 5th and 95th percentiles are more consistent with the mean matched radar Z compared to that computed with the modified BF95 relationship.

Thus, the bulk variables such as Z derived using $b > 3$ are physically plausible for the distributions examined here given the covariability of a and b. However, this conclusion may only apply when the coefficients are applied over the range of particle sizes observed during MC3E and assuming PSDs with similar shapes. For example, for the 95th percentile of b ($b = 3.61$) and the corresponding value of a used to construct Fig. 2.4, ice particles with $D < 3.83$ cm have particle masses less than those of spherical particles with a density of solid ice for the same maximum dimension. On the other hand, if the covariability of a and b was not taken into account when choosing the corresponding a value, then a particle could have a mass greater than that of a spherical particle for much smaller D. While the technique highlights the possibility of a wide range of m-D coefficients for a given environment, equally plausible solutions containing $b > 3$ are still not considered in the remainder of this study to remain consistent with previous studies and to avoid any chance of unphysical behavior should the equally plausible coefficients be extrapolated to PSDs from

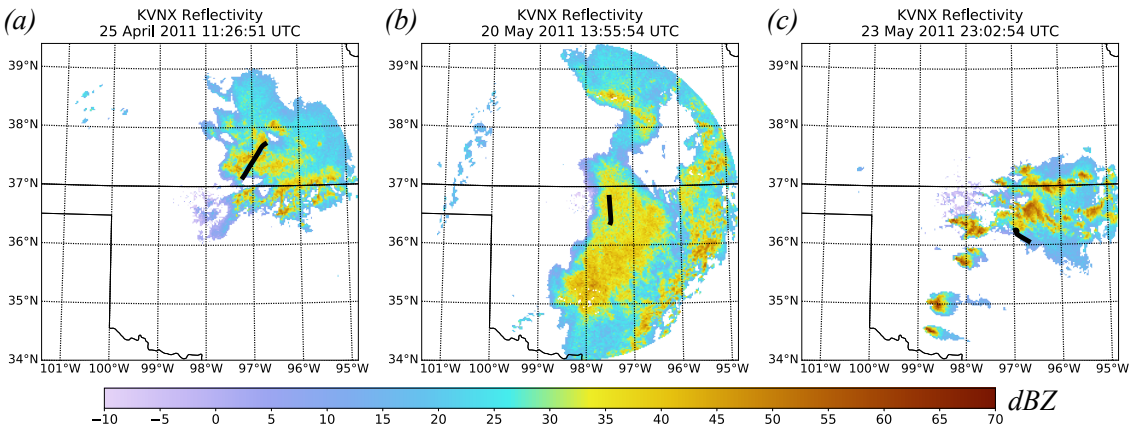

Figure 2.5: 0.5 degree PPI scan of corrected radar reflectivity from the KVNX radar for (a) 11:26:51 UTC 25 Apr 2011, (b) 14:04:34 UTC 20 May 2011, and (c) 23:02:54 UTC 23 May 2011. Black lines denote the Citation flight track for the constant-temperature leg corresponding to the radar image shown.

remote sensing retrievals or microphysics parameterization schemes that extend to particle sizes larger than in the original dataset.

2.4 Events overview

The Citation aircraft sampled different ice phase environments during the 25 April, 20 May, and 23 May 2011 flights. Jensen et al. (2016) provide an overview of all MC3E cases, while Jensen et al. (2014) give a synoptic scale overview of the MCSs examined in this study. These particular events were chosen because of variations in how the complex of storms evolved and the location of in situ measurements relative to the convective system. Figure 2.5 shows a 0.5° plan-position indicator (PPI) scan of corrected radar reflectivity from the KVNX radar for each event. The PPI was obtained during the middle of the UND Citation flight leg depicted by the black line in Fig. 2.5.

The first event involved an upper-level trough that produced ascent aloft and generated thunderstorms across northern Oklahoma around 06 UTC on 25 April 2011. As these storms traversed northward along an elevated frontal boundary overnight, their bases decoupled from the boundary layer as daytime solar radiation ceased. The discrete cells evolved into an MCS and moved into southern Kansas by 11 UTC (Fig. 2.5a) when the Citation sampled weaker embedded convection and broader stratiform precipitation. The second MCS, with a north-to-south oriented squall line which was part of a larger system, developed from a line of convective cells originating in west Texas along a dry line around 10 UTC on 20 May 2011 and propagated into the deployment region in north central Oklahoma. The Citation aircraft primarily flew within the trailing stratiform region of the MCS (Fig. 2.5b). The third MCS originated as a series of discrete supercell thunderstorms along a surface dry line in western Oklahoma and moved eastward into the MC3E domain by 21 UTC on 23 May 2011 before transitioning to a more linear MCS feature. Microphysical

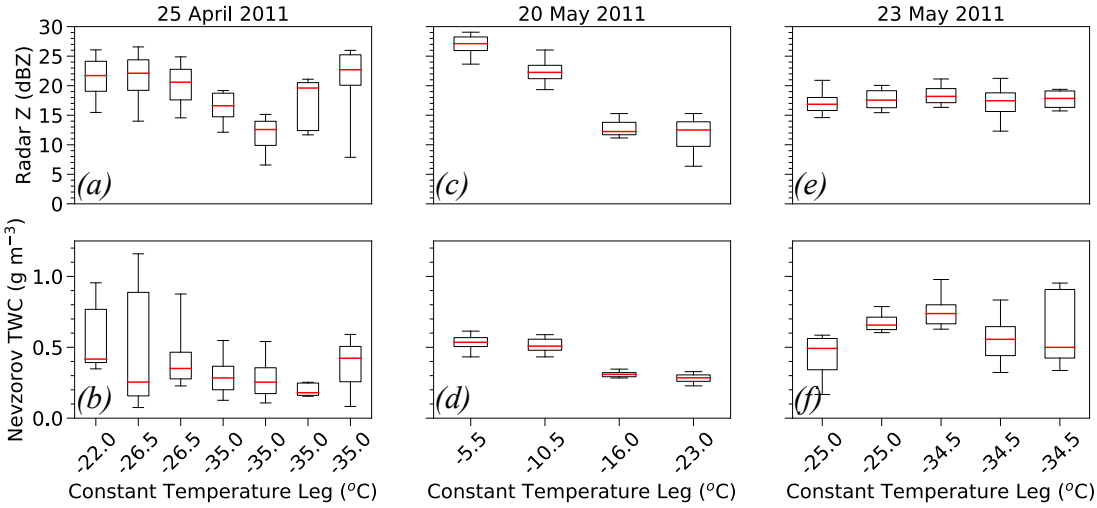

Figure 2.6: Distribution of matched Z (top) and *TWC* from the Nevzorov probe (bottom) for each constant-temperature leg on 25 Apr (left), 20 May (center), and 23 May 2011 (right). Whiskers represent the 5th and 95th percentiles, box edges are the 25th and 75th percentiles, and the line in the middle is the median. Cases where multiple legs of the same temperature exist are shown in chronological order.

measurements were made in the anvil region of these strong thunderstorms (Fig. 2.5c).

To provide context of the bulk characteristics sampled during each event, boxplots of Z matched at the aircraft's location and *TWC* from the Nevzorov probe for each constant-temperature flight leg are given in Fig. 2.6. The whiskers represent the 5th and 95th percentiles from coincident observations, the box edges denote the 25th and 75th percentiles, and the red line in the middle is the median. Distributions are listed in order of decreasing temperature, with instances of multiple legs having the same average temperature shown in chronological order. While the bulk *TWC* and Z may differ for flight legs of similar average temperature on a given day, as in the -26.5 and -35 °C environments on 25 April (Figs. 2.6a-b), greater or smaller *TWC* correlates with greater or smaller Z for most cases. The variability in the *TWC* and Z as it relates to the construction of surfaces of equally plausible *m-D* coefficients is discussed in the next section.

2.5 Results

This section discusses how the (*a,b*) surfaces vary between different cases, as a function of temperature, depending on the determination of radar reflectivity, and depending on whether PSDs had large mass contributions from particles with $D > 4$ mm.

2.5.1 Radar absolute *Z* calibration

While S-band radars within the NEXRAD WSR-88D network are calibrated individually and among one another upon initial installation, biases in *Z* can develop over time (Ice et al., 2017). Zhang et al. (2013) described a technique that uses self-similarity in the *Z*, Z_{DR}, and specific differential phase (K_{DP}) fields to estimate the absolute *Z* bias for events in rain. This method was employed for the cases in this study and biases in *Z* of -1.08 (25 April), -0.65 (20 May), and 1.43 dBZ (23 May 2011) were found. These corrections were applied to the value of *Z* calculated as explained in Sect. 2.3. The surfaces of *m-D* coefficients derived using the matched radar *Z* and that with the bias corrections applied were similar, with the range of equally plausible *b* values differing, on average, by 6.4$\%$ after the corrections were made.

2.5.2 Accounting for mass contributions from larger particles

As discussed in Sect. 2.2.3, the Nevzorov probe is prone to larger particles ($D > 4$ mm) bouncing out of the collection cone resulting in potential *TWC* underestimations. Mass contents were derived from the PSDs using the modified BF95 coefficients to identify time periods in which the contribution of mass from particles with $D > 4$ mm was likely greater than 20$\%$. Of all 10 s PSDs used in this study, 20.9$\%$ had mass contributions from these larger particles exceeding 20$\%$ of the total mass. Figure 2.7 illustrates the similarity in the (*a,b*) surfaces generated using all coincident observations (red shading) and only those using observations with mass from larger particles contributing $\leq 20\%$ of the total mass (blue shading) for the 23 May 2011 event. Regions of overlap between the two approaches only appear as purple shading. The sensitivity test shows that omitting observations where larger particles contribute fractionally more to the total mass yield an area of equally plausible (*a,b*) surfaces for the 23 May event differing, on average, by 1.4$\%$. As such, all coincident observations are used for this study irrespective of the fractional contributions of particles with $D > 4$ mm to the mass.

2.5.3 Environmental impact on *m-D* coefficients

Surfaces of equally plausible *m-D* coefficients in (*a,b*) phase space from all flight legs outlined in Table 2.1 are shown in Fig. 2.8. For each event, flight legs are grouped by the same environmental temperature with the different colors corresponding to the time periods given in each panel. These surfaces are influenced by how *TWC* and *Z* derived from the PSDs relate to observed *TWC* and *Z*, and by the variability of each within a flight leg. The observed trends in the (*a,b*) surfaces and how they are affected by *N(D)*, *TWC*, and *Z* are discussed further below.

To compare surfaces of equally plausible solutions between different environments and also between periods with the same temperature, the percent of overlap between any two flight legs is computed and shown as a matrix in

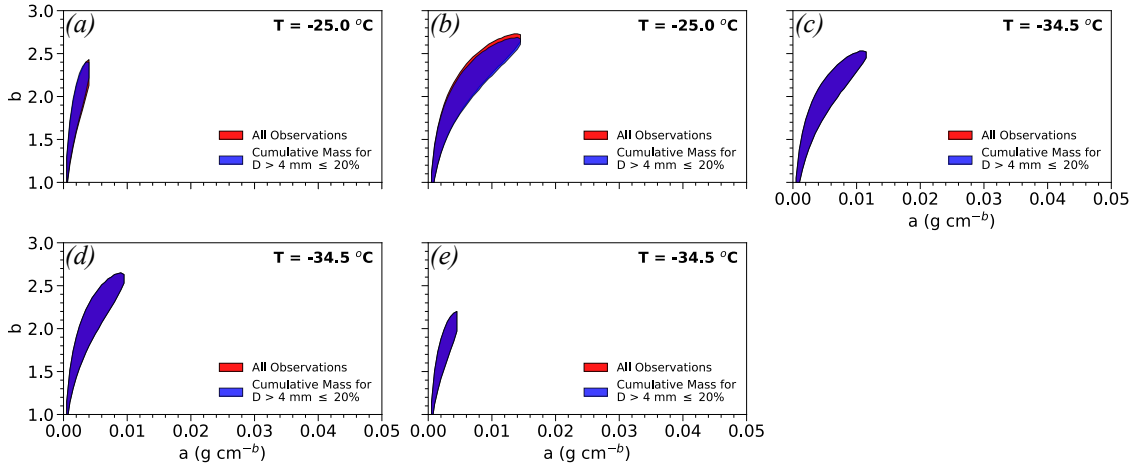

Figure 2.7: Surfaces of equally plausible a and b values from the $m = aD^b$ relation from each near-constant temperature leg on 23 May 2011 for all coincident observations (red) and only those where cumulative mass for $D > 4$ mm is $\leq$ 20 % (blue). Flight legs of the same temperature are shown in chronological order.

Fig. 2.9. The percentage of overlap is determined by counting the number of (*a,b*) pairs contained in both equally plausible surfaces for the conditions listed in the row and column in the matrix and dividing by the number of (*a,b*) pairs in the surface for the condition listed in the row multiplied by 100%. There are two values in the matrix corresponding to each comparison between two flight legs, with differences between the two values resulting from dividing the area of the equally plausible surface from the corresponding column by that in the corresponding row in the matrix. Thus, it is possible for the percentage of overlap between two flight legs to be greater when normalized by an equally plausible surface that is smaller in area, and to be smaller when normalized by a larger equally plausible surface. It is worth noting that the percentage of overlap does not always follow an organized trend with respect to moving away from the gray diagonal line in the matrix as depicted in the top right corner of Fig. 2.9a. The lack of organized overlap values in some regions of the matrix could be influenced by the sensitivity in computing the overlap region over a fine resolution of (*a,b*) values within the domain described in Sect. 2.3, or perhaps could change in a more organized manner if there was a more statistically representative sample for these calculations to be made. Using the (*a,b*) surfaces from the -26.5 °C flight legs on 25 April (Fig. 2.8b) as an example, 62% of the (*a,b*) surface for the 11:05:20–11:14:45 UTC period (labeled -26.5 °C I; Fig. 2.9a) overlaps with the later -26.5 °C flight leg while 65% of the (*a,b*) surface for the 11:21:20–11:34:05 UTC period (labeled -26.5 °C II) overlaps with the earlier -26.5 °C flight leg. The difference occurs because there are 1132 (*a,b*) pairs in the surface for the 11:05:20–11:14:45 UTC period and 1077 (*a,b*) pairs in the surface for the 11:21:20–11:34:05 UTC period. Flight legs having the same temperature are ordered chronologically as in Fig. 2.8 and differentiated with a Roman numeral. Differences of the (*a,b*) surfaces between flight legs are further discussed below.

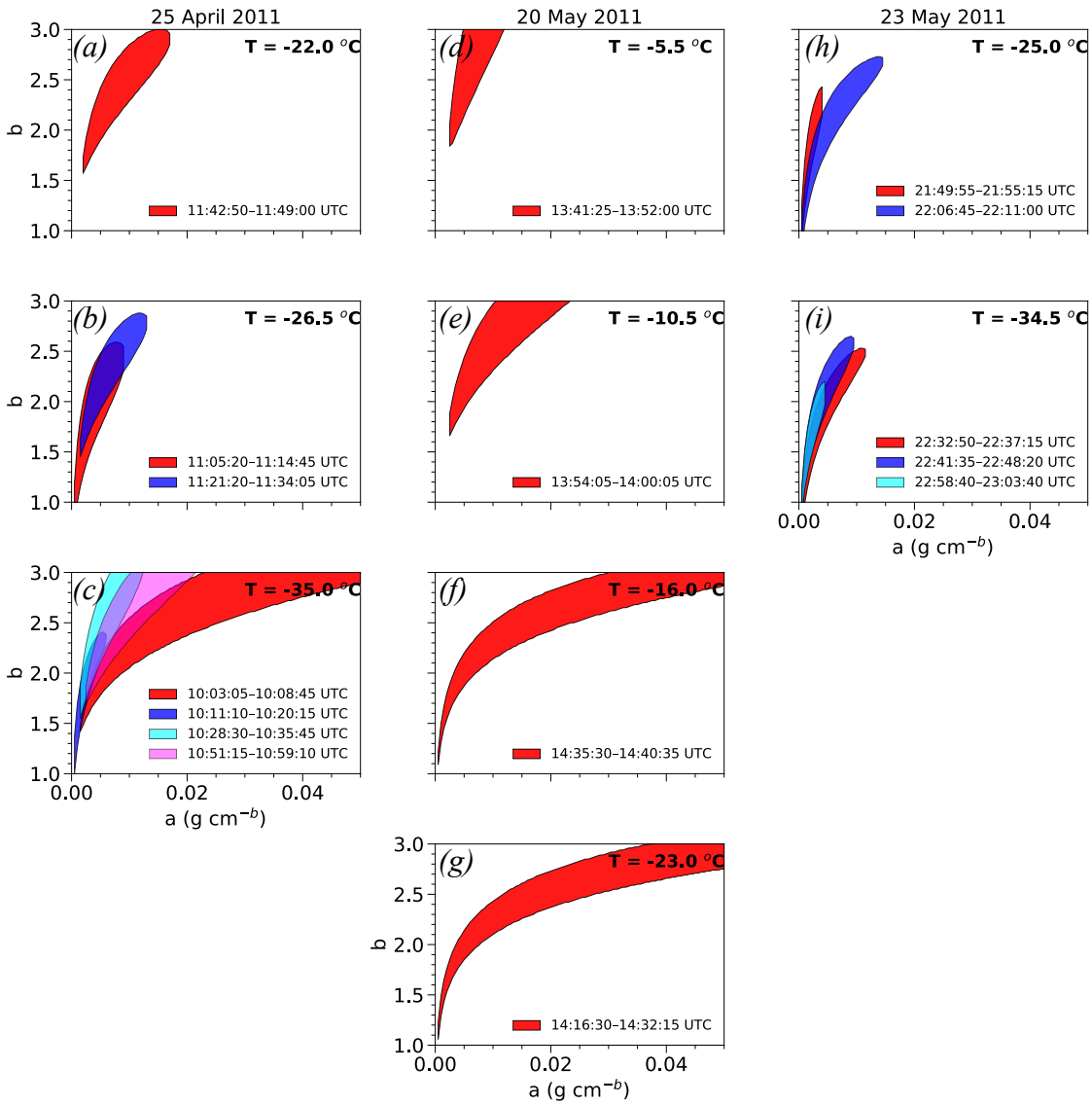

Figure 2.8: Surfaces of equally plausible *a* and *b* values for near-constant temperature flight legs for the (a–c) 25 April, (d–g) 20 May, and (h–i) 23 May 2011 events. Multiple legs occupying the same temperature are assigned a different color within a panel.

25 April case

While differences exist between the (*a,b*) surfaces for the near-constant temperature legs on 25 April (Fig. 2.9a), these surfaces have considerable overlap with each other for $a < 0.01$ g cm$^{-\mathrm{b}}$ and $b < 2.5$ (Figs. 2.8a-c). The -22 and -26.5 °C legs have similar sets of equally plausible solutions, with (*a,b*) surfaces overlapping between 46 and 91% (Fig. 2.9a). Less agreement in the (*a,b*) surfaces is observed among the -35 °C flight legs, with the surfaces overlapping on average 27.8% among the different combinations. The differences in the size of the surfaces is primarily influenced by the natural variability within cloud ($\Delta\chi^2 = \chi^2_{min}$) for 5 of the 7 legs and by the uncertainty due to measurement

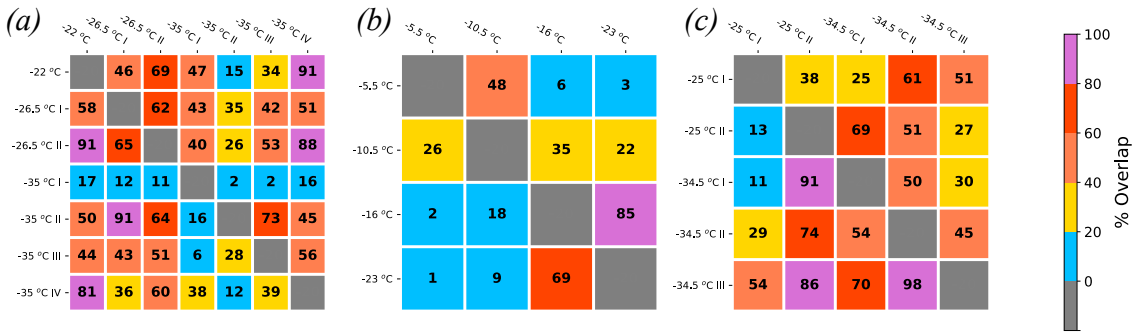

Figure 2.9: Matrix of overlap area between the equally plausible (*a,b*) surfaces corresponding to each row and column for (a) 25 April, (b) 20 May, and (c) 23 May 2011. The overlap area for each square is normalized by the area of the (*a,b*) surface corresponding to the flight leg listed in each row.

errors ($\Delta\chi^2 = \Delta\chi^2_2$) for the remaining legs. The areas of the (*a,b*) surfaces for the -22 and -26.5 °C legs were, on average, 31.2% smaller than the surfaces associated with the -35 °C environment (Figs. 2.8a-c). Three of the four -35 °C legs have surfaces larger than the -22 and -26.5 °C environments as the surface of equally plausible *m-D* coefficients extends beyond the maximum value *a* of 0.017 g cm^{-b} and *b* of 3.00 found for the -22 and -26.5 °C legs. To explain the variation of these (*a,b*) surfaces for the different temperatures, the distributions of microphysical quantities for the times corresponding to these surfaces were examined.

To examine the variability in hydrometeors, particle images and distributions of bulk microphysical properties were analyzed for each flight leg. Example particle images from the HVPS-3, which provide information on the size and habit of ice phase particles with $D > 1$ mm, are plotted in Fig. 2.10. The pictured particles represent a subset of those imaged for the time period given and were chosen at random in an attempt to obtain a representative sample of hydrometeors. Figure 2.11 shows the mean *N(D)* and cumulative mass distribution function *M(D)* using the modified BF95 relationship for each flight leg analyzed in this study. Figure 2.12 details the distribution of number concentration N_t, median mass diameter D_{mm}, and a metric for particle sphericity obtained from the PSDs derived from the 2D-C and HVPS-3 data at each 10 s coincident observation. The D_{mm} is derived using the modified BF95 coefficients to compare among the different flight legs. The whiskers and box edges are the same as in Fig. 2.6. Particle sphericity ζ (McFarquhar et al., 2005; Finlon et al., 2016) is defined by

$$\zeta = A^{1/2}/P, \tag{2.9}$$

where *A* is the cross-sectional area directly measured by the probe and *P* is the perimeter determined from the sum of all pixels within one diode width of the edge of the particle and the diode resolution. Finlon et al. (2016) described how higher ζ denotes more-circular particles. Sphericity values shown in Fig. 2.12 represent a mass-weighted mean of ζ for all particles using mass estimated from the modified BF95 relation within each 10 s observation. Figures 2.10,

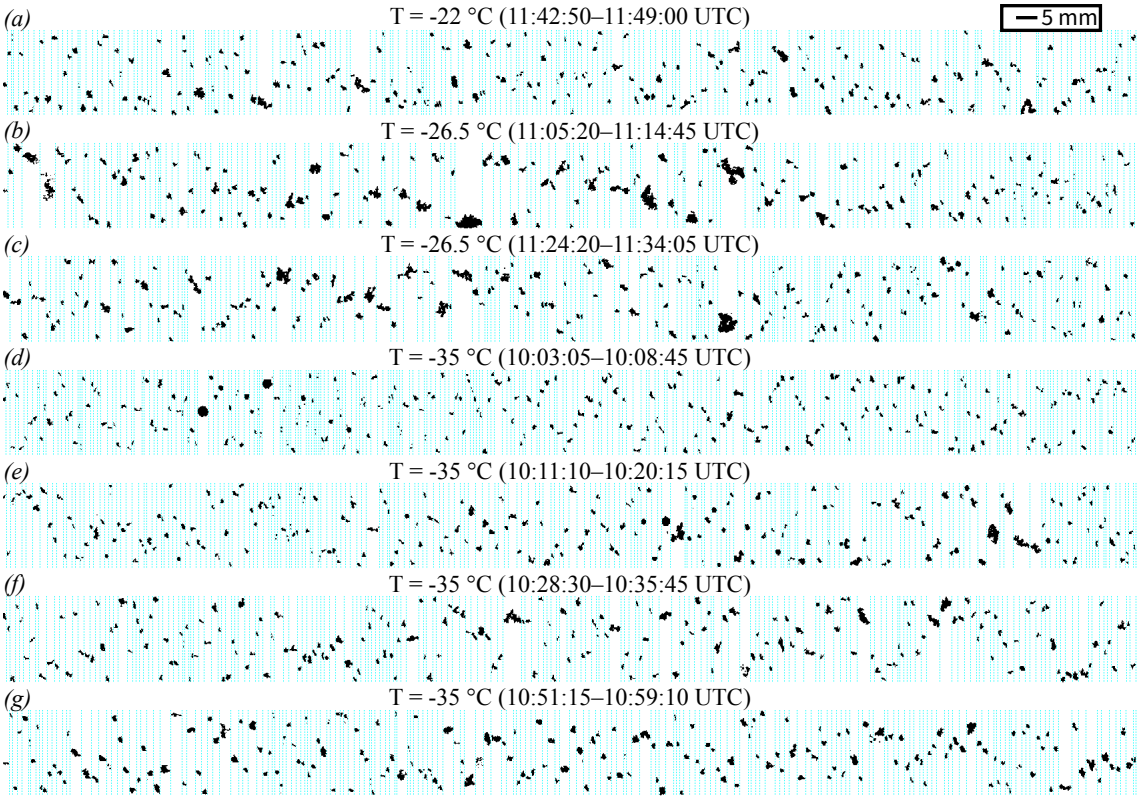

Figure 2.10: Representative particle images from the HVPS-3 for each near-constant temperature flight leg on 25 April 2011.

2.11, and 2.12 are ordered in the same manner as in Fig. 2.6, with instances of multiple legs having the same average temperature shown in chronological order.

As evidenced by the particle images and mean *N(D)* at T = -22 and -26.5 °C (Figs. 2.10a-c, 2.11a), the presence of aggregates exceeding 5 mm is more common compared to lower temperatures (Figs. 2.10d-g) where the ice crystals and aggregates appear to be skewed towards smaller sizes. Distributions of D_{mm} (Fig. 2.12b) and *TWC* (Fig. 2.6b) also indicate this trend, with a median D_{mm} for the 11:05:20–11:14:45 UTC (T = -26.5 °C) flight leg of 2.2 mm while the -35 °C periods have median D_{mm} ranging between 1.1 and 1.7 mm.

To illustrate that the range of equally plausible (*a,b*) coefficients is sometimes explained more by the variability of cloud parameters than the uncertainty in measurement errors, the distributions of bulk microphysical variables, *TWC*, and *Z* are compared between the 11:05:20–11:14:45 UTC (T = -26.5 °C) and 10:03:05–10:08:45 UTC (T = -35 °C) periods. The -26.5 °C flight leg had ranges in N_t, D_{mm}, sphericity, *Z*, and *TWC* between the 25th and 75th percentiles (interquartile range hereafter) of 21.5 L^{-1}, 1.3 mm, 0.04, 5.2 dBZ, and 0.73 g m^{-3}, respectively, while the same variables for the -35 °C period had smaller interquartile ranges of 7.4 L^{-1}, 0.1 mm, 0.02, 4.0 dBZ, and 0.17 g m^{-3} (Figs. 2.6a,b; 2.12a-c). The distribution of χ^2 in (*a,b*) phase space is expected to differ when the variability in *N(D)*

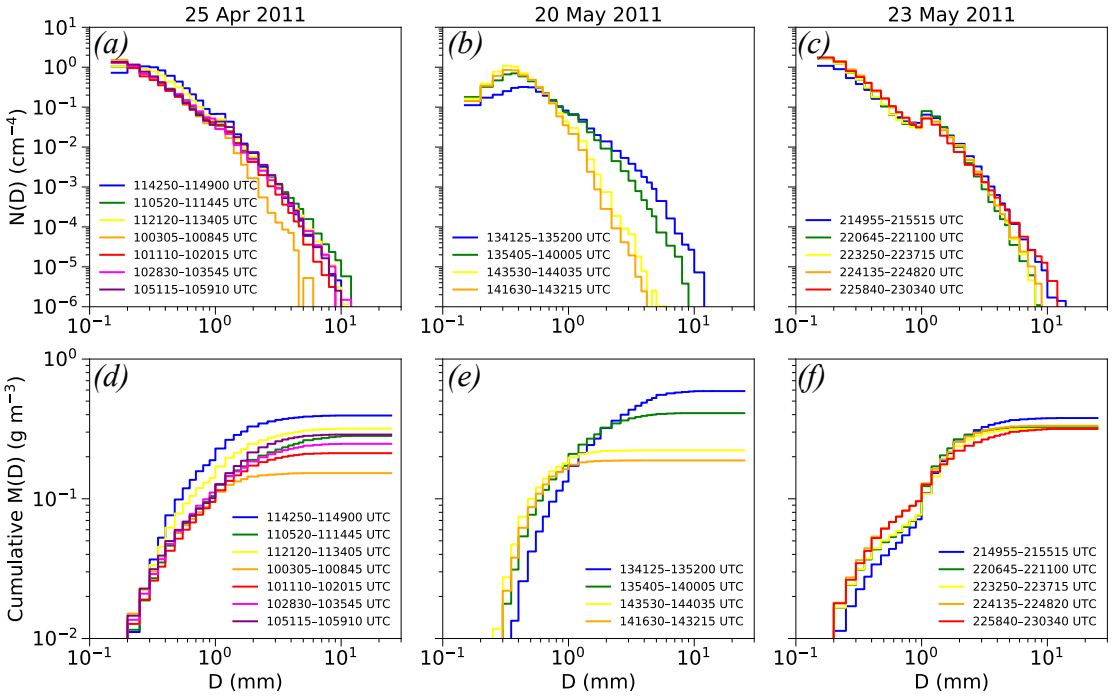

Figure 2.11: Mean *N(D)* (top) and cumulative *M(D)* (bottom) for each constant-temperature leg on 25 Apr (left), 20 May (center), and 23 May 2011 (right). Cases where multiple legs of the same temperature exist are shown in chronological order.

throughout a flight leg is different between two periods since different a and b are likely to yield TWC_{SD} and Z_{SD} similar to the observed *TWC* and *Z*. Figure 2.13 illustrates the distribution of χ^2 for the two periods, with the outlined region representing χ^2 values that are ≤ 2 for comparison. The region containing $\chi^2 \leq 2$ is 90.8% smaller for the -26.5 °C flight leg compared to the -35 °C period and indicates that the TWC_{SD} and Z_{SD} derived from all possible a and b remain fairly consistent over the course of the -26.5 °C flight leg due to the smaller interquartile ranges in the *TWC*, *Z*, and bulk microphysical properties. As such, low χ^2 values are present over a larger range of *m-D* coefficients for the -35 °C leg.

Although the distribution of χ^2 is an important factor in determining the area of an equally plausible surface, the $\Delta\chi^2$ confidence region, which is equal to χ^2_{min} ($\Delta\chi^2_2$) for 4 (3) of the flight legs on this day, can also influence the area of (a,b) surfaces. While the allowable tolerance is a factor of 2 greater for the -26.5 °C leg, the equally plausible (a,b) surface is 3.4 times smaller compared to the -35 °C flight leg (Figs. 2.8b,c) because of the magnitude and distribution of χ^2 values in (a,b) phase space. Put another way, more χ^2 values considered within the (a,b) phase space are greater than the $\chi^2_{min} + \Delta\chi^2$ criteria to be considered equally plausible solutions compared to the -35 °C leg.

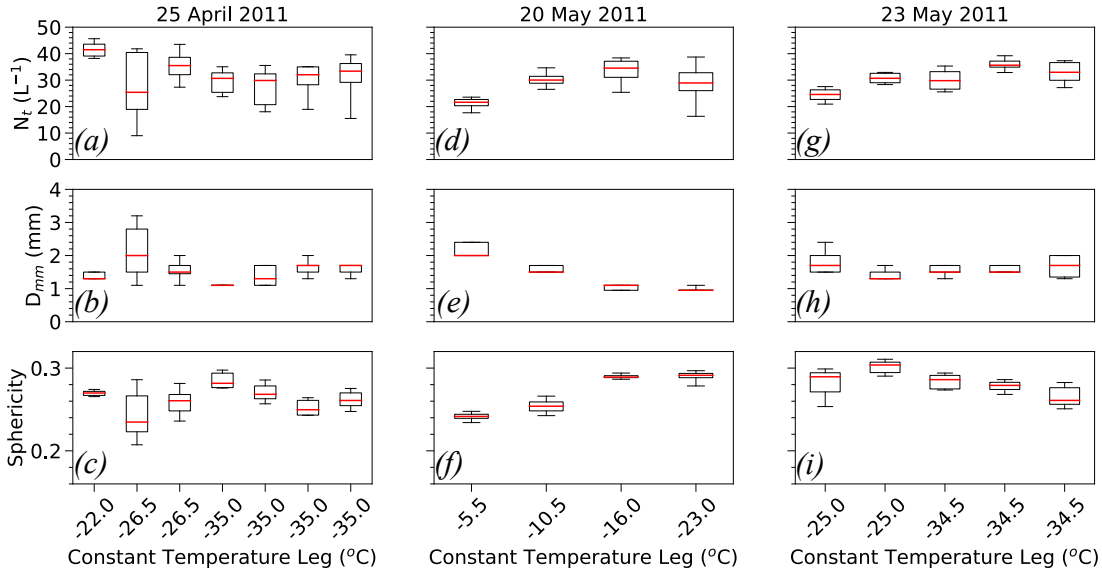

Figure 2.12: As in Fig. 2.6, but for number concentration N_t, median mass diameter D_{mm}, and mass-weighted mean sphericity.

20 May case

The wide range of temperatures sampled during the 20 May event was associated with a large variation in Z (Fig. 2.6c), with median values ranging between 12.5 dBZ (T = -23 °C) and 27.1 dBZ (T = -5.5 °C). Representative particle images (Fig. 2.14) highlight differences in particle size and habit between the higher temperature flight legs (T = -5.5 and -10.5 °C) and the lower temperature periods (T = -16 and -23 °C), with images and mean $N(D)$ (Fig. 2.11b) from the -5.5 and -10.5 °C legs indicating a greater frequency of larger ice crystals and aggregates with $D \geq 2$ mm.

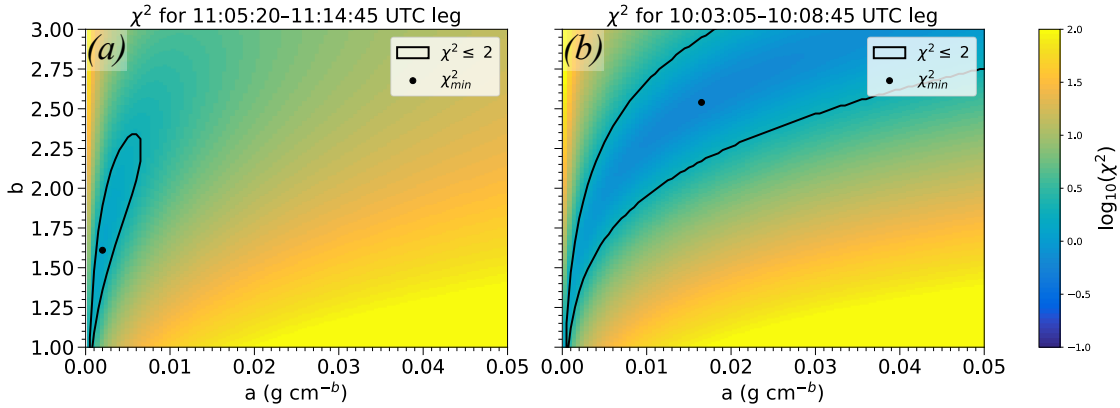

Figure 2.13: χ^2 statistic in (a,b) phase space for the (a) 11:05:20–11:14:45 UTC and (b) 10:03:05–10:08:45 UTC flight legs on 25 April 2011. Outlined regions represent $\chi^2 \leq 2$ and the dots χ^2_{min}.

A Mann-Whitney U test confirms that D_{mm} (Fig. 2.12e) and sphericity (Fig. 2.12f) between the higher and lower temperature environments are statistically different at the 99% confidence level, with notably larger and less spherical particles observed during the -5.5 and -10.5 °C flight legs. Further, median *Z* for the -5.5 and -10.5 °C periods (22.3–27.1 dBZ) are up to 30.7 times greater than for the -16 and -23 °C legs (12.2–12.5 dBZ) while the median *TWC* are up to 1.9 times (0.3 g m^{-3}) greater for the -5.5 and -10.5 °C legs. Thus, the difference in particle properties and bulk properties *TWC* and *Z* can be used to explain differences in (*a,b*) coefficients observed between the legs on this day.

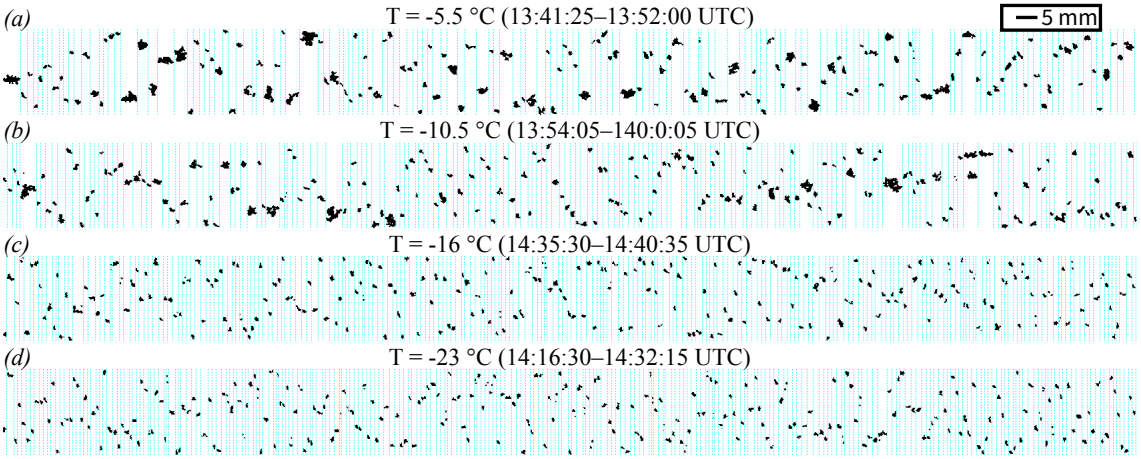

Figure 2.14: Same as in Fig. 2.10, but for the 20 May 2011 case.

Microphysical properties such as the effective density ρ_e of ice hydrometeors can impact *TWC* differently than they do *Z*. The ρ_e, defined here as the ratio of *TWC* derived assuming the modified BF95 relationship to the integrated volume of particles enclosed by an oblate spheroid with an aspect ratio of 0.6 (e.g., Hogan et al., 2012), is estimated to evaluate its influence on *TWC* and *Z*. Median ρ_e ranges between 0.05 and 0.08 g cm^{-3} for the -5.5 and -10.5 °C periods and between 0.18 and 0.21 g cm^{-3} for the -16 and -23 °C flight legs. These trends along with minimal riming evident from the 2D-C particle images suggest that particles are on average less compact for the higher temperature legs. Further, the presence of larger aggregates as suggested by greater values of D_{mm} (Fig. 2.12e), lower sphericity (Fig. 2.12f) and ρ_e, and the representative particle images from the HVPS-3 (Figs. 2.14a,b) are consistent with increasing *Z* when observed by longer wavelength radars (e.g., Giangrande et al., 2016).

Since differences in ρ_e appear to affect the *TWC* and *Z* on 20 May, the variability in *N(D)* is not the only factor influencing the equally plausible (*a,b*) surfaces depicted in Figs. 2.8d-g. Figure 2.9b illustrates that only the -16 and -23 °C legs have similar (*a,b*) surfaces, with 85% of the (*a,b*) coefficients from the -16 °C leg overlapping with the -23 °C flight leg. Minimum values of *b* for the -5.5 and -10.5 °C flight legs, where less compact particles were observed, were 1.84 and 1.66, respectively, while minimum *b* for the -16 and -23 °C legs were 1.09 and 1.06 for similar *a* (Figs. 2.8d-g). Looking at the (*a,b*) surfaces another way, values of *a* for the -5.5 and -10.5 °C legs were as large as 0.031 g cm^{-b} while *a* exceeds 0.05 g cm^{-b} for $b = 3$ during the -16 and -23 °C flight legs. Although the $\Delta\chi^2$

confidence region is equal to $\Delta\chi^2_2$ for the 4 flight legs on this day and has $\Delta\chi^2$ values that are within 1% of each other, the distribution of χ^2 greatly influences the extent of these surfaces in (*a,b*) phase space with an area for the -5.5 and -10.5 °C flight legs that is on average 2.9 times smaller than the the -16 and -23 °C periods. When considering the $m = aD^b$ relation whose size D and exponent b are held fixed, lower values of a as observed during the -5.5 and -10.5 °C legs suggest that particles on average have smaller m compared to the -16 and -23 °C legs and are consistent with smaller ρ_e observed for the -5.5 and -10.5 °C periods.

23 May case

The 23 May case was unique from the other two cases in that the bulk Z varied less between the different temperature environments (Fig. 2.6e), with median Z ranging only between 16.9 and 18.2 dBZ. Representative particle images (Fig. 2.15) in addition to the mean *N(D)* (Fig. 2.11c) and the cumulative *M(D)* (Fig. 2.11f) indicate that the sizes and shapes of ice hydrometeors are similar for all five flight legs. Additionally, distributions of D_{mm} (Fig. 2.12h) and sphericity (Fig. 2.12i), with median values of each varying by 0.4 mm and 0.04 respectively, further support this similarity in cloud properties between the different environments. Equally plausible (*a,b*) surfaces were also similar irrespective of temperature (Figs. 2.8h,i), with the four flight legs after the 21:49:55–21:55:15 UTC period having surfaces that overlap on average 62.1% among the different combinations (Fig. 2.9c). The 21:49:55–21:55:15 UTC leg is the only period on this day where the $\Delta\chi^2$ confidence region is determined by the natural variability in the cloud (χ^2_{min}) rather than the uncertainty due to measurement errors ($\Delta\chi^2_2$). As such, the (*a,b*) surface for this period has minimal overlap with the other equally plausible surfaces. Closer examination of the bulk *TWC* (Fig. 2.6f) indicates that values at the fifth percentile for the 21:49:55–21:55:15 UTC period are 65.2% less than the remaining flight legs, which impacts the distribution of χ^2 values and the (*a,b*) values that are within the $\chi^2_{\text{min}} + \Delta\chi^2$ threshold.

Although surfaces of equally plausible solutions trend larger in area for lower temperature environments on 25 April and 20 May, the area of (*a,b*) surfaces among the five flight legs on 23 May are on average 2.2 (3.8) times smaller compared to the 25 April (20 May) event. To examine how the distribution of χ^2 in (*a,b*) phase space is affected by differences in the variability of *TWC* and Z throughout a flight leg, the 14:16:30–14:32:15 UTC period on 20 May and the 21:49:55–21:55:15 UTC period on 23 May are compared because of their similar temperature and $\chi^2_{\text{min}} + \Delta\chi^2$ threshold used to determine the (*a,b*) surfaces. Figure 2.16 illustrates the distribution of χ^2 for the two periods, with the outlined region representing χ^2 values that are ≤ 1 for the purpose of comparison. The region containing $\chi^2 \leq 1$ is 88.2% smaller for the 23 May flight leg compared to the 20 May period, and highlights how different a and b can yield a χ^2 value that is within the given tolerance based on differences in the observed *TWC* and Z distributions. When bulk *TWC* and Z are compared against the 25 April (20 May) events, the median Z from flight legs on 23 May is on average 34.4% (25.9%) lower while the median *TWC* is 90.3% (43.9%) greater. As mentioned

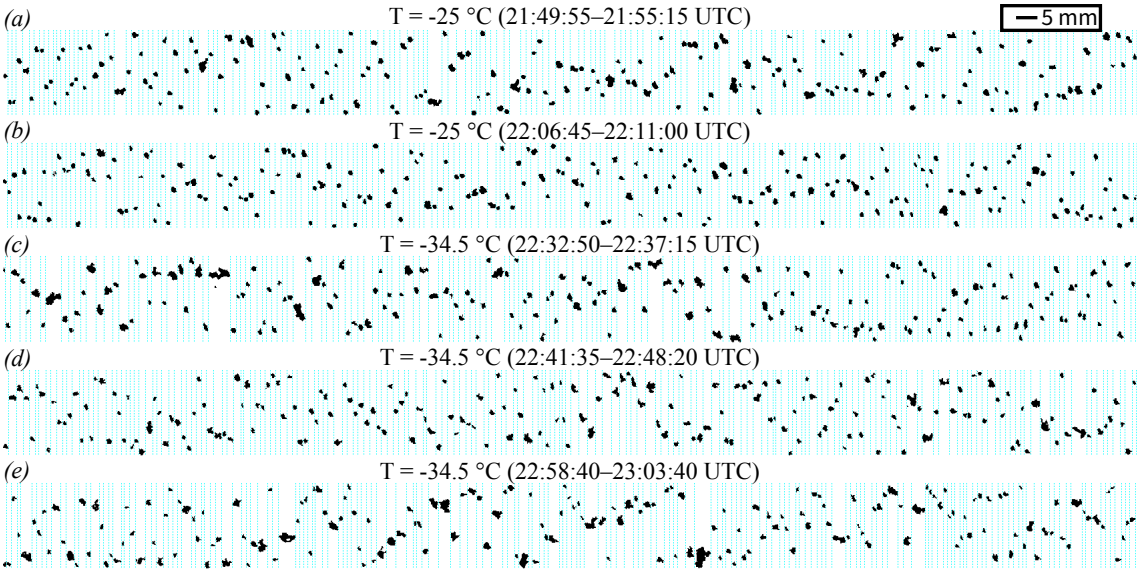

Figure 2.15: Same as in Fig. 2.10, but for the 23 May 2011 case.

in Sect. 2.4, the sampling strategy on 23 May was different from the stratiform clouds observed with the previous two events in that measurements were primarily made in the anvil region of supercell thunderstorms. Previous studies (e.g., Heymsfield et al., 2007) noted that the prefactor a had less of a temperature dependence within anvil cirrus clouds, consistent with trends in a for the 23 May flight legs.

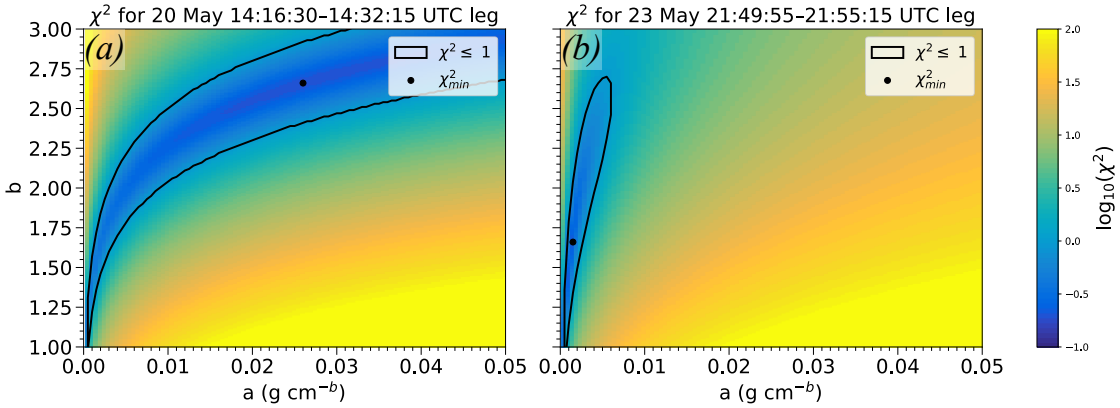

Figure 2.16: Same as in Fig. 2.13, but for (a) 14:16:30–14:32:15 UTC on 20 May and (b) 21:49:55–21:55:15 UTC on 23 May 2011. Outlined regions represent $\chi^2 \leq 1$ and the dots χ^2_{min}.

2.6 Conclusions

This chapter presented a novel approach to characterize the variability of mass-Dimension (*m-D*) coefficients characterizing particle size distributions (PSDs) during the Mid-latitude Continental Convective Clouds Experiment (MC3E).

The technique outlined here extends the approach of McFarquhar et al. (2015), who derived a volume of equally realizable solutions in the phase space of gamma fit parameter coefficients to characterize PSDs. Ground-based radar measurements of reflectivity *Z* from the Vance Air Force Base, OK radar were matched to the location of the Cessna Citation II aircraft where total water content (*TWC*) measurements from the Nevzorov probe were made and PSDs were derived from optical array probe data. These collocated datasets permitted use of a χ^2 minimization technique where all χ^2 within a tolerance $\Delta\chi^2$ of the minimum χ^2 were considered equally plausible solutions to the $m = aD^b$ relationship for a flight leg of similar temperature. The tolerance was determined by considering uncertainties due to natural variability of cloud conditions for a particular environment, the statistical sampling of particles from the PSDs, and uncertainties in the measurements themselves.

The key findings of this chapter are as follows:

1. The distribution of χ^2 values in (*a,b*) phase space shows that the *a* and *b* parameters are highly correlated, as expected. The degree to which these χ^2 values vary throughout a flight leg is influenced by how the PSDs, *TWC* from the Nevzorov probe, and *Z* from radar vary within a flight leg of similar temperature. Flight legs that have little variability in the microphysical properties and an allowable tolerance equal to the minimum χ^2 in (*a,b*) phase space, such as the 10:03:05–10:08:45 UTC period on 25 April, occupy a surface area in (*a,b*) phase space that is up to 8.7 times larger than flight legs where microphysical properties vary more, such as the 11:05:20–11:14:45 UTC leg on the same day.

2. Surfaces of equally plausible solutions appear dependent on temperature for the 25 April and 20 May events. The range of plausible *a* and *b* coefficients is larger for flight legs of lower temperature, and 80% of the surfaces compared between the lowest and highest temperature for each day overlap by less than 50%.

3. Cases with little dependence of the surfaces of equally plausible solutions on temperature, like the flight legs analyzed on 23 May, can be explained in terms of the regions of cloud sampled and the types of ice hydrometeors observed. A mean overlap of 62.1% between four of the five (*a,b*) surfaces on that day is consistent with previous studies (e.g., Heymsfield et al., 2007) that note little dependence in the *a* coefficient with temperature in anvil cirrus clouds.

4. The minimum χ^2 in (*a,b*) phase space determines the allowable tolerance $\Delta\chi^2$ for 5 of the 16 flight legs when determining the set of equally plausible *a* and *b* coefficients, whereas the combined uncertainty due to measurement error from the OAPs, Nevzorov *TWC* probe, and radar determines the $\Delta\chi^2$ for the remaining 11 flight legs. This means that the uncertainty in the *m-D* coefficients is driven by uncertainties in the measurements the majority of the time, with the natural parameter variability over a flight leg a driving factor for 31% of the flight legs observed. Thus, efforts to reduce measurement errors could reduce the uncertainty in derived (*a,b*)

coefficients.

5. The covariability of a and b permit possible solutions of $b > 3$ for the ranges of particle sizes observed in 7 of the 16 flight legs analyzed. For these flight legs this covariability means that Z derived from a and b and the PSDs is still within 82.4% of the mean matched radar Z, which is marginally greater than the 50.5% difference when b is not greater than 3.

6. Flight legs where the cloud particles have lower effective density ρ_e, such as the -5.5 and -10.5 °C flight legs on 20 May, yield minimum b values in (a,b) phase space as much as 0.78 larger than clouds with a higher ρ_e like the -16 and -23 °C legs on the same day. These differences can be explained by the different impacts of ρ_e on *TWC* compared to Z.

A key finding of this study is that a range of a and b coefficients should be considered as equally plausible for a given environment due to the natural variability of cloud conditions and measurement uncertainties, even within a similar temperature range. This variability results in a large range of a and b as equally plausible solutions (as indicated in this study), and could explain the range in *m-D* coefficients determined in past studies (Fig. 2.1) where a coefficients can vary by 3 orders of magnitude and b coefficients between 1 and 3 for measurements made in similar environmental conditions. The technique used in this study provides insight into how equally plausible *m-D* coefficients can arise because the dependence of derived microphysical parameters on environmental conditions is sometimes more important than measurement uncertainties based on the instruments used to collect the data, but is not always the case. Further, it is shown that the dependence of the (a,b) coefficients on temperature is still notable even when considering the ranges of equally plausible solutions. Future studies should further ascertain the extent to which the dependence of (a,b) on other environmental parameters is robust enough to be distinguished from the natural variability of the surface or its variability due to measurement errors.

While representing *m-D* coefficients as a range of equally plausible solutions may address shortcomings of microphysical parameterization schemes and remote sensing retrievals that employ a single *m-D* relationship for a given ice species or environment, caution should be taken if the results presented here are applied to ranges of particle size or environments outside of those sampled (e.g., ones with different observed habits or various degrees of riming). The results presented here illustrate that similar *TWC* and Z can be obtained regardless of the a and b values chosen, with coefficients randomly selected from a surface of solutions allowing one to represent how the uncertainty in (a,b) impacts any derived quantity. Thus, the large variability in derived (a,b) for an equally plausible surface does not necessarily indicate there is a large uncertainty in quantities derived using the a and b coefficients. Future work should assess how the representation of modeled processes and retrieved quantities are influenced by the variability in a and b coefficients as well as which environmental drivers and cloud microphysical properties influence the size of derived

surfaces of equally plausible solutions, and the extent to which measurement errors need to be reduced to better refine these surfaces. The approach presented in this study can be applied to additional studies that make use of collocated radar and microphysical measurements in other cloud and meteorological environments, and improve the statistical robustness of plausible *m-D* parameters for given environmental conditions. Such studies may help to further understand how surfaces of equally plausible (*a,b*) solutions are affected by different environments and the variability of cloud conditions therein, as well as the dependence of these solutions as a function of other cloud or environmental properties.

Chapter 3

Environmental dependence of mass-dimension relationships from three GPM ground validation campaigns

This chapter uses the Finlon et al. (2019) technique to characterize the dependence of mass-dimension relationships as a function of environmental temperature and ice water content from the Mid-latitude Continental Convective Clouds Experiment, Global Precipitation Measurement (GPM) Cold Precipitation Experiment, and Olympic Mountains Experiment. These campaigns represent a subset of GPM ground validation field experiments that have been conducted in recent years to validate the radar retrievals from the GPM constellation of satellites.

3.1 Introduction

The relationship between ice particle mass m and maximum dimension D is typically represented as an $m = aD^b$ power law for use in numerical models and remote sensing retrievals. These *m-D* relations are typically formulated by minimizing the difference between a bulk microphysical property derived from a particle size distribution (PSD) such as total water content (TWC) or reflectivity (Z) and that directly measured by an independent instrument such as a TWC probe or radar. Numerous studies have derived *m-D* relations for measurements made in a variety of conditions (e.g., Brown and Francis, 1995; Heymsfield et al., 2010; Cotton et al., 2013; Fontaine et al., 2014) or partitioned by habit (e.g., Locatelli and Hobbs, 1974; Mitchell et al., 1990; Schmitt and Heymsfield, 2010), among other factors. Chapter 2 illustrated the wide range in *m-D* coefficients that exists from studies dating back to Nakaya and Terada (1935), with the prefactor a in the *m-D* relationship spanning 5 orders of magnitude and the exponent b ranging in value from 1 to greater than 3.

Research since the 1940s has suggested that ice particle habits, characterized as having similar density and morphological properties, are related to temperature, pressure, and ice supersaturation (e.g., Weickmann, 1945; Magono and Lee, 1966; Pruppacher and Klett, 1997; Bailey and Hallett, 2004, 2009). Although crystals are not necessarily observed where they form, these findings have motivated attempts to explore the temperature dependence of *m-D* coefficients (e.g., Heymsfield et al., 2007, 2013; McFarquhar et al., 2007a; Fontaine et al., 2014; Erfani and Mitchell, 2016) while still acknowledging the heterogeneity of ice crystal habit species occurring over narrow ranges of temperatures.

While temperature-dependent *m-D* relations may be considered an improvement over single values of *a* and *b* often used in retrievals and model applications, most studies have not considered the spatial variability of microphysical properties or the uncertainties in the acquired measurements (Baumgardner et al., 2017; McFarquhar et al., 2017), the statistical counting errors (Hallett, 2003; McFarquhar et al., 2007b), and other uncertainties. Of the studies that estimated uncertainties in the *a* and/or *b* coefficients, some have used optimal estimation techniques (Maahn et al., 2015; Xu and Mace, 2017; Mascio and Mace, 2017) while others applied uncertainties in the measured *Z*, PSDs, or morphological properties (Fontaine et al., 2014; Erfani and Mitchell, 2016).

Analogous to the approach of McFarquhar et al. (2015), Chapter 2 characterizes the variability of *m-D* relationships for different environments during the Mid-latitude Continental Convective Clouds Experiment (MC3E), co-sponsored by the U.S. Department of Energy and the National Aeronautics and Space Administration, by minimizing the chi-square difference between moments derived from a PSD and those measured by a TWC probe and radar. Subsequently Chapter 2 applied an allowed tolerance about the minimum chi-square based on the natural parameter variability and measurement uncertainties to determine a range of (*a,b*) coefficients that are considered equally realizable.

This study uses the techniques introduced in Chapter 2 to examine the dependence of *m-D* relations on *T* and bulk ice mass content (IWC). Data from 3 Global Precipitation Measurement (GPM) ground validation (GV) field experiments are used in order to better understand the behavior of *m-D* relationships for a wide range of environmental and geographic conditions, and to determine these relations in a way that can be implemented within remote sensing retrieval schemes and microphysical parameterization routines.

The remainder of this chapter is organized as follows. Section 3.2 describes the datasets analyzed, the methodology used to process the data, and the procedure employed to develop surfaces of equally plausible *m-D* coefficients for a given environment. A summary of the conditions sampled in the field experiments studied is outlined in section 3.3, and the influence of temperature *T*, and IWC on the *m-D* coefficients is explored in sections 3.4 and 3.5. A summary of major findings and implications for microphysical parameterizations and remote sensing retrievals are discussed in section 3.6.

3.2 Data and methodology

Data collected during the 2011 MC3E field campaign, the 2012 GPM Cold Precipitation Experiment (GCPEx), and the 2015 Olympic Mountain Experiment (OLYMPEX) are used in this chapter. A combination of cloud microphysical instruments aboard the University of North Dakota (UND) Cessna Citation II aircraft and ground-based radars permitted derivation of the *m-D* parameters presented here. The ground-based and airborne instrumentation pertinent to the current study are summarized in Table 3.1 and described below.

Table 3.1: Summary of the radar and microphysical instruments pertaining to this study used during the Mid-latitude Continental Convective Clouds Experiment (MC3E, left), GPM Cold Precipitation Experiment (GCPEx, middle), and Olympic Mountains Experiment (OLYMPEX, right).

Instrument	MC3E	GCPEx	OLYMPEX
Radar	Vance Air Force Base, OK, USA (KVNX)	King City Radar, ON, Canada (CWKR)	Langley Hill, WA, USA (KLGX)
Radar Wavelength	10 cm (S-band)	3 cm (C-band)	10 cm (S-band)
TWC Probe	←——Nevzorov TWC Probe (120° deep cone)——→		
OAPs Used	2D-C, HVPS-3	CIP, HVPS-3	2D-S, HVPS-3
OAP Resolution	30 μm, 150 μm	25 μm, 150 μm	10 μm, 150 μm
OAP Size Range	←——0.15–1.0 mm, 1.0–19.2 mm——→		

3.2.1 Identification of coincident aircraft/radar data

During these three experiments, the UND Citation sampled cloud properties in-situ within the volume being sampled remotely by the radar. Chapter 2 describes the methodology and criteria used to determine whether the in-situ measurements and radar retrievals were sufficiently close in time and space, hereafter called a coincident point. The radar matching algorithm used to calculate radar Z in the vicinity of each 10-s averaged aircraft property (Nesbitt et al., 2019) identifies radar gates within a specified radius of influence and applies the Barnes (1964) interpolation technique to obtain an average Z. Following Chapter 2, a 500-m radius of influence was chosen to allow a sufficient number of gates to be considered for the interpolation procedure while limiting the vertical extent of radar gates since microphysical properties can vary considerably in the vertical. When alternately using a 250 m (1 km) radius of influence, the root mean square difference (RMSD) in the matched Z was 0.65 (0.55) dBZ for all coincident points during MC3E, 0.93 (0.61) dBZ for GCPEx, and 0.63 (0.34) dBZ for OLYMPEX. These differences are minimal compared to typical uncertainties of 1 dBZ in radar reflectivity measurements (section 3.2.4).

Measurements taken during flight legs of near-constant temperature and spiral ascents and descents are considered in the analysis. Section 3.2.4 describes how the coincident observations were partitioned into specific environmental conditions to obtain *m-D* parameters for each T and IWC category.

Determination of *m-D* relations for ice particles is simplest when the PSDs, TWC, and Z are unaffected by liquid water. The remainder of this subsection describes a set of criteria that are applied to ensure that only ice phase hydrometeors of sufficient quality are used in the analysis. First, the mean T must be $<$ -5 °C to avoid melting of ice particles and prevent contamination of the radar bright band. Second, the mean TWC must be $\geq$ 0.05 g m^{-3} as the observation is either below or too close to the noise threshold of the Nevzorov probe. Finally, measurements from the Rosemount Icing Detector (RID) and cloud droplet probe (CDP) are used to ensure that supercooled liquid water

(SLW) was not present. After smoothing the RID frequencies with a 1D Gaussian filter, time periods where frequency changes of $\leq$ -1 Hz s^{-1} corresponding to vibration changes of the RID wire from the accretion of SLW and of $>$ 2 Hz s^{-1} corresponding to the heating of the wire to melt the SLW, and points within $\pm$ 2 s are identified as potentially contaminated by SLW. If fewer than 5 s elapsed between periods of potential SLW, all 1-s samples in the interval are also flagged as potential SLW.

Finally, periods with CDP concentrations $>$ 10 cm^{-3} (Hobbs and Rangno, 1998; Cober et al., 2001; Lance et al., 2010; Heymsfield et al., 2011) were also identified as potential SLW as SLW can occur for RID frequency changes of $>$ -1 Hz s^{-1} in periods of light icing. Particle images from a 2D cloud (2D-C) probe for MC3E, a cloud imaging probe (CIP) for GCPEx, and a 2D stereo (2D-S) probe for OLYMPEX were examined along with a cloud particle imager were examined during these periods of light icing to verify whether the CDP correctly detected circular water drops when the RID frequency changed slowly or not at all over the 10-s period. Analysis of particle images indicate that the $>$ 10 cm^{-3} CDP concentration threshold compliments the RID frequency derivative threshold for periods when marginal amounts of SLW are present. After removing time periods with SLW, the analysis is constrained to periods when ice-phase hydrometeors dominate the observed PSD such that TWC $\approx$ IWC. Therefore, bulk mass content values from the Nevzorov probe are hereafter referred to as IWC.

After the above criteria are considered, a total of 6119 10-s periods are used among the flights analyzed for this study. The number of coincident points are provided for each flight in Table 3.2.

3.2.2 Radar measurements

Data from the Vance Air Force Base, OK (KVNX), Langley Hill, WA (KLGX) Weather Surveillance Radar-1988 Doppler (WSR-88D) radars and the King City, Ontario (CWKR) radar are used in the analysis for the MC3E, OLYMPEX, and GCPEx events, respectively. Given the reduced effect of non-Rayleigh scattering on larger hydrometeors (e.g., Lemke and Quante, 1999; Matrosov, 2007) and attenuation through liquid regions of cloud (e.g., Bringi et al., 1990; Park et al., 2005; Matrosov, 2008), use of the KVNX and KLGX S-band (10-cm wavelength) radars and the CWKR C-band (3-cm wavelength) radar are preferred over nearby research radars that transmit at higher frequencies and may be more susceptible to attenuation and non-Rayleigh scattering.

While radars within the US Next Generation Weather Radar (NEXRAD) WSR-88D network are calibrated upon installation, biases in Z can develop over time (Ice et al., 2017). The approach of Zhang et al. (2013) was thus applied to determine the bias in Z for each event using the self-similarity in multiple radar polarimetric variables for regions in rain. The biases in Z range between -1.08 and 1.43 dBZ for the MC3E events and between 0.18 and 2.36 dBZ for the OLYMPEX events. The self-similarity technique is not applied for the GCPEx events examined here as no bright band was observed by the CWKR radar and as such the precipitation did not fall as rain. The radar, however, is calibrated

every 3–4 months to determine the absolute gain and bias of the antenna (Hassan et al., 2017) using techniques similar to those performed within the WSR-88D network (Bringi and Chandrasekar, 2001; Ice et al., 2015).

3.2.3 Microphysical measurements

A suite of microphysical instruments, including optical array probes (OAPs) that were used to derive the PSDs and a Nevzorov probe that measured the IWC, were installed on the Citation aircraft for the field projects analyzed in this study. Specifics on the instrumentation and methodology used to process the data are provided below.

OAP data

A 2D cloud (2D-C) probe, a cloud imaging probe (CIP), and a High Volume Precipitation Spectrometer, version 3 (HVPS-3), were used during MC3E and GCPEx while a 2D stereo (2D-S) probe and an HVPS-3 were used during OLYMPEX to image particles. Table 3.1 outlines the OAPs used to create a composite PSD for each campaign, and the range of particle sizes considered for each probe. Although the CIP has a larger sample volume compared to the 2D-C, inclusion of anti-shattering tips on the 2D-C reduced the impact of shattered artifacts and therefore was the preferred instrument to size smaller particles during MC3E (Wu and McFarquhar, 2016). To maintain consistency in how particles were imaged as the Citation flew through cloud, all OAPs used in the field experiments were installed on the aircraft such that their arms were oriented vertically.

Morphological properties of individual particles (e.g., maximum dimension, habit, projected area, perimeter, and area ratio) were calculated and PSDs derived for each second of flight using the University of Illinois/Oklahoma OAP Processing Software (UIOOPS; McFarquhar et al., 2018b). Details regarding the OAPs, particle sizes, and criteria considered for the computation of PSDs for the MC3E project are provided in Chapter 2 while similar details related to the processing of particle properties during OLYMPEX are given in Chase et al. (2018). Information pertaining to the determination of PSDs for the GCPEx flights are described below.

A 1 mm cutoff between the 2D-S/2D-C/CIP and the HVPS-3 was chosen since the difference in the number distribution function N(D) between the 2D-S/2D-C/CIP and the HVPS-3 was a minimum in the $0.8 \leq D \leq 1.2$ mm size range for the events analyzed, and because it allowed particles to be mostly imaged by the 2D-S/2D-C/CIP while maintaining sufficient counting statistics in this size range. The sensitivity of composite PSDs for all coincident points was evaluated for a 1 and 1.2 mm cutoff between the 2D-S/2D-C/CIP and the HVPS-3. The mean ratio in the N(D) from 0.8–1.2 mm between these cutoff sizes are 1.26 for MC3E, 1.13 for GCPEx, and 0.76 for OLYMPEX. The mean ratio in the median mass diameter D_{mm} using the *m-D* relationship from Heymsfield et al. (2004, hereafter H04) are 0.91, 0.95, and 0.96, respectively.

Although anti-shattering tips were installed on the CIP during GCPEx and the 2D-S during OLYMPEX, previous

studies (Korolev et al., 2011, 2013a; Jackson et al., 2014) show that applying an algorithm removing shattered artifacts based on the frequency distribution of elapsed times between particles entering the OAP's sample volume (inter-arrival time; Baumgardner and Dye, 1983; Field et al., 2003) is also needed. A bimodal distribution in the inter-arrival times occurs when these artifacts are present and belong to a mode with shorter inter-arrival times, while the naturally-occurring particles have a mode with longer inter-arrival times (e.g., Field et al., 2006). During GCPEx (OLYMPEX) the distribution of inter-arrival times from the CIP (2D-S) was bimodal, with the division between the modes varying with time. Thus, for each group of 10^5 particles, an inter-arrival time threshold was determined based on the two modes present, with particles in the smallest mode of inter-arrival times identified as artifacts.

To examine the sensitivity of PSDs to the choice of threshold used to identify artifacts, alternate PSDs were derived using a constant inter-arrival time threshold determined for the entire flight. The mean ratio in the number concentration N_t (D_{mm}) for the different algorithms was 0.91 (1) during GCPEx and 1.03 (1) during OLYMPEX. Differences are larger for N_t than D_{mm} because smaller particles, which are more likely to be shattered artifacts, have more weight in determining N_t than D_{mm}. Given that the technique used to determine *m-D* coefficients (section 3.2.4) involves moments related to the mass and reflectivity, which are dominated by the larger particles, the differences between algorithms are less important. For the MC3E cases used in this study 99.8% of particles belonged to the larger mode of the frequency distribution of inter-arrival times, suggesting few particles were shattered artifacts (Wu and McFarquhar, 2016), and thus no shatter removal algorithm was applied to the CIP or the HVPS-3.

IWC data

IWC measurements were made by the Nevzorov probe for all 3 campaigns. Even with the deep cone used in these experiments, the IWC may be underestimated when particles with D greater than about 4 mm bounce out of the cone (Korolev et al., 2013b; Wang et al., 2015). Korolev et al. (2013b) found that the IWC measured by the Nevzorov probe disagreed on average by 2% compared to the IWC derived from PSDs when the maximum D was smaller than 4 mm and by 8% when the maximum D was larger than 4 mm. These uncertainties are considered in the development of equally plausible *m-D* coefficients and further discussed in the subsection below.

3.2.4 Deriving surfaces of equally plausible *m-D* coefficients

A method for deriving a surface of equally plausible solutions for *m-D* coefficients for varying environmental conditions is detailed in this subsection. The surfaces of coefficients are determined for multiple ranges of T and IWC spanning 19 flights from 3 field campaigns by minimizing the χ^2 differences between the IWC and Z directly measured by the Nevzorov probe and ground-based radar, respectively, and that derived from the N(D) following Chapter 2, who applied the technique to 3 cases during MC3E.

The minimization procedure in this study was applied to 2 ranges of environmental temperature (T < -20 and -20 $\leq T <$ -5 °C) and 3 ranges of IWC (0.05 $\leq$ IWC $<$ 0.2, 0.2 $\leq$ IWC $<$ 0.35, and IWC $\geq$ 0.35 g m^{-3}). The temperature categories are chosen based on Bailey and Hallett (2009) in an effort to represent ranges where single crystals (T > 20 °C) and polycrystals (T < 20 °C) typically grow, even if they are not necessarily observed at the temperatures where they grow. Distributions of T and IWC for the coincident points in each campaign are shown in Fig. 3.1, with the ranges of T and IWC separated by vertical lines. The sampling strategy performed and altitudes in which in-situ measurements were made during MC3E (section 3.3) resulted in a larger proportion of coincident points (68%) with T < -20 °C compared to GCPEx and OLYMPEX (Fig. 3.1a). The distribution of IWC measurements for the coincident points during MC3E was also different from GCPEx and OLYMPEX, with 55% of the coincident points having IWC values $\geq$ 0.35 g m^{-3}.

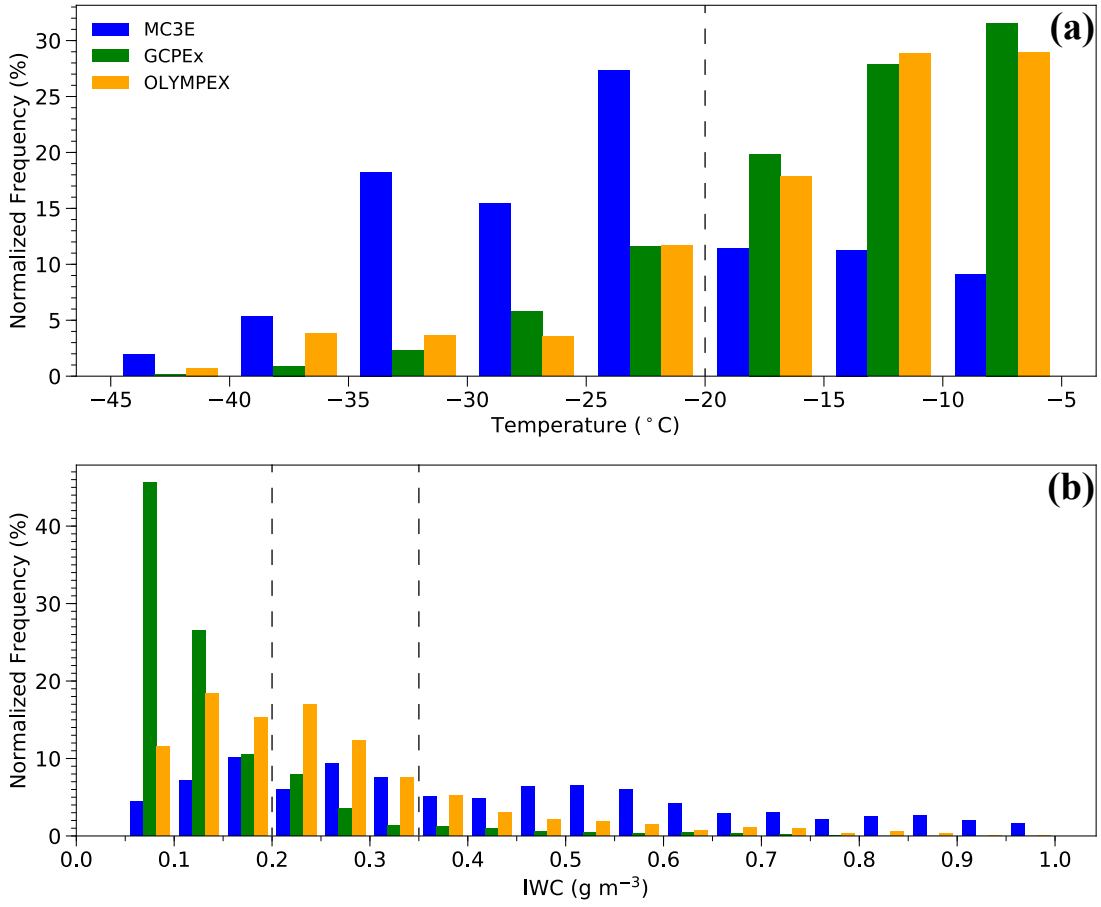

Figure 3.1: Normalized frequency of coincident points for (a) temperature T in 5 °C incriments and (b) ice water content (IWC) in 0.05 g m^{-3} incriments for MC3E (blue), GCPEx (green), and OLYMPEX (orange). Temperature and IWC values between the vertical lines correspond to ranges used for analysis (section 3.2.4).

The IWC and Z derived from the N(D) of a 10-s coincident point and using a particular a and b is given by IWC$_{SD}$

and Z_{SD}, respectively, and are computed following the methods of Hogan et al. (2006) and Chapter 2. The IWC_{SD} is a function of the concentration and individual particle mass for each size bin, whereas the Z_{SD} is proportional to the square of a particle's mass and dependent on the density of ice as well as the dielectric constants for ice ($|K_{ice}|^2$ = 0.17) and water ($|K_w|^2$ = 0.93). Following Chapter 2, the difference between the IWC and *Z* derived using a specific *a* and *b* from the N(D) and that measured directly by the Nevzorov probe and ground-based radar, respectively, is given by IWC_{diff} and Z_{diff} for all (*a,b*) combinations from a domain of values encompassing $5 \times 10^{-4} < a < 0.35$ g cm^{-b} at increments of 5×10^{-4} g cm^{-b} and $0.20 < b < 5.00$ at increments of 0.01. The minimization of the sum of IWC_{diff} + Z_{diff} at each (*a,b*) determines which *a* and *b* coefficient gives the best agreement between the measured moments IWC and *Z* and those derived from the N(D). Chapter 2 showed that the co-variability of *a* and *b* permit a swath of coefficients that minimize the difference between the measured and derived moments. The chi-square statistic (χ^2) for each *T* and IWC category involves a summation of $IWC_{diff} + Z_{diff}$ over all N 10-s coincident points meeting the *T* and IWC criteria, and normalized by N. The *a* and *b* that minimize χ^2, hereafter χ^2_{min}, is considered the most likely *a* and *b* value for that range of *T* or IWC.

An allowable tolerance $\Delta\chi^2$ that represents uncertainty in the derived coefficients for a given environment is also considered such that all *a* and *b* coefficients fulfilling $\chi^2 \leq \chi^2_{min} + \Delta\chi^2$ are regarded as equally plausible solutions. The confidence region, defined as $\Delta\chi^2 = \max(\chi^2_{min}, \Delta\chi^2_1, \Delta\chi^2_2)$, considers the robustness of the minimization procedure affected by the natural parameter variability (χ^2_{min}), uncertainties in the N(D) due to statistical sampling uncertainties ($\Delta\chi^2_1$), and instrument measurement uncertainties ($\Delta\chi^2_2$). The $\Delta\chi^2_1$ characterizes the difference between the IWC or *Z* estimated from the measured N(D) (IWC_{SD} or Z_{SD}) using the most likely (*a,b*) and from the minimum and maximum IWC/*Z* derived using the minimum and maximum N(D). The minimum and maximum N(D), obtained by subtracting or adding the square root of the number of particles counted in each size bin to the number of particles counted in the bin, follows McFarquhar et al. (2015) and uses Poisson statistics to quantify uncertainty in the actual particle counts for each size bin (Hallett, 2003; McFarquhar et al., 2007b). Measurement uncertainties in N(D) and bulk measurements of IWC and *Z* are considered in $\Delta\chi^2_2$. A 50% uncertainty in the measured N(D) (Heymsfield et al., 2013; Baumgardner et al., 2017), 2–8% uncertainty in the Nevzorov IWC measurements (section 3.2.3, Korolev et al., 2013b), and a 1 dB uncertainty in the radar reflectivity (Krajewski and Ciach, 2003) are used to compute $\Delta\chi^2_2$ for a given environment. Chapter 2 provides more details on and mathematical expressions for the various uncertainties used in the generation of the uncertainty surfaces in (*a,b*) phase space.

3.3 Events description

One of the overarching goals of the GPM GV field campaigns was to validate and improve the microwave and radar retrieval algorithms pertaining to the GPM constellation of satellites by making targeted measurements of cloud microphysical properties and precipitation characteristics from radar both in the air and at the ground (Petersen and Schwaller, 2008). A total of 6119 coincident observations over 19 flights from 3 GPM GV missions (section 3.2.1) are used here to characterize *m-D* relationships in clouds containing ice hydrometeors. An overview of each field project and instrument setup pertaining to this study is outlined below. Table 3.2 provides a brief synoptic description, the range in T and altitude, and the number of coincident points for each flight used in the analysis.

Table 3.2: Overview of the flights used in the analysis, including the synoptic context, number of 10-s coincident points, and temperature and altitude ranges considered.

Flight Date	# Obs.	Alt. Range (km)	T Range	Synoptic Context
			MC3E	
25 Apr 2011	395	5.0–8.3	-36.4– -10.6	Thunderstorms from upper-level trough evolving into an MCS.
18 May 2011	260	4.4–7.5	-24.7– -5.0	Elevated convection associated with a low level jet.
20 May 2011	390	4.8–7.9	-23.0– -5.1	Thunderstorms along dry line evolving into north-south oriented squall line.
23 May 2011	334	4.9–10.4	-42.9– -7.5	Discrete supercells along dry line transitioning into linear MCS feature.
			GCPEx	
19 Jan 2012	262	0.2–4.8	-35.5– -5.5	Broad area of precipitation ahead of cold front evolving into banded features.
28 Jan 2012	313	1.2–6.3	-41.0– -5.3	Broad area of snow associated with upper level disturbance.
30 Jan 2012	347	.02–4.4	-17.3– -5.4	Broad area of snow associated with upper level disturbance ahead of warm front.
12 Feb 2012	269	0.9–2.2	-21.5– -10.8	Northwest-southeast oriented lake-effect bands originating over Lake Huron.
18 Feb 2012*	471	0.3–4.3	-29.0– -5.0	1009-hPa center of low pressure traversing east over deployment region.

Table 3.2 (cont.)

24 Feb 2012*	327	0.9–5.8	-32.9– -5.0	985-hpa center of low pressure in Ohio Valley moving over Georgian Bay.
			OLYMPEX	
13 Nov 2015	49	3.2–6.8	-28.4– -5.0	Heavy warm sector precipitation ahead of narrow cold frontal band.
01 Dec 2015	410	3.0–7.0	-29.5– -5.0	Stratiform precipitation associated with warm-frontal passage.
03 Dec 2015	419	3.0–6.0	-23.3– -5.0	Warm sector precipitation ahead of stalled cold front.[a]
05 Dec 2015	638	2.9–9.1	-49.3– -5.0	Broad area of precipitation associated with cold front in sheared environment.
12 Dec 2015	613	2.1–6.0	-23.0– -5.2	Warm sector precipitation and passage of occluded front.
18 Dec 2015*	622	2.6–10.2	-57.5– -5.1	Widespread precipitation with embedded convection during occlusion.

*Denotes two flights were flown on that day.

[a]Surface analysis and thermodynamic profiles provided in Purnell et al. (2018).

MC3E used coordinated airborne and ground instruments to improve the understanding of the physical drivers associated with convective clouds in the mid-latitudes (Jensen et al., 2016). The Citation aircraft housed a suite of cloud microphysical instruments that measured cloud particle properties, while data from the KVNX radar was used to characterize the radar Z at the aircraft's location (section 3.2). Jensen et al. (2014) give an overview of the synoptic conditions for several mesoscale convective systems (MCSs) while Chapter 2 details the microphysical characteristics and *m-D* relationships for three of the MC3E events analyzed in this study.

During GCPEx, aircraft and ground-based measurements of the radiative and microphysical properties of falling snow were made in Ontario, Canada (Skofronick-Jackson et al., 2015). The Citation aircraft conducted Lagrangian spiral ascents and Lagrangian and Eulerian descents in addition to constant-altitude legs. The CWKR radar routinely conducted plan-position indicator (PPI) scans and on occasion performed range-height indicator (RHI) scans along the same radial as the constant-altitude legs flown by the Citation aircraft.

A major goal of OLYMPEX was to improve understanding of the orographic influence on frontal precipitation processes in the Pacific Northwest (Houze et al., 2017). While aspects of the OLYMPEX multiplatform sampling strategy were similar to other GPM GV campaigns in its collection of microphysical and radiative properties through

the depth of the troposphere, emphasis was placed on data collection upwind of, over, and downwind of mountainous terrain. The Citation aircraft frequently flew near-constant altitude flight legs at various depths in cloud to provide a vertical profile of ice particle sizes, derived concentrations, and other morphological properties within range of volume scans performed by the KLGX radar. Given that nearly all in situ measurements from the Citation aircraft were made on the windward side of the Olympic Range (Houze et al., 2017), this study does not address the role that terrain may have in affecting the *m-D* relations on the leeward side of the mountains.

3.4 Microphysical summary

In order for the *m-D* surfaces to be placed in context of the microphysical conditions for a particular environment, the mean N(D) and cumulative mass distribution function M(D) for each range of T and IWC (section 3.2.4) is provided in Fig. 3.2. The cumulative M(D) is estimated using the H04 m-D relation. While this relation does not consider the impact of particle density for different habits, it is useful for comparing among the different environments. For increasing T and IWC, a notable increase in the cumulative M(D) (Figs. 3.2d–f) is generally associated with a greater concentration of larger particles (Figs. 3.2a–c) observed in warmer regions of cloud containing greater mass contents.

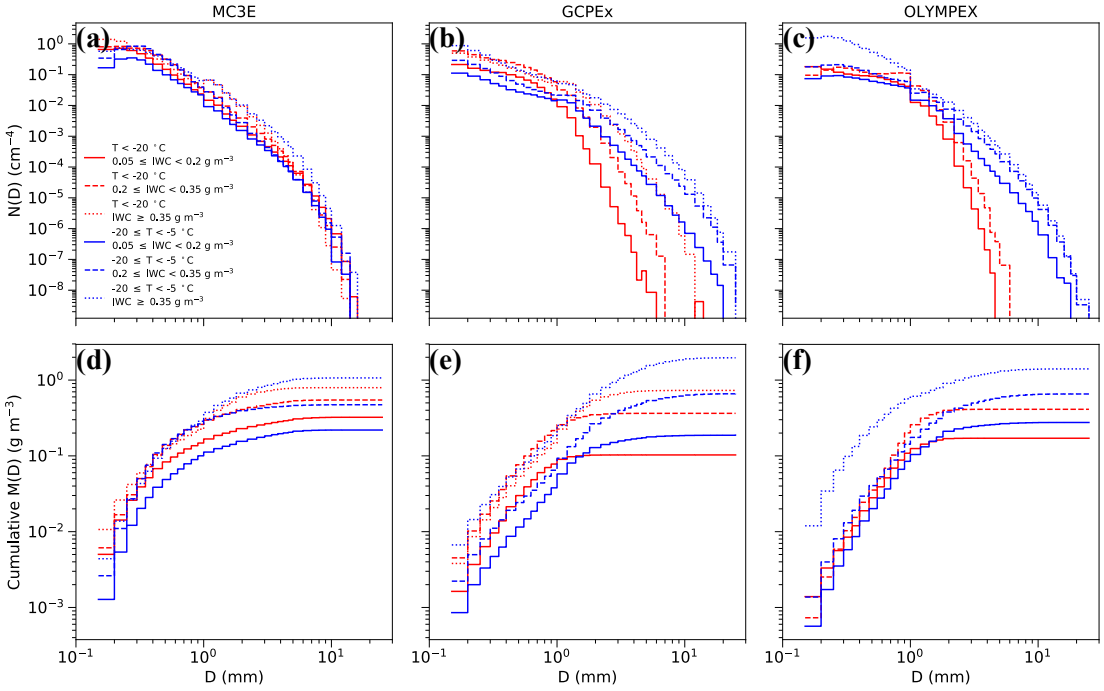

Figure 3.2: Mean (a–c) N(D) and (d–f) cumulative M(D) for (a,d) MC3E, (b,e) GCPEx, and (c,f) OLYMPEX. Line colors correspond to different ranges of T and line styles to IWC.

While differences in the N(D) and cumulative M(D) exist for different environments during MC3E, the slopes of the PSDs are similar (Fig. 3.2a). Wang et al. (2015) found that the median slope parameter from 6 MC3E flights where

the Z derived from fitted PSDs $>$ 12 dBZ, which consist of 86% of the MC3E observations in this study, only ranged between 5 and 15 cm^{-1}. Similarities in the slope of the PSD yield an M(D) integrated over the range of particle sizes (i.e., estimated IWC) that's similar irrespective of temperature. When the integrated M(D) for $T <$ -20 and $T \geq$ -20 °C are compared for similar IWC (Fig. 3.2d), their ratios are 1.45 for 0.05 $\leq$ IWC $<$ 0.2 g m^{-3}, 1.17 for 0.2 $\leq$ IWC $<$ 0.35 g m^{-3}, and 0.74 for IWC $\geq$ 0.35 g m^{-3}. The N(D) during MC3E for $T <$ -20 °C and IWC $<$ 0.35 g m^{-3} differed significantly from the other campaigns, with greater number concentrations observed for particles larger than 1 mm and the N(D) was 2–3 orders of magnitude greater for $D \geq$ 4 mm (Figs. 3.3a,b).

Unlike the conditions sampled during MC3E, the slope of the PSD is more sensitive to the different environments analyzed for GCPEx and OLYMPEX (Figs. 3.2b,c). Environments where -20 $\leq T \leq$ -5 °C have a broader PSD compared to MC3E with particles as large as 25 mm observed (Figs. 3.3d–f). During GCPEx and OLYMPEX the N(D) at 15 mm, where the largest particles were observed for MC3E, ranged from 1 to 3 orders of magnitude greater, suggesting that a more efficient aggregation process occurred in warmer regions of the cloud. When $T <$ -20 °C, particles larger than 10 mm were not observed during OLYMPEX and were rarely observed during GCPEx (Figs. 3.3a–c). Given differences in the PSD slope measured for these experiments, larger spread occurs in the integrated M(D) (Figs. 3.2e,f) compared to the differences observed in the integrated M(D) during MC3E.

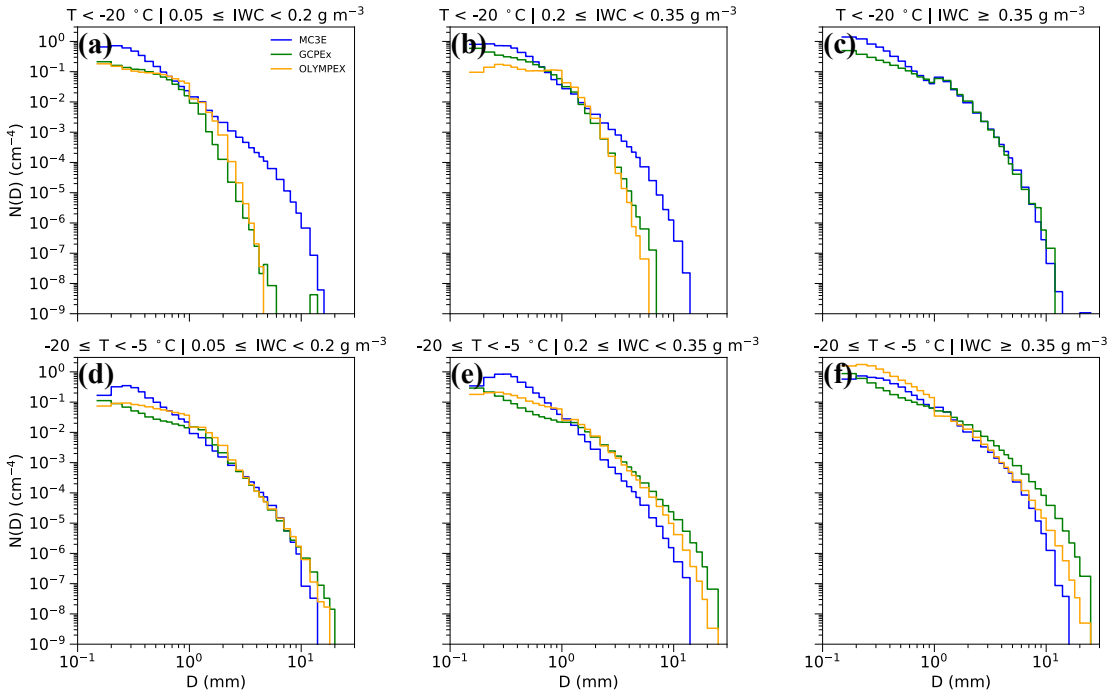

Figure 3.3: Same as in Figs. 3.2a–c, but divided by T (rows) and IWC (columns) for MC3E (blue), GCPEx (green), OLYMPEX (orange).

The N(D) and cumulative M(D) for -20 $\leq T \leq$ -5 °C and IWC $\geq$ 0.35 g m^{-3} are notably greater in the 0.15–1 mm

size range during OLYMPEX compared to the other environments. Particle images from the 2D-S were examined for instances when $N_t > 100$ L^{-1}, and representative particles from 4 periods are shown in Fig. 3.4. The presence of an abundant number of columns and needles in conjunction with a few SLW drops observed in the -10 to -5 °C range suggests that secondary ice production via the Hallet-Mossop process may be active during these periods.

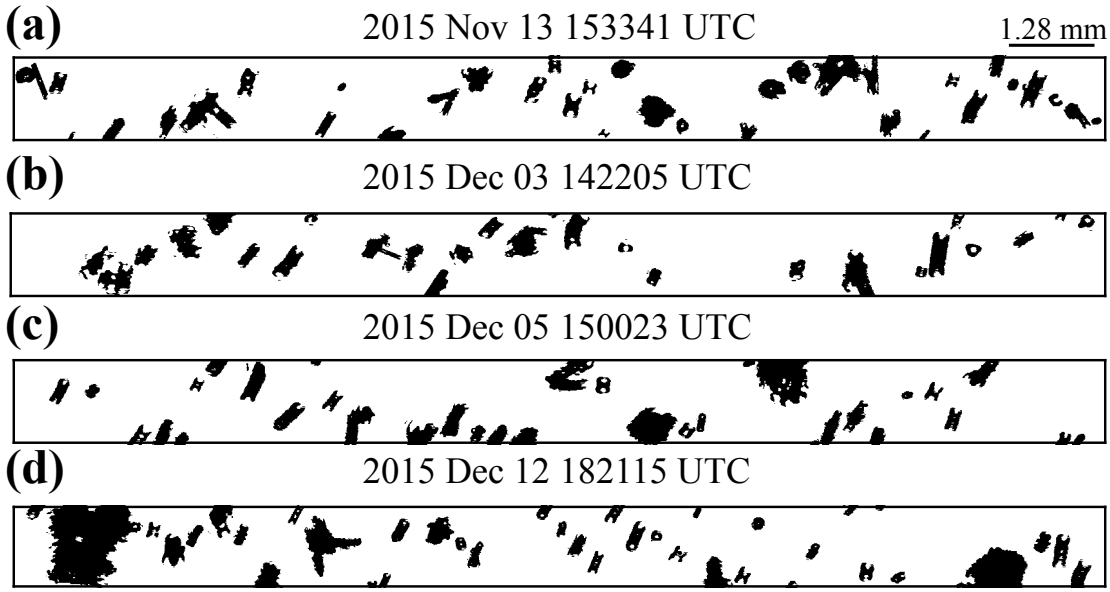

Figure 3.4: Representative particle images from the 2D-S probe during 4 OLYMPEX periods when -10 $\leq T <$ -5 °C and secondary ice production is believed to be active. The image buffer size (panel height) is 1.28 mm and shown as a scale in the top right.

Distributions of the radar Z, number concentration N_t, and median mass diameter D_{mm} are represented as box-and-whisker plots in Fig. 3.5. The H04 *m-D* relation is used to estimate D_{mm}. The box edges denote the 25th and 75th percentiles from coincident observations for each range of T and IWC, the whiskers represent the 5th and 95th percentiles, and the line in the middle is the median.

A greater or smaller radar Z is typically correlated with a greater or smaller IWC, and distributions of the radar Z are skewed towards larger values when -20 $\leq T \leq$ -5 °C compared to environments with similar IWC at colder temperatures (Figs. 2a,b). The median N_t within a given temperature range generally increases with increasing IWC for each campaign, while distributions of N_t when -20 $\leq T \leq$ -5 °C are generally skewed towards smaller values compared to environments with similar IWC at colder temperatures during GCPEx and OLYMPEX (Figs. 3.5c,d). Given that the particles sampled deeper within the cloud occur at warmer temperatures, deposition and aggregation growth processes occurring in these regions of cloud for GCPEx and OLYMPEX may explain why the N_t is on average lower (Fig. 3.5d), the D_{mm} larger (Fig. 3.5f), and the PSDs more broad (Figs. 3.2b,c) than the colder environments.

Given that variability within an environment of similar T and IWC can influence the $\Delta\chi^2$ (section 3.2.4), the spread in the distributions of Z (Figs. 2a,b) and in the PSDs as represented by N_t (Figs. 2c,d) and D_{mm} (Figs. 2e,f) are

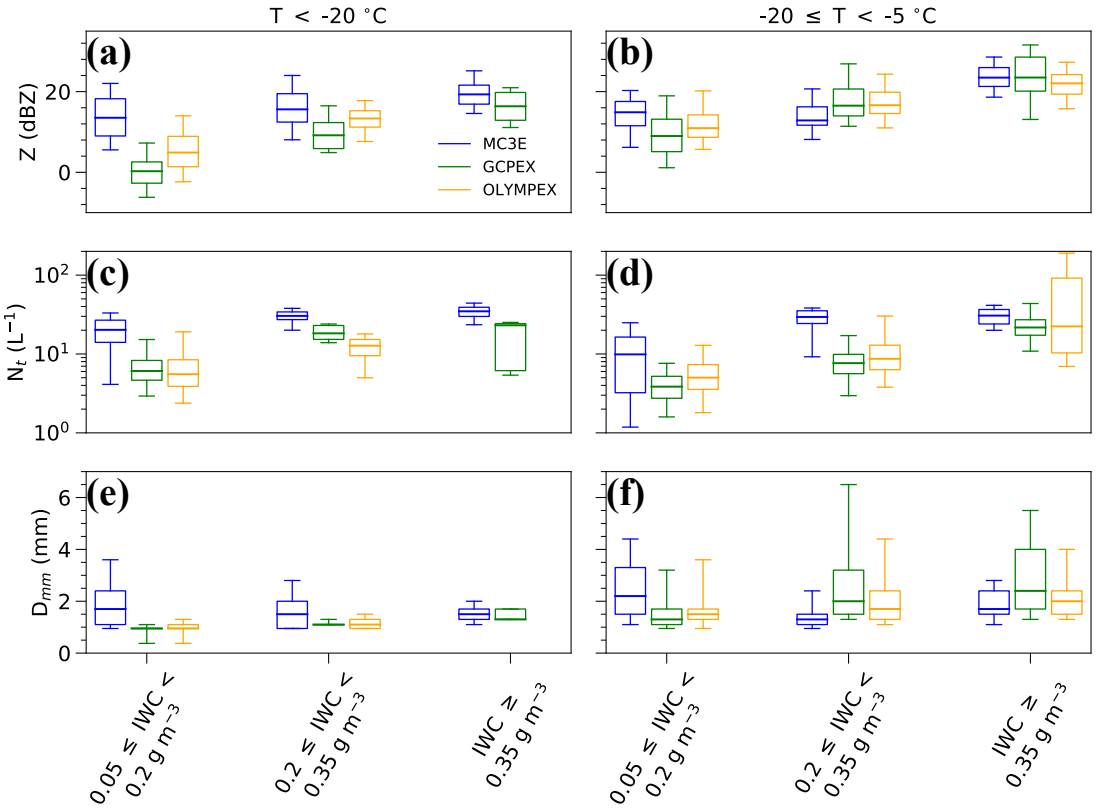

Figure 3.5: Distribution of (a,b) radar Z, (c,d) number concentration N_t, and (e,f) median mass diameter D_{mm} for each range of T (column) and IWC. Box edges represent the 25th and 75th percentiles, whiskers are the 5th and 95th percentiles, and the line in the middle is the median.

important factors in explaining differences in the size of the *m-D* surfaces as further discussed in section 3.5.

In an effort to characterize the shape and density of an ensemble of particles, the sphericity and effective density were computed for each coincident point, and their distributions provided for each range of T and IWC in Fig. 3.6. The sphericity of a particle projected on a 2D plane is defined as the ratio of the cross-sectional area measured by an OAP to the number of shadowed pixels along its edge multiplied by the diode resolution (McFarquhar et al., 2005; Finlon et al., 2016, 2019). A mass-weighted mean of sphericity is then computed from particles sampled for each coincident point using the HY04 *m-D* relation (Figs. 3.6a,b). Effective density ρ_e (Figs. 3.6c,d) is defined following Chase et al. (2018) and Chapter 2 as the ratio of IWC (derived using the HY04 relation) to the integrated of volume of particles with an assumed particle aspect ratio of 0.6 (Hogan et al., 2012). A Mann-Whitney U test confirms that sphericity and effective density values between the higher and lower temperature environments are statistically different at the 99% confidence level, with higher sphericity and ρ_e for $T <$ -20 °C suggesting that particles are on average more compact and dense than at higher temperatures.

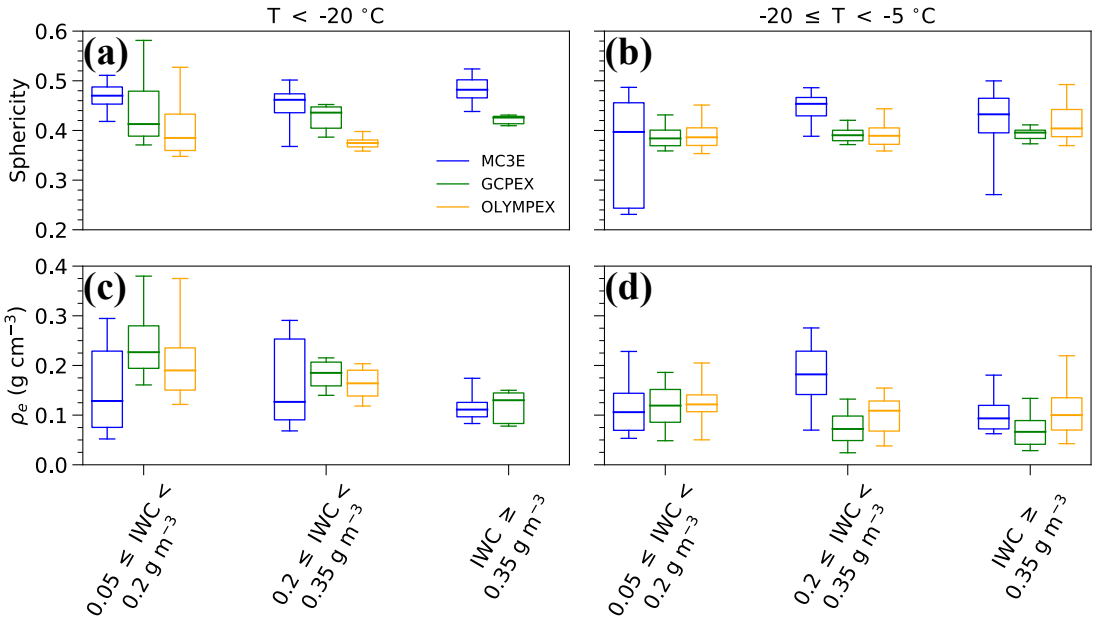

Figure 3.6: Same as in Fig. 3.5, but for mass-weighted mean sphericity (top) and effective density ρ_e (bottom).

3.5 Environmental dependence on *m-D* relationships

The set of equally plausible *m-D* coefficents for all ranges of T and IWC, represented as a surface in (*a,b*) phase space, is shown for MC3E, GCPEx, and OLYMPEX in Fig. 3.7. For each range in temperature (column), the surfaces colored red are comprised of coincident points where $0.05 \leq \text{IWC} < 0.2$ g m^{-3}, blue where $0.2 \leq \text{IWC} < 0.35$ g m^{-3}, and magenta where IWC ≥ 0.35 g m^{-3}. The dot, triangle, and square correspond to the a (a_{min}) and b (b_{min}) from the same surfaces where χ^2 is minimized, and is quantitatively shown in Table 3.3. The extent of each surface beyond the minimum χ^2 is represented as $\Delta\chi^2$ and the area of each surface is determined by the χ^2 values at each a and b in the (*a,b*) domain and the $\Delta\chi^2$ computed for each environment.

To quantify the similarity between two surfaces of equally plausible *m-D* coefficients (hereafter *m-D* surfaces), the Jaccard similarity coefficient J is computed. The coefficient J, defined as

$$J = \frac{X_1 \cap X_2}{X_1 \cup X_2}, \tag{3.1}$$

involves comparison of the number of equally plausible solutions in common between both *m-D* surfaces ($X_1 \cap X_2$) to the total number of equally plausible solutions from either surface ($X_1 \cup X_2$). Put another way, the number of (*a,b*) pairs considered equally plausible for both *m-D* surfaces (Y_{11}) are compared against the number of (*a,b*) pairs

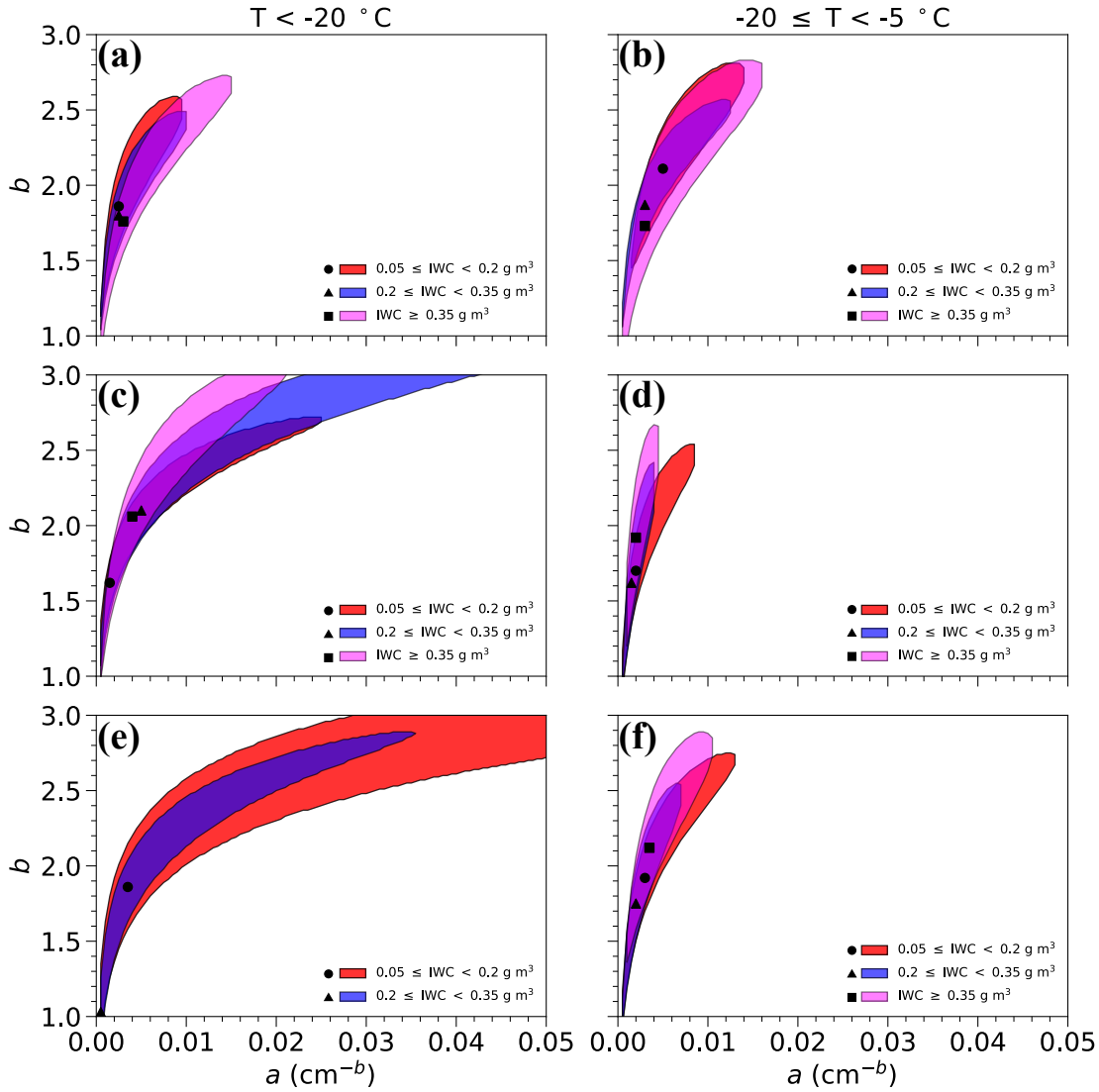

Figure 3.7: Set of equally plausible a and b coefficients for (a,c,e) $T <$ -20 and (b,d,f) -20 $\leq T <$ -5 °C and colored for IWC ranges of 0.05 $\leq$ IWC $<$ 0.2 g m^{-3} in red, 0.2 $\leq$ IWC $<$ 0.35 g m^{-3} in blue, and IWC $\geq$ 0.35 g m^{-3} in magenta for (a,b) MC3E, (c,d) GCPEx, and (e,f) OLYMPEX. The dot, triangle, and square correspond to the a and b from the same surfaces where χ^2 is minimized.

considered equally plausible for one surface and not the other (Y_{10}) and vice versa (Y_{01}) such that

$$J = \frac{Y_{11}}{Y_{11} + Y_{10} + Y_{01}}. \tag{3.2}$$

Values closer to 1 indicate greater similarity between two surfaces.

The J computed for all combinations of surfaces in the different T and IWC ranges for each campaign are shown as a percent in Fig. 3.8. Each box within the grid represents the degree of similarity between an *m-D* surface for the T and IWC listed for that row and for a surface fitting the T and IWC criteria for that column. Each label contains

a Roman numeral following the range of T to indicate an IWC range of 0.05–0.2 g m^{-3} (I), 0.2–0.35 g m^{-3} (II), and $\geq$ 0.35 g m^{-3} (III). The boxes are greyed out along the diagonal as the *m-D* surfaces for the environment in the corresponding row and column are identical and if one or both environments being compared did not contain coincident points to analyze the a and b coefficients. Boxes closer to the diagonal signify *m-D* surfaces that are being compared in environments where the differences between T and IWC are not as great, while the box in the lower left of each panel compares a surface with substantially greater T and IWC in the last row to a surface with lower T and IWC in the first column.

Table 3.3: The a (a_{min}) and b (b_{min}) that minimize χ^2 for each range of T and IWC that correspond to the *m-D* surfaces shown in Fig. 3.7.

T	$T <$ -20 °C			-20 $\leq T <$ -5 °C		
IWC	0.05 $\leq$ IWC $<$ 0.2 g m^{-3}	0.2 $\leq$ IWC $<$ 0.35 g m^{-3}	IWC $\geq$ 0.35 g m^{-3}	0.05 $\leq$ IWC $<$ 0.2 g m^{-3}	0.2 $\leq$ IWC $<$ 0.35 g m^{-3}	IWC $\geq$ 0.35 g m^{-3}
			MC3E			
a_{min}	0.0025	0.0025	0.003	0.005	0.003	0.003
b_{min}	1.86	1.8	1.76	2.11	1.87	1.73
$\chi^2{}_{\text{min}}$	0.69	0.55	0.432	0.454	0.343	0.893
			GCPEx			
a_{min}	0.0015	0.005	0.004	0.002	0.0015	0.002
b_{min}	1.62	2.1	2.06	1.7	1.62	1.92
$\chi^2{}_{\text{min}}$	0.224	0.263	0.07	0.254	0.27	0.554
			OLYMPEX			
a_{min}	0.0035	0.0005	–	0.003	0.002	0.0035
b_{min}	1.86	1.03	–	1.92	1.75	2.12
$\chi^2{}_{\text{min}}$	1.407	0.893	–	0.257	0.408	0.563

3.5.1 MC3E

The *m-D* surfaces for MC3E are considered to be similar in size and shape within the (*a,b*) phase space for the different T and IWC environments (Figs. 3.7a,b). Figure 3.8a illustrates this similarity as 80% of the comparisons between *m-D* surfaces are at least 40% similar in terms of area, shape, and placement within the (*a,b*) phase space. The b minimizing χ^2, particularly for the $T <$ -20 °C environment, is also similar with the b that minimizes χ^2 ranging in value from 1.76–1.86 (Table 3.3). Comparing the range of a and b considered as equally plausible for IWC $\geq$ 0.35 g m^{-3} for both ranges of T, which correspond to the largest *m-D* surfaces for each temperature range, yield similarities as well.

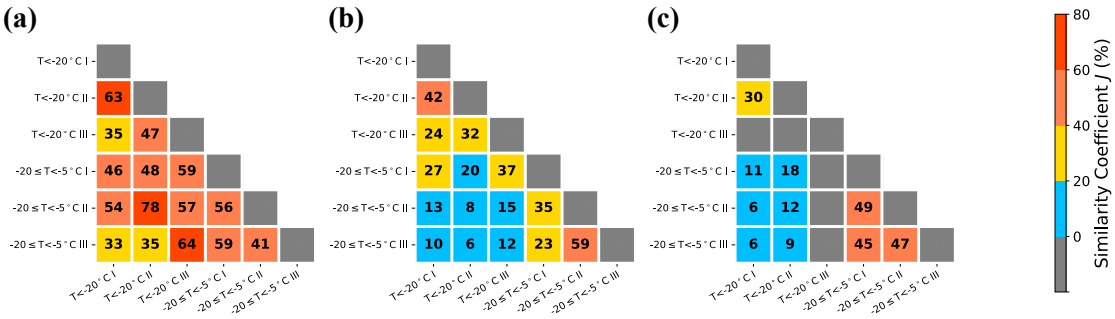

Figure 3.8: Jaccard similarity coefficient J (%) between 2 *m-D* surfaces corresponding to the ranges of T and IWC given for each row and column during (a) MC3E, (b) GCPEx, and (c) OLYMPEX. Roman numerals indicate an IWC range of 0.05–0.2 g m^{-3} (I), 0.2–0.35 g m^{-3} (II), and $\geq$ 0.35 g m^{-3} (III).

The largest value of a (b) within the IWC $\geq$ 0.35 g m^{-3} surface for $T <$ -20 °C is 0.015 g cm^{-b} (2.73) compared to 0.016 g cm^{-b} (2.83) for similar IWC when -20 $\leq T <$ -5 °C.

Similarities in the *m-D* surfaces for MC3E are placed into the context of the type of cloud sampled, where measurements were made, the vertical velocities that occurred, and microphysical properties observed during the field experiment. Aircraft measurements were typically taken in the anvil cirrus region like in the 23 May event or in the stratiform outflow region of the MCS as in the 20 May squall line case (Table 3.2; Fridlind et al., 2017). Chapter 2 corroborated the findings of Heymsfield et al. (2007) that observed little temperature dependence on the a coefficient for measurements made in anvil cirrus clouds. The maximum vertical velocity w measured by the aircraft for each coincident point was obtained and distributions made for each campaign as shown in Fig. 3.9. The distributions are binned in increments of 0.5 m s^{-1} and normalized such that integration across all bins equals 1. The distribution median, standard deviation σ, and skewness are also provided in each panel. A broader distribution that is skewed towards larger w during MC3E suggests that the aircraft more frequently sampled regions of cloud that were greater affected by vertical motions compared to GCPEx (Fig. 3.9b) and OLYMPEX (Fig. 3.9c).

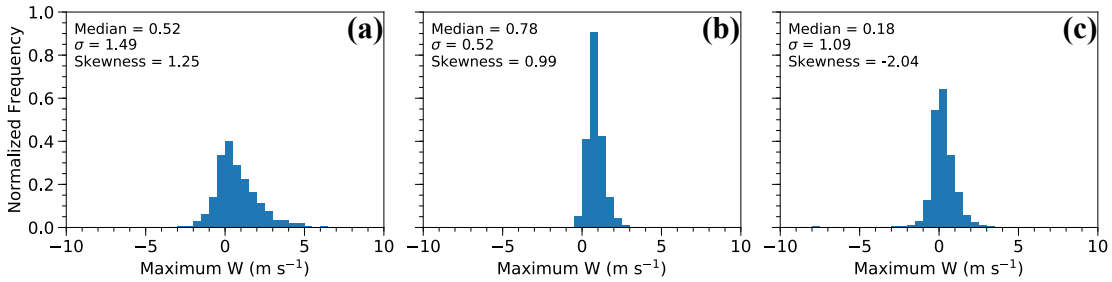

Figure 3.9: Distribution of the maximum vertical velocity w from coincident points for (a) MC3E, (b) GCPEx, and (c) OLYMPEX. Bins are in incriments of 0.5 m s^{-1}.

One hypothesis that may explain why the mean N(D) did not consist of as many particles as large as those observed during GCPEx and OLYMPEX (Figs. 3.3d–f) is provided below. If graupel represented a larger fractional mass

contribution for the environments analyzed in MC3E compared to those in GCPEx and OLYMPEX as formed through the larger vertical motions observed, concentrations of larger aggregates could have been limited. Further, Fridlind et al. (2017) also mention differential sedimentation as a possible explanation for why signals of aggregation and dendritic growth between -20 $\leq T \leq$ -10 °C were not present for the 20 May MCS despite an increasing trend in the radar Z towards the melting level, a trend in Z that is also observed in Finlon et al. (2019). While modeling analysis may provide additional physical insight into the similarities in the PSDs shown in Fig. 3.2a, such efforts are beyond the scope of this study.

3.5.2 GCPEx

The *m-D* surfaces for GCPEx (Figs. 3.7c,d) are characterized by greater differences between temperature environments and also for ice mass content ranges within the same temperature range. The sensitivity of T and IWC to these surfaces is shown in Fig. 3.8b with 87% of the comparisons between *m-D* surfaces having a similarity $<$ 40%. While differences in the surfaces are greatest between the different ranges of T, where similarities range between 6 and 37% among the different combinations, the bulk ice mass content also influences the set of a and b coefficients considered as equally plausible.

A much larger range of a and b is observed for environments where $T <$ -20 °C, with values of a as large as 4.25 $\times$ 10^{-2} g cm^{-b} and b of 3 (Fig. 3.7c). Larger ranges in a and b are typically found to be correlated with less variability of cloud conditions (Chapter 2). When the domain of $IWC_{\text{diff}} + Z_{\text{diff}}$ values are considered for a coincident point, a narrow swath of a and b span the (a,b) domain given the co-variability of the a and b satisfying the *m-D* power law relationship. For conditions where the microphysical properties are not as variable (Fig. 3.5), a similar swath of a and b values may contain small $IWC_{\text{diff}} + Z_{\text{diff}}$ values for several coincident points such that the χ^2 integrated over all coincident points for an environment of similar T and IWC yield a large range of a and b where the $\chi^2 \leq \chi^2_{\text{min}} + \Delta\chi^2$ condition is satisfied.

To quantify the variability in Z, N_{t}, and D_{mm} between the $T <$ -20 and -20 $\leq T <$ -5 °C environments, the interquartile range IQR, defined as the difference between the 25$^{\text{th}}$ and 75$^{\text{th}}$ percentiles for a given variable, is used. For the cases analyzed during GCPEx the mean IQR among the three IWC environments for T colder (warmer) than -20 °C is 30.0 (241.15 mm^6 m^{-3}) for Z, 9.79 (5.54 L^{-1}) for N_{t}, and 0.13 (1.53) for D_{mm}. Smaller IQR values for the $T <$ -20 °C environments, particularly for Z and D_{mm}, indicate that the cloud properties are far less variable compared to warmer regions of cloud.

A highly variable aggregation process for the -20 $\leq T <$ -5 °C environments appeared to impact the variability of the microphysical properties observed. Coincident points where large aggregates were present yielded large D_{mm}, as with the 0.2 $\leq$ IWC $<$ 0.35 g m^{-3} environment, where D_{mm} at the 95$^{\text{th}}$ percentile was 6.5 mm. Conversely, D_{mm}

values for half of the coincident points for the same range of T and IWC were below 2 mm, highlighting the variability in the characteristic particle size within warmer regions of cloud for the events analyzed.

3.5.3 OLYMPEX

Similar to GCPEx, a greater range of a and b are considered equally plausible solutions for environments where T $<$ -20 °C (Fig. 3.7e) compared to warmer regions of cloud (Fig. 3.7f). This trend is also related to the variability of microphysical properties for each range of T and IWC, with a mean IQR among the IWC environments for T colder (warmer) than -20 °C of 13.39 (88.44 mm^6 m^{-3}) for Z, 5.16 (45.88 L^{-1}) for N_t, and 0.25 (0.8) for D_{mm}.

While all a and b coefficients associated with the *m-D* surface for T $<$ -20 °C and 0.05 $\leq$ IWC $<$ 0.2 g m^{-3} are shared with the surface corresponding to greater IWC values for the same range in T (Fig. 3.7e), the greater range in a and b for the latter *m-D* surface yields a similarity of 30% between the surfaces (Fig. 3.8c). Differences between these surfaces can be explained by the variability of microphysical properties. For conditions where 0.05 $\leq$ IWC $<$ 0.2 g m^{-3}, larger microphysical variability results from an IQR that is 217% greater for Z, 26% greater for N_t, and 133% greater for D_{mm}.

The *m-D* surfaces for the -20 $\leq$ T $<$ -5 °C environments are less sensitive to the value of IWC, with similarities ranging between 45 and 49% among the combinations considered (Fig. 3.8c). While some observations pertaining to IWC values $\geq$ 0.35 g m^{-3} were likely influenced by secondary ice production processes (section 3.4; Figs. 3.2, 3.5), the resulting *m-D* surface is still somewhat similar to the other surfaces for similar T. Since the larger N_t values primarily result from ice hydrometeors in the sub-millimeter size range, which contribute less to the bulk mass and reflectivity compared to the larger particles in a PSD, their impact on the χ^2 minimization procedure is less than the impact from larger particles that contribute more to the mass and reflectivity.

3.6 Conclusions

This chapter presents analyses of the variability in mass-dimension (*m-D*) relationships characterizing particle size distributions (PSDs) for different ranges of temperature T and ice water content IWC during the Mid-latitude Continental Convective Clouds Experiment (MC3E), Global Precipitation Measurement (GPM) Cold Precipitation Experiment (GCPEx), and Olympic Mountains Experiment (OLYMPEX). The study applies the technique outlined in Chapter 2 for deriving a surface of equally realizable solutions in the phase space of a and b parameters from an *m-D* relation, and extends the approach of McFarquhar et al. (2015) who derived a volume of equally realizable solutions in the phase space of gamma fit parameters corresponding to PSDs. Measurements of reflectivity Z from ground-based radar were matched to the location of the Cessna Citation II aircraft, where IWC measurements from the Nevzorov probe

were made and PSDs derived from optical array probe data. A χ^2 minimization technique was used on the coincident data to determine the set of equally plausible *a* and *b* coefficients for environments of similar *T* and IWC from which the χ^2 values were within a tolerance $\Delta\chi^2$, which considered natural variability in cloud conditions and uncertainties in the measurements, of the minimum χ^2.

The key findings of the paper are as follows:

1. The range of *a* and *b* coefficients contained within a surface of equally plausible solutions (i.e., the *m-D* surface) is related to the degree of variability in the cloud properties represented by *Z*, number concentration N_t, and median-mass diameter D_{mm}. Environments where the variability in cloud properties is less, such as environments where $T <$ -20 °C for GCPEx, have interquartile ranges that are a factor of 6.6 smaller for *Z*, 8.9 smaller for N_t, and 3.2 smaller for D_{mm} compared to environments where -20 $\leq T <$ -5 °C. Trends in the *m-D* surfaces are linked to the co-variability between *a* and *b* and corroborates the findings presented in chapter 2.

2. Notable differences were found in the N(D), N_t, D_{mm}, and *Z* between environments where the temperature was greater than or less than -20 °C for GCPEx and OLYMPEX. Environments where -20 $\leq T <$ -5 °C were characterized by PSDs with the largest particles around or greater than 2 cm, larger D_{mm}, and larger *Z* compared to environments colder than -20 °C. These properties, in conjunction with particle images, suggest a more active aggregation process was occurring within warmer regions of cloud for the systems analyzed.

3. For the MC3E storm environments analyzed in this study, the distribution of particle sizes was less sensitive to the temperature compared to GCPEx and OLYMPEX. The largest particles observed were smaller than during GCPEx and OLYMPEX, suggesting a less efficient aggregation process that might have been attributed to the presence of more graupel and rimed particles compared to habits whose growth was aided by aggregation. The larger updrafts observed during MC3E is consistent with this hypothesis. Similarities in the *m-D* surfaces also corroborate the findings in chapter 2 and Heymsfield et al. (2007) for measurements made in anvil cirrus clouds that observed little temperature dependence on the *a* coefficient.

4. The influence of IWC on the *m-D* surfaces is less than the influence of *T*. These trends are related to trends in the *Z*, N_t, and D_{mm} as the distributions among different ranges of IWC are more similar than the distributions among different ranges of *T*. The greater impact that *T* has on these surfaces may be related to the different types of crystals generally grown in $T <$ -20 °C environment (polycrystals) compared to the -20 $\leq T <$ -5 °C environment (single crystals) based on previous laboratory studies and *in situ* measurements (e.g., Hallett and Mossop, 1974; Field et al., 2016).

A key finding of this study is that the natural variability in cloud properties and various measurement uncertainties permit a range of *a* and *b* coefficients to be considered equally plausible for an environment of given *T* and IWC. The

range in a and b coefficients for an *m-D* surface indicates that that a similar Z and IWC can be obtained irrespective of the a and b values chosen. Further, random selection from these surfaces allows for the impact of any derived quantity using the uncertainty in (a,b) to be determined. As such, large variation in the set of equally plausible (a,b) as in the $T <$ -20 °C environments for GCPEx and OLYMPEX does not guarantee that quantities derived from these a and b coefficients will be characterized by a large uncertainty.

While this study incorporates 17 hours of flight data spanning 19 flights from numerous types of mesoscale and synoptic precipitation, caution should be exercised if extrapolating the results presented here to particle sizes or environments beyond what was sampled in the analysis. Given the different microphysical processes occurring for various environments and the resulting distribution of particle sizes, shapes, habits, and other characteristics, the types of environments sampled for a given campaign may yield *m-D* surfaces that are dramatically different than another environment. Future work applying the technique provided in Chapter 2 and expanded upon here to other cloud and meteorological environments may give insight into how these *m-D* surfaces are affected by the microphysical properties observed and the relevant processes occurring for various cloud or environmental properties. Further, relating the *m-D* surfaces to cloud dynamics and types of cloud systems (e.g., convective versus stratiform environments) is needed if the surfaces are to be applied in a useful manner to model simulations and retrievals for environments other than those from which they were derived.

Chapter 4

Analysis of an atmospheric river over Australia and the Southern Ocean: Microphysical evolution of the seeder-feeder process

This chapter examines the precipitation structure and microphysical properties observed during two transects through an atmospheric river during the Southern Ocean Clouds, Radiation, Aerosol Transport Experimental Study. This chapter will be submitted to the *Journal of Geophysical Research*.

4.1 Introduction

The pre-cold-frontal region within the warm sector of extratropical cyclones is associated with narrow zones of enhanced horizontal poleward transport of water vapor (Browning and Pardoe, 1973; Ralph et al., 2004). These elongated corridors of moisture, referenced to as atmospheric rivers (ARs; Zhu and Newell, 1998), are typically thousands of kilometers long and hundreds of kilometers wide with the greatest water vapor flux in the lowest 3 km of the troposphere (Ralph et al., 2018). These events, characterized by values of vertically-integrated water vapor $\geq$ 2 cm (e.g., Ralph et al., 2004; Neiman et al., 2008b; Dettinger et al., 2011) or integrated vapor transport $\geq$ 250 kg m^{-1} s^{-1} (Rutz et al., 2014), have considerable hydrological impact around the world (Ralph et al., 2006; Ruby Leung and Qian, 2009; Moore et al., 2012; Lavers and Villarini, 2013; Nakamura et al., 2013; Waliser and Guan, 2017).

The majority of field experiments related to ARs have focused on the Northeast Pacific since the frequency of land-falling extratropical cyclones, combined with orographic enhancement, make these high-impact events. The use of satellite microwave imagers (Ralph et al., 2006; Wick et al., 2013) permit identification of ARs and their key meteorological characteristics, while radio occultation techniques (Neiman et al., 2008a; Ma et al., 2011) have been used to retrieve temperature and moisture properties through the vertical column within these enhanced moisture plumes. The California Land-Falling Jets Experiment (CALJET), Pacific Land-Falling Jets Experiment (PACJET), and California Water Service (CalWater) field campaigns directly measured thermodynamic and kinematic properties via dropsonde deployments, identifying the melting level, low-level jet, and other unique thermodynamic and kinematic features associated with AR events (e.g., Ralph et al., 2005, 2017; Neiman et al., 2016).

A series of studies in recent years used spaceborne (Matrosov, 2012, 2013; Cannon et al., 2017) and ground-based

vertically-pointing radars (White et al., 2015; Kingsmill et al., 2016; Matrosov et al., 2016; Neiman et al., 2017) to evaluate cloud and precipitation characteristics within ARs where a bright band signature is present or absent in the radar reflectivity. Modeling studies have shown that moisture sources associated with ARs often contain tropical-sourced moisture at higher altitudes, while surface moisture originates in mid-latitudes and ascends within the warm sector as a result of the ageostrophic vertical circulation about the cold front (Bao et al., 2006; Sodemann and Stohl, 2013). Drop size distributions (DSDs) from disdrometer data have been used to investigate hypotheses that bright band signatures are a signature of a "seeder-feeder" process (Bergeron, 1950) where ice crystals within deeper cloud layers above the melting layer grow by riming, aggregation, and vapor deposition and subsequently melt as larger drops (Kingsmill et al., 2006; Martner et al., 2008; Neiman et al., 2017). These studies related the seeder-feeder mechanism to an orographically-influenced process where particles fall from a seeder cloud formed by large-scale ascent into a feeder cloud where moisture is formed by flow over mountainous terrain. White et al. (2003) found that 44% of precipitation from 3 months of AR events was attributed to the seeder-feeder process based on profiling radar observations. Non-bright band signatures are found to be associated with a greater concentration of smaller drops resulting from coalescence and condensation (Martner et al., 2008; Zagrodnik et al., 2018), and have been attributed to the absence of a seeder-feeder process.

Instrumentation deployed in the Pacific Northwest during the second Improvement of Microphysical Parameterization through Observational Verification Experiment (IMPROVE-2; Stoelinga et al., 2003) and Olympic Mountains Experiment (OLYMPEX; Houze et al., 2017) provided opportunities to observe cloud and precipitation information in situ; studies to date from these experiments have not explicitly focused on the microphysical properties through the depth of an AR. Crosier et al. (2014) examined the microphysical properties and relevant processes at different temperatures through a narrow cold-frontal rainband and associated warm conveyor belt region, but it is unclear whether this case study classified as an AR event. Other AR-related field experiments to date have not used instrumentation aboard aircraft to directly measure the particle sizes, shapes, and other morphological characteristics; microphysical studies based on observations through the vertical depth of ARs to date are very limited.

A target of opportunity to collect high spatiotemporal resolution measurements on the structure and microphysics of this AR over Australia and the Southern Ocean occurred on 28–29 January 2018 during the Southern Ocean Clouds, Radiation, Aerosol Transport Experimental Study (SOCRATES). This chapter is the second part of a larger study, with the first part (Rauber et al., 2019, in preparation) currently in review. Part I (Rauber et al., 2019) investigates the large-scale features of the AR using the WRF Model, dropsondes, and precipitation measurements from satellite and surface-based instruments. Rauber et al. (2019) documented the contribution of tropical-sourced moisture to the total moisture of an AR observed south of Hobart during the SOCRATES experiment. In Rauber et al. (2019), a water vapor tracer-enabled version of the Weather Research and Forecasting (WRF) Model was used to track the

lifecycle of moisture from tropical latitudes and mid latitudes prior to it falling as precipitation. Model analyses indicated that the tropical contribution to precipitation ranged between 40 and 70% for altitudes above 4 km (0 °C) within a cross section through the AR over Hobart, Tasmania (Fig. 4.1), showing that moisture of tropical origin played an important role in forming ice crystals and supercooled liquid water (SLW) aloft, and seeding the zone below the bright band, which was primarily mid-latitude moisture. The results were placed in the context of a seeder-feeder process different from that discussed in previous AR studies; the seeder and feeder regions were comprised of a continuous cloud layer through the depth of the AR, while the feeder region was the result of surface moisture ascending due to the ageostrophic circulation ahead of a frontal boundary rather than from ascent associated with elevated terrain. In this chapter, the microphysical evolution of particles within the seeder and feeder regions of this AR is analyzed using a vertically-pointing Doppler radar and a suite of microphysical instruments aboard the National Science Foundation/National Center for Atmospheric Research (NSF/NCAR) Gulfstream-V (G-V) aircraft that flew through the vertical depth of the AR precipitation band. These observations are interpreted in the context of the seeder-feeder mechanism (Fig. 4.2) hypothesized in past AR studies and the model results presented in Rauber et al. (2019) (Fig. 4.1). Microphysical features within the cloud are linked to the microphysical processes occurring within the AR that influence the concentration, phase, habits, and distribution of particle sizes within the seeder region.

The remainder of this chapter is organized as follows. Section 4.2 details the data sources used, flight strategy conducted, and the methodology employed to process the microphysics and radar data. The physical structure of the AR is discussed in section 4.3. The microphysical structure of the tropical-sourced seeder region is analyzed in section 4.4 and the microphysical characteristics of the mid-latitude-sourced feeder region is presented in section 4.5. Discussion of the microphysical processes involved as it relates to the seeder-feeder mechanism are summarized in section 4.6 while a summary of the results and key findings are given in section 4.7.

4.2 Data and methodology

Flight operations by the G-V during SOCRATES permitted collection of data presented in this chapter and Rauber et al. (2019). The radar and microphysical instrumentation and methodology used to process the data are described below.

4.2.1 HIAPER cloud radar

The NSF/NCAR HIAPER cloud radar (HCR; UCAR/NCAR – Earth Observing Laboratory [EOL] 2014), transmitting at 94.4 GHz (3-mm wavelength), was housed in a pod beneath the right wing of the G-V and was positioned at either zenith or nadir detecting liquid, ice, and mixed-phase cloud layers. The HCR was pointed at nadir during both transects

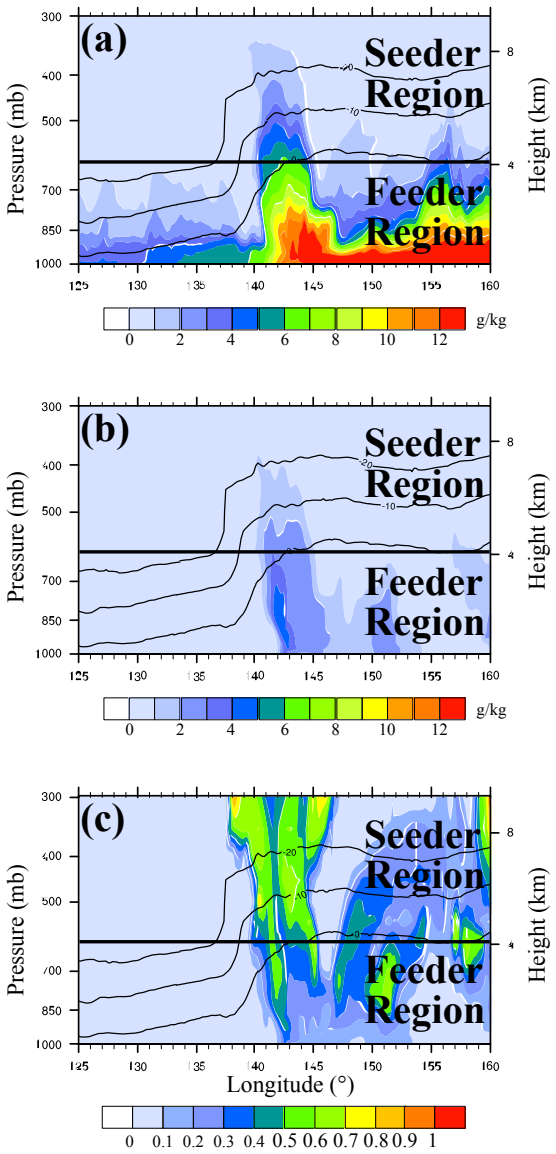

Figure 4.1: Vertical distribution of the (a) total mixing ratio, (b) mixing ratio associated with tropical-sourced moisture, and (c) ratio of tropical-sourced moisture to total moisture for a cross section through the AR at 0600 UTC 29 January based on model analyses from Rauber et al. (2019).

through the AR meaning that cloud top was not detected by the HCR unless the G-V was above cloud.

A series of calibrations were routinely performed to develop correction factors for the radar reflectivity (Z) and vertical radial velocity (V_R) measurements. Since radar performance can be affected by large temperature fluctuations during flight, a series of noise source calibration procedures was performed by measuring changes in the receiver gain when a noise signal, which was insensitive to temperature changes, was introduced to the radar (EOL 2018a). The ocean surface was used to perform ocean scan calibrations following the methodology of Li et al. (2005) by calculating the normalized radar cross section bias of the HCR (EOL 2018b). Following Liebe (1985) and International

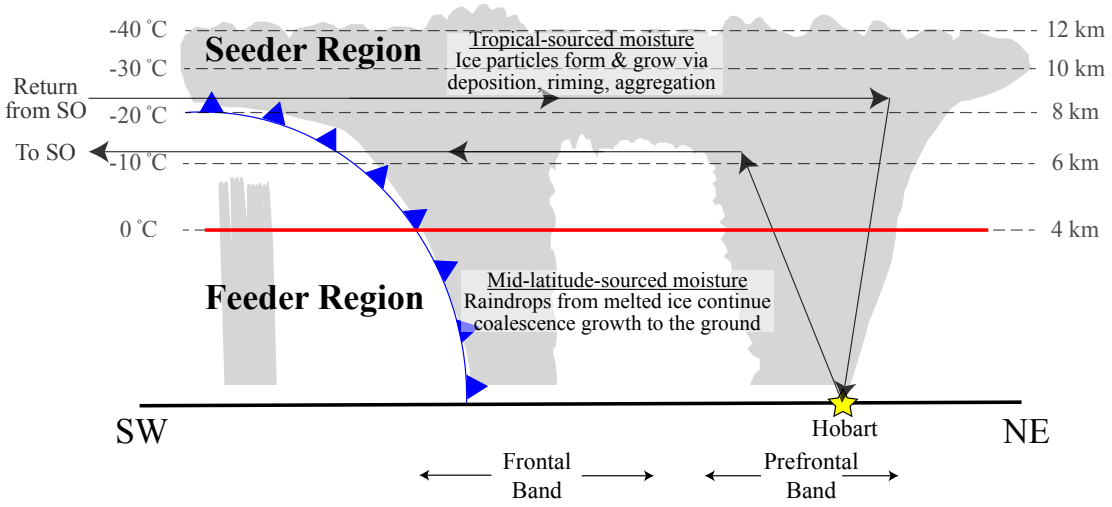

Figure 4.2: Schematic showing the general flight pattern (arrows) during two passes through the AR. Dashed lines denote typical temperatures and altitudes for the positions indicated. Thick line represents division between the seeder and feeder regions discussed in sections 4.4 and 4.5.

Telecommunication Union (2013), attenuation by atmospheric gases was calculated and corrections applied to the radar Z. Due to the high transmission frequency of the HCR (94.4 GHz), attenuation through liquid portions of the cloud was significant and no attempt was made to correct for attenuation by liquid-phase particles since the vertical distribution of liquid water content was unknown. Caution should therefore be used in interpreting the reflectivity data as the radar signal penetrated through SLW layers and rain below the bright band. The V_R was corrected for platform motion following Ellis et al. (2017) and Rauber et al. (2017) when the radar beam was pointed at nadir, and also by using inertial navigation system and GPS measurements. Finally, radar gates were masked if the normalized coherent power < 0.16 to eliminate noise.

4.2.2 Microphysics measurements

Several microphysical instruments were installed on the G-V during SOCRATES that measured the concentrations, sizes, shapes, scattering characteristics, and bulk mass contents of cloud- and precipitation-size particles. A brief description of the instruments and methods used to process the data relevant to this study are provided below.

SLW observations and bulk mass content

The Rosemont Icing Detector (RID) indicated periods when icing conditions were present by recording the voltage change (converted from a frequency measurement) as ice accreted on a vibrating sensing element (Baumgardner and Rodi, 1989). The RID is used qualitatively herein to detect regions of SLW for $T \leq$ -5 °C as the RID does not detect

SLW at higher temperatures due to dynamic heating of its wire. The cloud droplet probe (CDP) provided cloud droplet size distributions for diameters between 2 and 50 μm, while the King probe provided measurements of liquid water content (LWC).

Small particle images

Particle images were collected by the Particle Habit Imaging and Polar Scattering probe (PHIPS; Abdelmonem et al., 2016) to examine the morphological properties of small ice and liquid particles. The PHIPS provides microscopic images at an optical resolution of 2.5 μm using camera-telescope assemblies and an illumination laser. The PHIPS instrument also has a polar nephelometer that provides information on the particle phase by determining the scattering phase function from a scattering laser beam and a series of mirrors spaced at equiangular distances (Järvinen et al., 2016). High-resolution images from the PHIPS are used herein to help interpret particle imagery from optical array probes (OAPs), particularly when determination of particle phase and habit were inconclusive from OAP data.

OAP data

A 2D stereo (2D-S) probe, a 2D cloud (2D-C), and a precipitation imaging probe (PIP) were installed on the G-V to determine the particle size distributions (PSDs), mass concentrations, projected particle area, and other particle shape properties from shadowgraphs of liquid- and ice-phase hydrometeors. During SOCRATES the 2D-C periodically was susceptible to poor image quality as condensation caused fogging of the probe's optical lens. The PIP frequently suffered from communication issues corrupting particle boundaries in the image buffer data, preventing extraction of meaningful PSD information from the instrument. For these reasons, OAP data presented in this chapter are limited to those from the 2D-S probe, which has an optical resolution of 10 μm, and imaged particle sizes spanning $0.05 \leq D \leq 3.2$ mm. Particles smaller than 0.05 mm are not reported in this chapter given limitations of the probe's depth of field and uncertainties in the sample area for the smaller particles (Baumgardner and Korolev, 1997).

The 2D-S data were processed using the University of Illinois/Oklahoma OAP Processing Software (McFarquhar et al., 2018b), which calculates several morphological properties for individual particles (e.g., maximum dimension, projected area, area ratio, perimeter, and habit) and determines PSDs for each second of flight. Only particles identified as having their center within the OAP field of view were considered (Chapter 2) so that the uncertainties in particle size were minimized (Heymsfield and Baumgardner, 1985; Field, 1999).

The 2D-S probe was fitted with anti-shattering tips, which limited the impact of shattered artifacts (e.g., Korolev et al., 2011). As in Korolev et al. (2011), Korolev et al. (2013a), and Jackson et al. (2014), a shattering removal algorithm was used to further eliminate shattered artifacts from the PSDs. The shattering removal algorithm follows Field et al. (2006) by examining the distribution of elapsed times between particles entering the probe's sample vol-

ume (inter-arrival times; Field et al., 2003). This distribution follows a bimodal form when shattered artifacts are present, with naturally-occurring particles belonging to the mode with longer inter-arrival times and shattered artifacts belonging to the mode with shorter inter-arrival times. The minimum frequency between the peaks of the bimodal distribution was used as a threshold, and all particles whose inter-arrival time was below the determined threshold were rejected.

4.3 Physical structure of the AR

The G-V, stationed in Hobart, Australia during SOCRATES, was primarily tasked to sample marine boundary layer clouds in the cold sector of Southern Ocean mid-latitude cyclones during the January–February 2018 period. The AR was sampled as a target of opportunity.

An overview of the flight pattern as the aircraft sampled the AR following its departure from Hobart and return to Hobart is provided in Figs. 4.2 and 4.3. The retrieved cloud properties valid at 2320 UTC 28 January (Figs. 4.3a,b) and 0530 UTC 29 January (Figs. 4.3c,d) were produced following the processing techniques of Minnis et al. (2008) and Minnis et al. (2011) while the Ku-band (13.6 GHz) reflectivity profile is from a Global Precipitation Measurement (GPM) overpass during the AR event (Fig. 4.3e) illustrates the cloud structure with a prefrontal band, frontal band, and anvil region present.

At takeoff at 2255 UTC on 28 January 2018 the AR was located directly over Hobart (Figs. 4.3a,b). The aircraft ascended through the AR until it reached a cruising altitude of 6.1 km by 2305 UTC. Unfortunately, detailed measurements during this vertical profile through the AR were limited for the departure flight leg because instruments were only being brought online following takeoff. For this reason, only the constant-altitude portion of the flight on departure is analyzed here. The aircraft flew through the frontal band and anvil region of the AR, where the mean cloud top height was 8.4 $\pm$ 1.1 km and mean cloud top temperature was -26.1 $\pm$ 8.1 °C (Figs. 4.3a,b). Estimated cloud top height and radar data indicated that the depth of the anvil region ranged from 3–3.5 km (Figs. 4.2, 4.3). Radar cross sections indicated that a second cloud layer was present below the anvil region where post-frontal convection was observed (Fig. 4.4). Pockets of positive V_{r} values correspond to updraft regions near the top of the detached cloud layer between 232835 and 232900 UTC with fall streaks emanating from some of the convective elements. While the melting layer is not clearly shown in Fig. 4.4, dropsonde measurements taken at 2337 UTC indicate the melting layer is at 3 km behind the front. The aircraft exited the AR's western edge by 2340 UTC, where it then continued southward over the Southern Ocean (Fig. 4.2).

Since the AR was still positioned over Hobart upon return of the G-V, project scientists modified the flight plan to sample the AR again. The G-V climbed to 8 km (-20 °C) prior to reaching the AR, as it entered the western side of

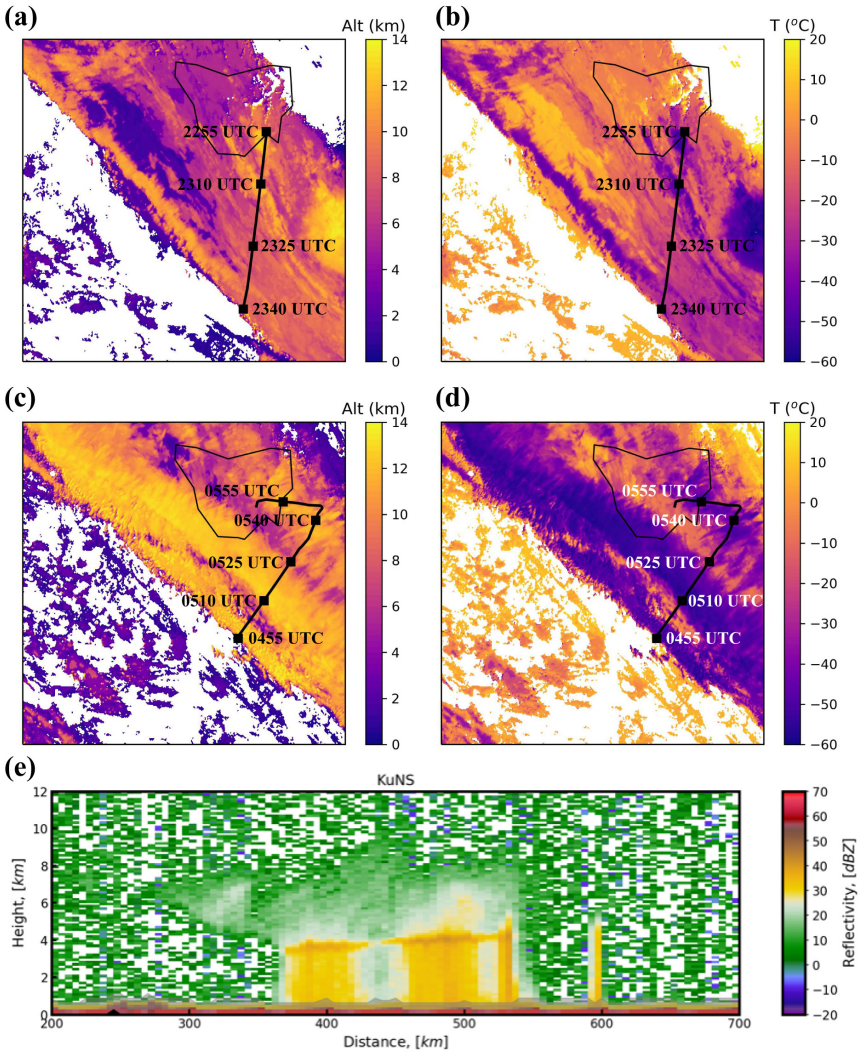

Figure 4.3: Retrieved (a,c) cloud top height and (b,d) cloud top temperature from the Himawari-8 satellite valid at 2320 UTC 28 January (top) and 0530 UTC 29 January 2018 (middle). G-V flight track in black and aircraft position annotated every 15 minutes. (e) Global Precipitation Measurement (GPM) profile of Ku-band equivalent radar reflectivity factor valid at 1908 29 January 2018 along GPM orbit 022280.

the AR at 0455 UTC on 29 January (Figs. 4.3c,d), and then descended from 8 km at 0550 UTC through the prefrontal rainband and towards the Hobart airport before landing at 0605 UTC (Fig. 4.2). Cloud top height estimated from satellite observations (Figs. 4.3c) indicated that the cloud depth was greater than the aircraft's flight to the Southern Ocean 6 hours prior, with a mean cloud top height of 10.2 $\pm$ 2.6 km in the anvil and frontal regions and 10.2 $\pm$ 1.4 km in the prefrontal region. Cloud top temperatures were also lower than during the departure flight leg, with a mean cloud top temperature of -47.8 $\pm$ 5.4 °C through the frontal band and -37.5 $\pm$ 10.3 °C through the prefrontal band (Figs. 4.3d).

Post-frontal convection was observed during the return leg to Hobart, albeit significantly more shallow compared

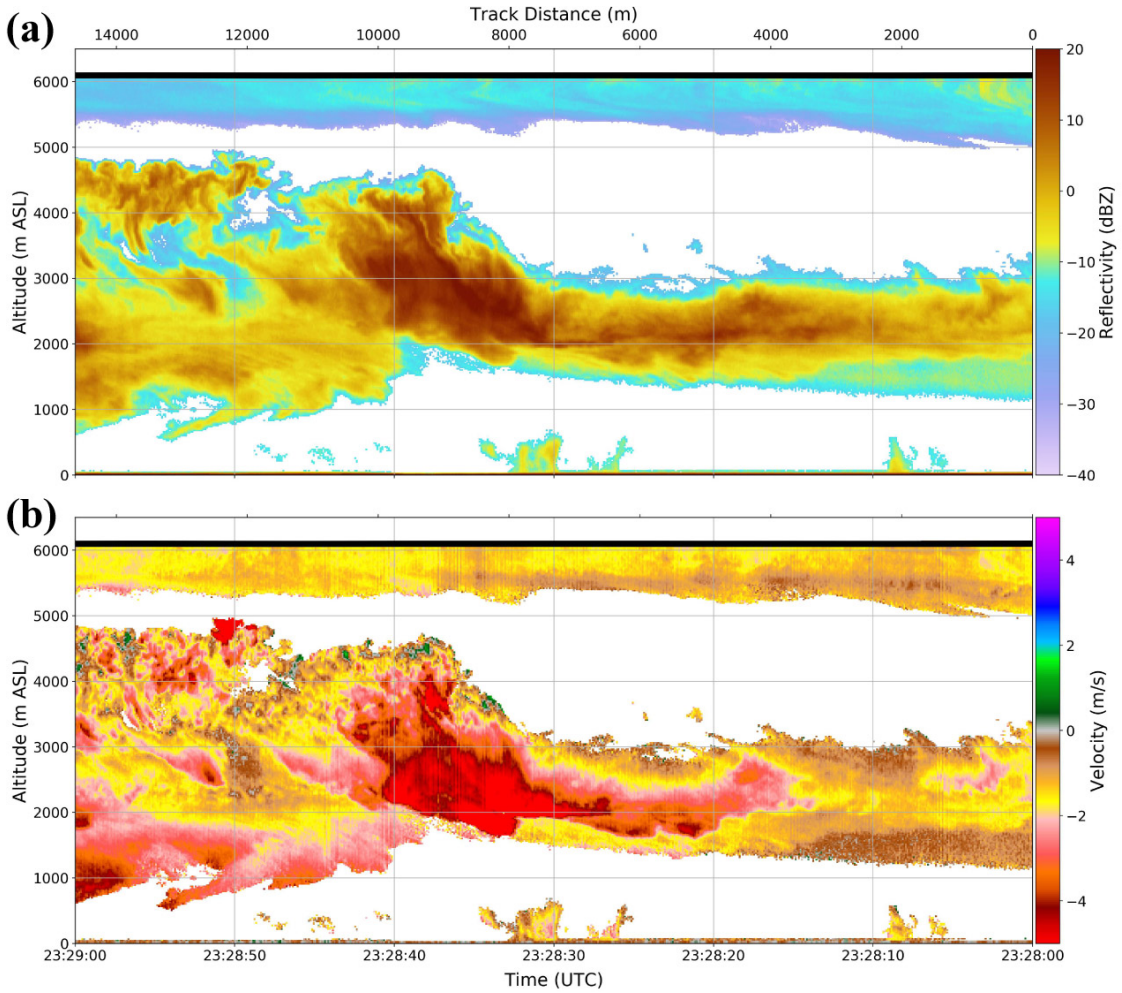

Figure 4.4: Radar cross sections of (a) Z and (b) V_r for 2328–2329 UTC 28 January.

to earlier in the flight with clouds confined to the lowest kilometer (Fig. 4.5). Near the anvil base, horizontal variations in V_r were occasionally observed. Local minima in the Z field along the anvil base between 0516 and 0517 UTC 29 January were collocated with regions of alternating larger V_r (updrafts) and smaller V_r values (downdrafts) (Fig. 4.5). The downdrafts near anvil base are likely driven by sublimative cooling while the corresponding updrafts are a response to the sinking motion in the downdraft regions. The closely spaced updrafts and downdrafts near the anvil base illustrates the turbulent character of the anvil base.

4.4 Microphysical structure of the tropical-sourced seeder region

The precipitation structure and microphysical observations pertaining to the tropical-sourced seeder region of the AR are detailed in this section. Microphysical measurements were made above the melting level prior to 055530 UTC as indicated by the radar bright band signature, vertical gradient in the radial velocity V_r, and temperature values

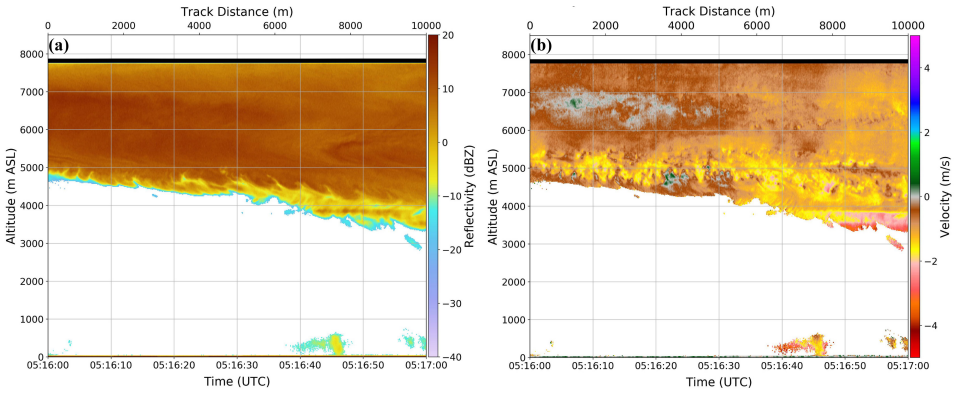

Figure 4.5: As in Fig. 4.4, but for 0516–0517 UTC 29 January.

$\leq$ 0 °C (Figs. 4.6a–c). Complete attenuation of the radar signal was occasionally observed due to the presence of liquid water in the vertical column. The top of the gray-shaded region in Figs. 4.6a,b denotes the cloud top altitude from derived satellite data (Fig. 4.3c), with values ranging from 9–12 km and corresponding cloud top temperatures between -50 and -30 °C. Microphysical properties at the -20 °C flight level, the -10 °C flight level, and the evolution of the microphysical characteristics during the aircraft's descent down to the melting level, the base of the seeder region based on Fig. 4.21, are discussed in the subsections below.

4.4.1 Microphysical characteristics at the -20 °C flight level

Towards the end of its mission, the G-V made a constant-altitude pass through the anvil region, frontal band, and part of the prefrontal band of the AR at -20 °C (8 km; Fig. 4.2). The flight through the anvil region at -20 °C occurred between 0507 and 0518 on 29 January, although the anvil base was above the aircraft's altitude as early as 0455 UTC (Figs. 4.6a,b). At 0508 UTC, the cloud top height was 11 km and the temperature at cloud top was -42 °C (Figs. 4.3c-d). LWC values were negligible throughout the anvil region and frontal band at the aircraft altitude (Fig. 4.6d).

Ice particle concentrations (N_{2DS}; $0.15 \leq D \leq 3.2$ mm) within the anvil region at -20 °C averaged 10.6 $\pm$ 5.8 L^{-1} (Fig. 4.6e). Representative particle images from the 2D-S and PHIPS show that bullet rosettes were observed (Fig. 4.7) and habit classification of the 2D-S images indicate that rosettes were the second most dominant habit by number behind irregular crystals for particles larger than 0.5 mm. The N(D) for $D \leq 0.7$ mm was characterized as a broad distribution of particle sizes. Bailey and Hallett (2009) showed in field experiments that bullet rosettes falling into regions warmer than -40 °C typically develop plate-like components since the plate-like regime occurs between temperatures of -40 and -20 °C. Plate-like growth associated with the bullet rosettes was common in images at -20 °C (Fig. 4.7b). While these mixed rosettes remained the second most dominant habit for $D \geq 0.5$ mm across the frontal band (0518–0522 UTC), number concentrations from the 2D-S increased to a mean value of 23.9 $\pm$ 14.3 L^{-1} with a peak in the N(D) occurring between 0.1 and 0.2 mm. Particles in this size range were identified as quasi-spherical

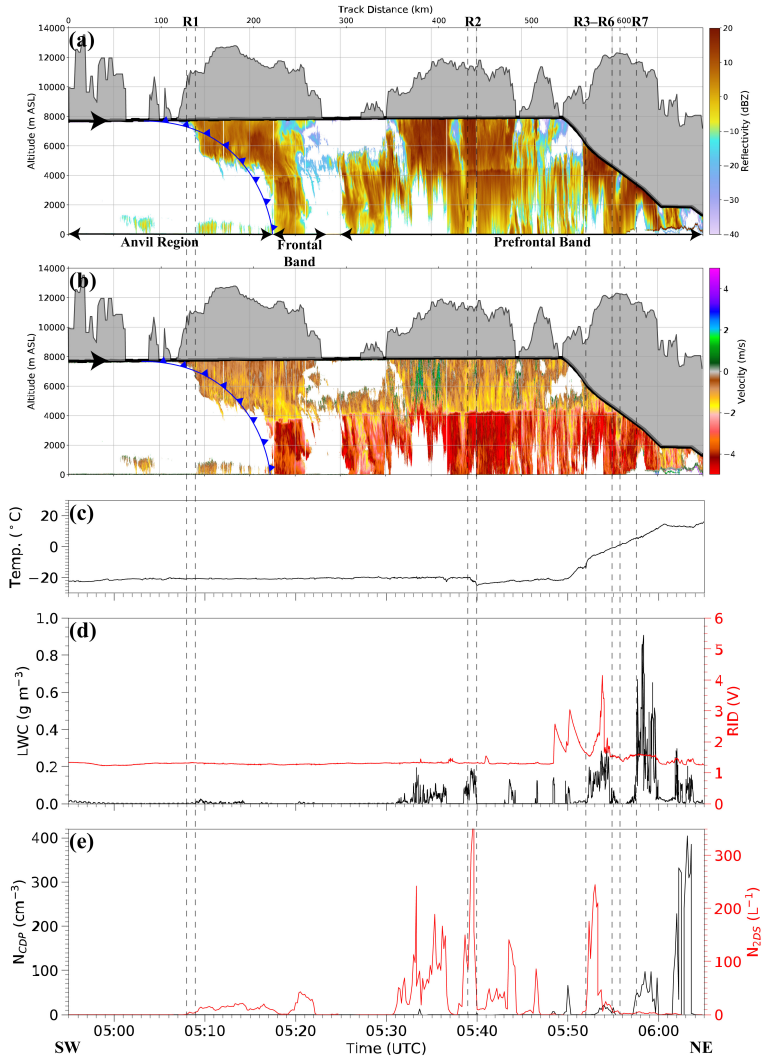

Figure 4.6: Radar cross section of (a) equivalent radar reflectivity factor Z and (b) radial velocity V_r from the HIAPER Cloud Radar (HCR) from 0455–0605 UTC 29 January. Aircraft location is denoted by the black line and the region shaded gray is bounded by the aircraft altitude and estimated cloud top height. The prefrontal band, frontal band, anvil region, and estimated frontal position are labeled. Time series of (c) temperature, (d) liquid water content (LWC; black) and Rosemont icing detector (RID) voltage (red), and (e) number concentration from the cloud droplet probe (CDP; black) and 2D stereo (2D-S) probe ($0.15 \leq D \leq 3.2$ mm; red) also shown. Regions R1–R7 indicate time segments used for expanded radar cross sections and detailed microphysical analyses.

ice from habit classification of the 2D-S images and inspection of the PHIPS images, and SLW remained nonexistent based on the King probe, RID, and CDP (Fig. 4.6).

Most of the flight segment across the prefrontal band (0530–0545 UTC) at -20 °C was characterized by stronger updrafts and downdrafts compared to flight through the frontal band at -20 °C based on measurements of vertical velocity at the aircraft's altitude (w) and deeper within the cloud based on V_r measurements. Standard deviation in w was 2.7 times greater than the anvil region and frontal band at -20 °C. The minimum and maximum w for each 10-s period at -20 °C in the prefrontal band, shown in Fig. 4.8a, indicates that downdrafts were occasionally on the order

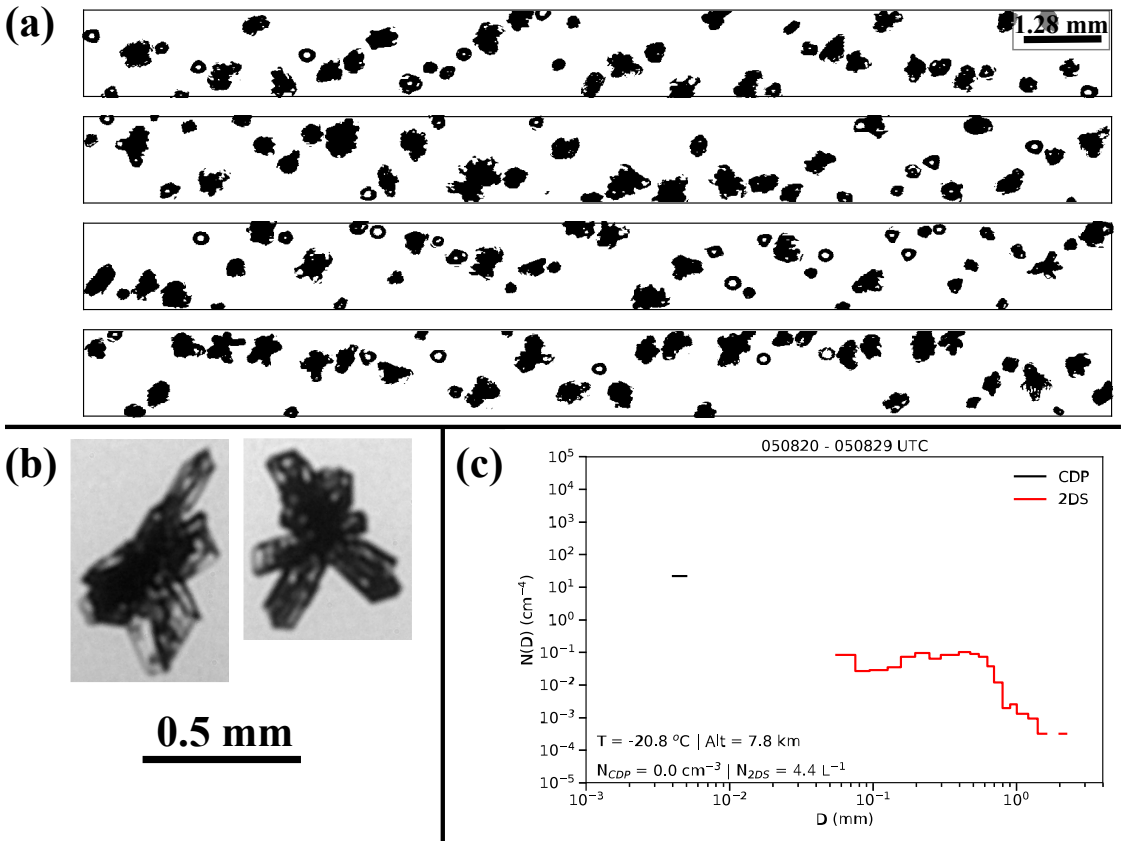

Figure 4.7: Representative images from the (a) 2D-S and (b) PHIPS instrument and (c) 10-s mean number distribution function N(D) from the CDP ($D < 50$ μm) and 2D-S ($50 \leq D < 3200$ μm) for area R1 in Fig. 4.6 (050820–050829 UTC 29 January).

of 2–3 m s^{-1}. Those downdrafts coincided with reductions in the temperature around 0535 and 0539 UTC (Fig. 4.6) as cooler air from above the aircraft's location descended into the region. Updrafts were occasionally on the order of 1.5–2.5 m s^{-1}.

Number concentrations of ice were also highly variable between 0530 and 0545 UTC, with N_{2DS} averaging 62.3 $\pm$ 73.2 L^{-1} and the N_{2DS} distribution skewed towards larger values (Fig. 4.6e). Concentrations exceeded 100 L^{-1} for 12 10-s periods, with the highest concentrations corresponding to downdrafts of 2–3 m s^{-1} (Fig. 4.8b). Cross sections of Z and V_r along with time series of w, LWC, RID voltage, N_{CDP}, and N_{2DS} are shown in Fig. 4.9 for the prefrontal band for a one minute period beginning at 0539 UTC. The aircraft sampled across updrafts and downdrafts located between altitudes of 6 and 8 km (Fig. 4.9b), with downdrafts as large as 3 m s^{-1} and updrafts as large as 2 m s^{-1} during the one minute period at the flight level (Fig. 4.9c). Droplet concentrations from the CDP remained below 2 cm^{-3} as the aircraft entered an updraft region around 053950 UTC (Figs. 4.9e).

The vertical lines in Figs. 4.9a–e denote the 10-s period where the greatest concentration was observed by the 2D-S during flight. Images from the 2D-S and PHIPS illustrate the abundance of columns, some of which are capped

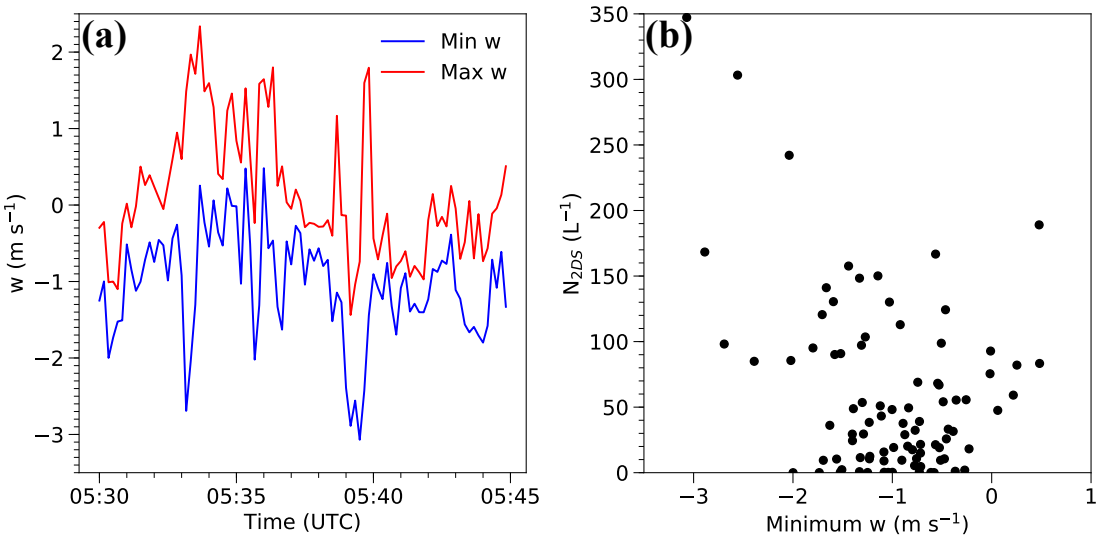

Figure 4.8: (a) Time series of the minimum (blue) and maximum w (red) for each 10-s interval, and (b) N_{2DS} as a function of the minimum w for the same 10-s intervals.

by plate-like structures, in the 0.3–0.6 mm size range. The presence of these columns correspond to a peak in the N(D) between 0.3 and 0.6 mm, owing to concentrations exceeding 300 L^{-1}. Bailey and Hallett (2009) found that columns originating from lower temperatures and falling into the plate-like regime where ice supersaturations are between 0.1 and 0.2 can be hollow or be capped by plates, consistent with the particles observed in Fig. 4.9. The relation between downdraft speed, particle ice concentration, and particle habit (Fig. 4.9) suggests that ice crystals from above the aircraft's location were transported downward in downdrafts to the -20 °C level where measurements were made.

4.4.2 Microphysical characteristics at the -10 °C flight level

The flight through the frontal band and lower anvil region for the pass at -10 °C occurred between 2310 and 2340 UTC 28 January. Radar cross sections of Z and V_r and time series of temperature, LWC, RID voltage, N_{CDP}, and N_{2DS} are plotted in Fig. 4.10 so that the left side of each panel corresponds to the southwest extent of the flight leg, as in Fig. 4.6. Cloud top heights based on Himawari retrievals were generally lower and cloud top temperatures higher than the pass at -20 °C (section 4.3, Fig. 4.3).

The G-V flew through the frontal band between 2310 and 2320 UTC, through a series of precipitation fall streaks evident on the radar (Fig. 4.10a). Two sets of fall streaks present between 2316 and 2317 UTC are expanded in Fig. 4.11. As the aircraft penetrated these fall streaks the droplet number concentrations briefly approached 9 cm^{-3} and LWC values ranged between 0.05 and 0.1 g m^{-3} in local areas, but was generally negligible. The fall streak occurring between 231645 and 231655 UTC contained some SLW as N_{CDP} was 1.9 cm^{-3} (Fig. 4.11h). These concentrations briefly increased to 5.2 cm^{-3} before the aircraft exited the fall streak (Figs. 4.11a,e). While the 2D-S N(D) indicates

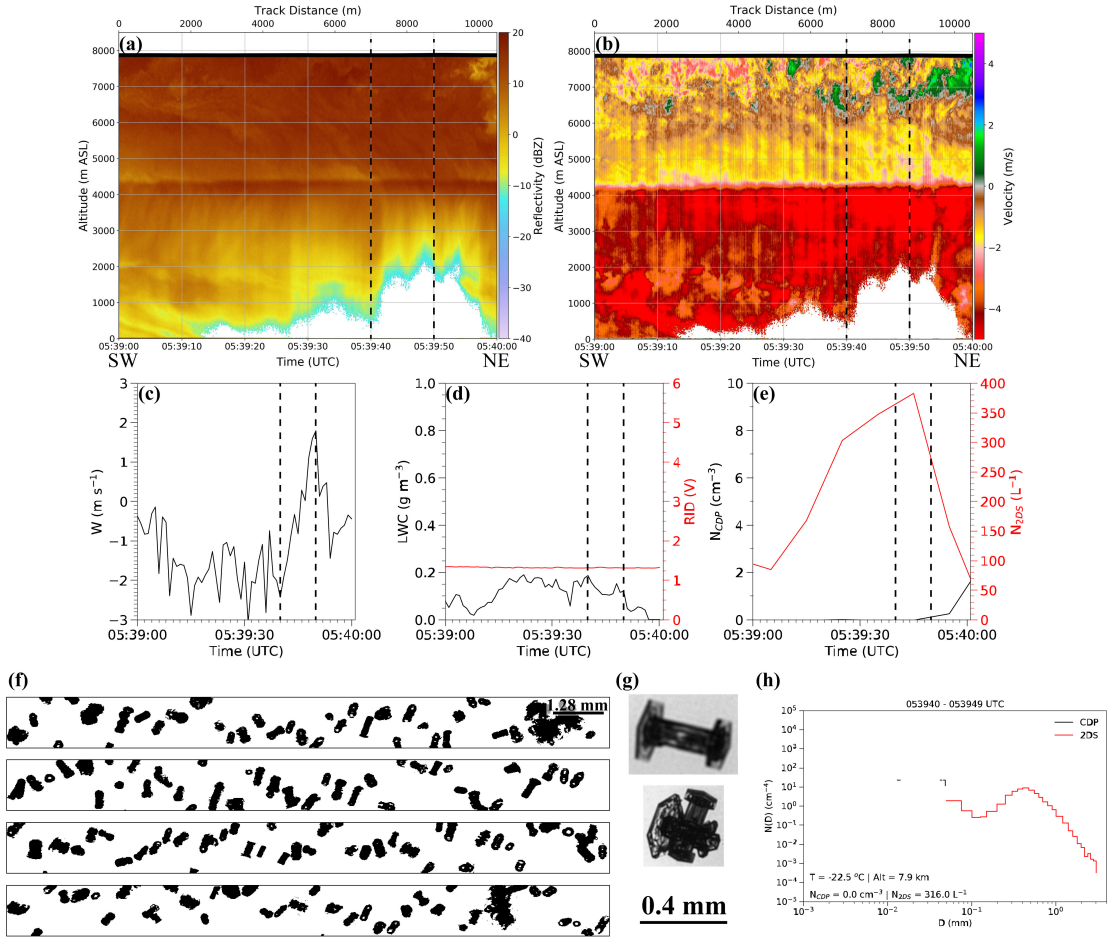

Figure 4.9: Radar cross sections of (a) Z and (b) V_r for area R2 in Fig. 4.6 (0539–0540 UTC 29 January). Times series of (c) vertical velocity w, (d) LWC (black) and RID voltage (red), and (e) N_{CDP} (black) and N_{2DS} (red) also shown for the same period. Times within the dashed lines correspond to the period depicted in (f)-(h). (f)–(h) As in Fig. 4.7.

a fairly broad distribution of ice particle sizes (Fig. 4.11h), the mode of higher concentrations between 0.4 and 1 mm are likely associated with an abundance of columns present in the particle images from the 2D-S and the PHIPS (Figs. 4.11f,g). Complexities in the particle perimeter from the 2D-S images and freezing of SLW droplets onto the columns shown in the PHIPS images suggest an active riming process at this temperature.

Twenty seconds later, the aircraft penetrated another fall streak (Fig. 4.12a) characterized by a sharp transition from primarily ice particles to a region dominated by smaller SLW droplets. Particle images from the 2D-S indicate this abrupt change in particle habit during the 231730–231739 UTC period (Fig. 4.12c). Within the span of 1 second the presence of irregularly-shaped crystals and supercooled drops were replaced by a high concentration of SLW droplets. The supercooled droplets, represented by the spherical PHIPS particles and exhibiting a smooth appearance along the perimeter and a Poisson (or Fresnel diffraction) spot in the center of the particle, and are on the order of 50–100 μm in size (Figs.4.12g,h). A response from the RID voltage was observed and LWC values approached 0.4 g

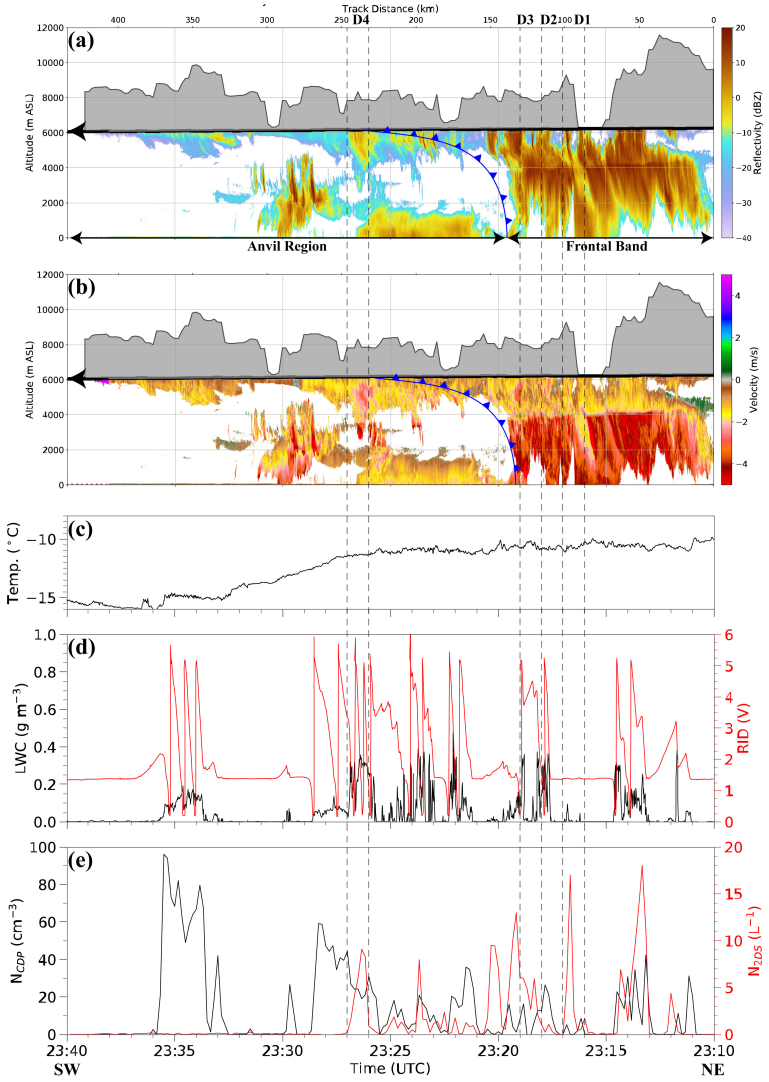

Figure 4.10: As in Fig. 4.6, but for 2310–2340 UTC 28 January. The left side corresponds to the southwest extent of the flight leg as in Fig. 4.6. Regions D1–D4 indicate time segments used for radar cross sections and detailed microphysical analyses.

m^{-3} during this period (Fig. 4.12d). Examination of *w* during this period indicates that the aircraft entered a region of weak updraft as *w* values were on the order of 1 m s^{-1}. Updraft speeds of this magnitude appear significant enough to transport supercooled droplets from lower altitudes up to the aircraft's position.

The aircraft flew into and out of another series of fall streaks between 2318 and 2319 UTC, where *w* ranged between -1.5 and 0.3 m s^{-1} (Figs. 4.13a–c). The fall streaks during this one minute period contained a mixture of ice particles and supercooled droplets, with brief increases LWC observed with maxima ranging between 0.15 and 0.4 g m^{-3} (Fig. 4.13d). As the G-V flew between fall streaks during the 231830–231839 UTC period, particle images from the 2D-S indicated that an abundance of dendrites were observed during this time (Fig. 4.13f), indicating that particles within this region fell from altitudes above the aircraft in the -18 to -12 °C temperature range where dendrites most

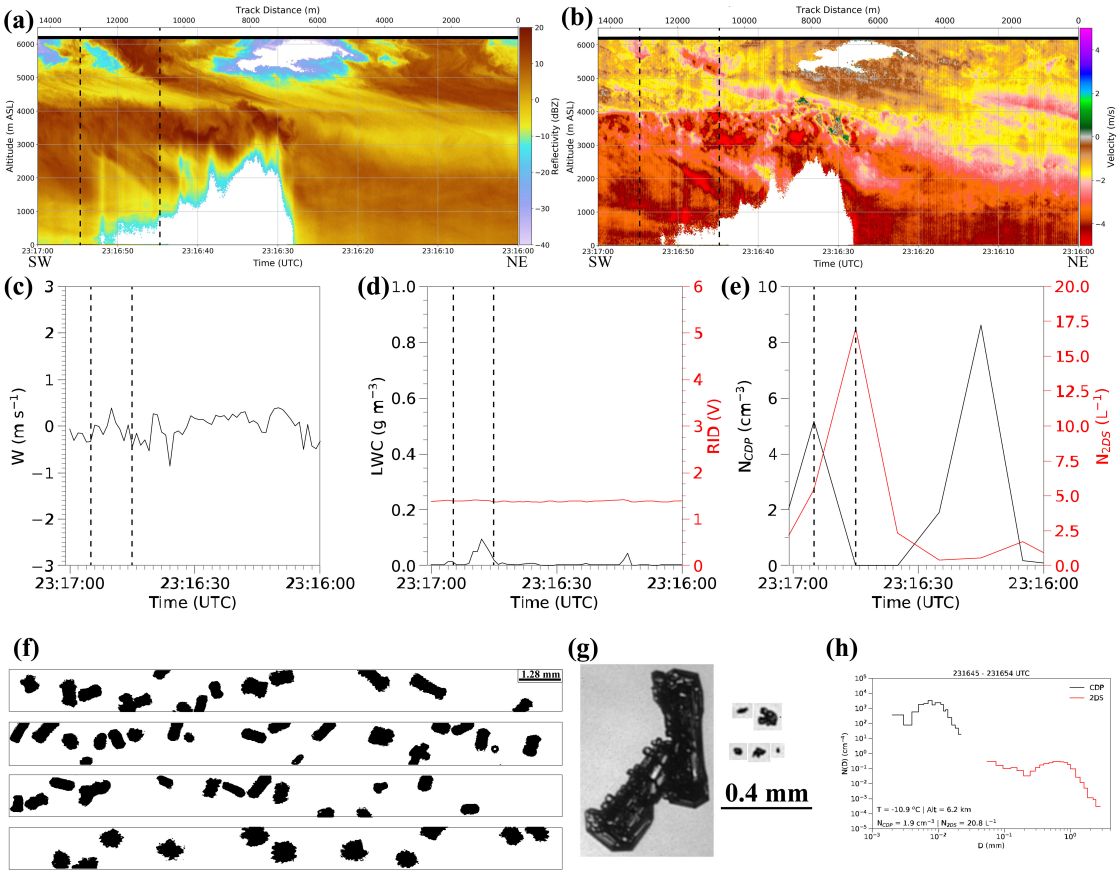

Figure 4.11: As in Fig. 4.9, but for region D1 in Fig. 4.10 (2316–2317 UTC 28 January).

commonly form (e.g., Bailey and Hallett, 2009). While number concentrations from the CDP suggest that supercooled drops at the aircraft altitude were not present, riming of the dendrites appears to have occurred above the flight altitude based on the rough appearance along the crystal surface in PHIPS images (Figs. 4.13g,h). Small ice particles also coexisted with the larger ice crystals given the irregular shape and absence of a diffraction spot in 2D-S and PHIPS images (Figs. 4.13f,g). Aggregation also had begun by the time passed through -10 °C, as particles as large as 3 mm were observed in the N(D) (Fig. 4.13c).

The southwest transect through the anvil region of the AR began around 2320 UTC as precipitation echo below 4 km became broken in nature (Fig. 4.10). Cross sections of radar Z and V_r and time series of w and microphysical properties for the one-minute period beginning at 2326 UTC are shown in Fig. 4.14. The G-V intersected the frontal boundary during that minute. During this one-minute period w ranged between -0.7 and 0.4 m s^{-1} (Fig. 4.14c), indicating that particles measured at the aircraft's location primarily originated from higher altitudes and fell at speeds close to their terminal fall velocity. Temperature values began to fall at 232620 UTC (Fig. 4.10c), signifying that the aircraft intersected the frontal boundary. Fall streaks in the anvil region were heavily influenced by sheared flow near the front. Around the same time, N_{2DS} values began to rapidly decrease from 9 L^{-1} to below 1 L^{-1} while

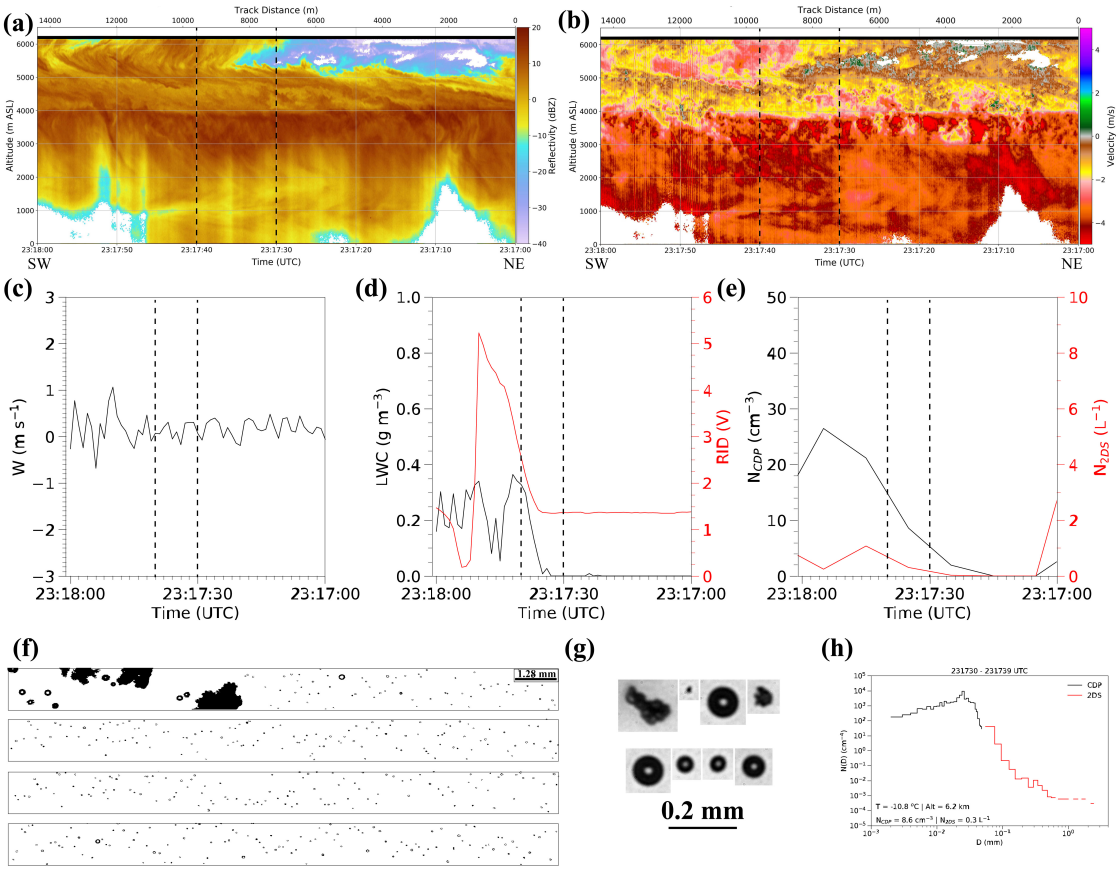

Figure 4.12: As in Fig. 4.9, but for region D2 in Fig. 4.10 (2317–2318 UTC 28 January).

N_{CDP}, LWC, and fluctuations in the RID voltage show that supercooled droplets dominated cloud near the -10 °C level (Figs. 4.14d,e).

4.4.3 Evolution of microphysical characteristics between -14 and 0 °C during descent

The aircraft began its descent from -20 °C around 0550 UTC, and re-entered the precipitation band at T = -14 °C around 055140 UTC. An expanded cross section of Z and V_r and time series of temperature and microphysical measurements for the descent through the seeder region of the prefrontal band appears in Fig. 4.15.

The G-V descended as it entered cloud at 055130 UTC, and over a one minute period the temperatures increased from -14.2 to -7.2 °C (Fig. 4.15c). Vertical velocity at the aircraft level averaged -0.9 $\pm$ 0.4 m s^{-1} and SLW was absent until the end of the one minute period (Figs. 4.16a–c). By 055150 UTC a broad distribution of ice particles were observed with sizes as large as 2.5 mm (Fig. 4.16e). Habit classification of the 2D-S images (Fig. 4.16d) indicated that irregular and dendritic crystals were the dominant habits by number for $D \geq 0.7$ mm. By 055205 UTC, the first signs of columnar crystals were observed at -9 °C (Fig. 4.16f) and supercooled droplets were also imaged by the 2D-S and PHIPS. The presence of SLW was minimal at this time, however, as number concentrations from the CDP were

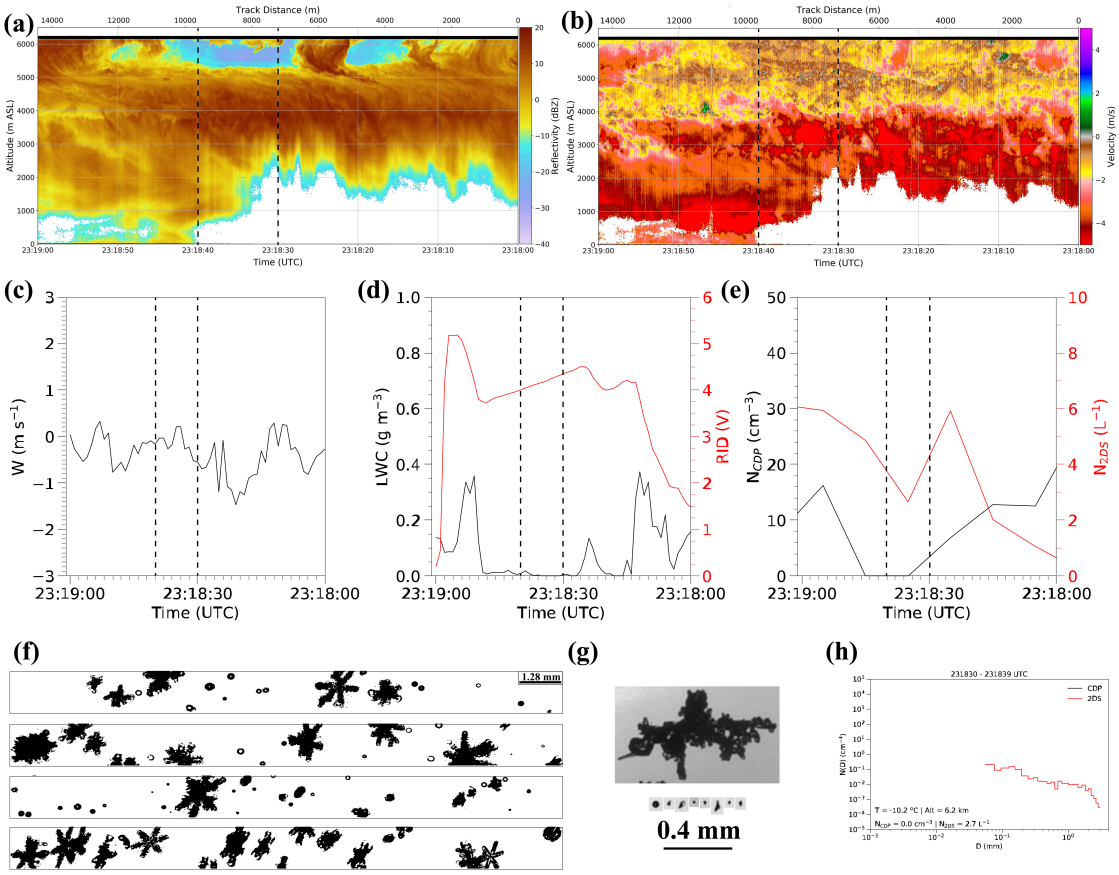

Figure 4.13: As in Fig. 4.9, but for region D3 in Fig. 4.10 (2318–2319 UTC 28 January).

0 cm^{-3} (Fig.4.16g) and LWC was below 0.05 g m^{-3} (Fig. 4.16b). Values of N_{2DS} during this period were 21.4 L^{-1} (Fig.4.16g).

By 055230 UTC, the temperature was -7 °C and concentrations from the 2D-S were 18 times greater than 40 seconds prior with an N_{2DS} of 105.7 L^{-1} (Fig. 4.17c). Particles imaged by the 2D-S indicate that columns and needles were the most common ice particle habit, with many of the particles in the 0.2–0.7 mm range (Fig. 4.17). The coexistence of liquid cloud droplets smaller than 13 μm (Fig. 4.17c), drops larger than 25 μm (Figs. 4.17a,c), and larger ice crystals between -8 and -3 °C are consistent with secondary ice production via the rime splintering process observed with laboratory studies and *in situ* measurements (e.g., Hallett and Mossop, 1974; Field et al., 2016).

Variability in the height of the maximum vertical V_r gradient, which is typically related to the melting level, was periodically observed between altitudes of 4 and 5 km (Fig. 4.18a). Regions where V_r values $\leq$ -2 m s^{-1} extend above the melting level of around 4.2 km appear to be related to the presence of SLW. Microphysical observations through a 10-s period when the G-V penetrated through a 1-km region where $V_r \leq$ -2 m s^{-1} show an abrupt change in the types of particles observed between 055330 and 055339 UTC (Fig. 4.18c). An increase in the LWC from 0.1 to 0.3 g m^{-3} and a change in the RID voltage during the beginning of the 10-s period (Fig. 4.6d) is correlated *w* values around 1

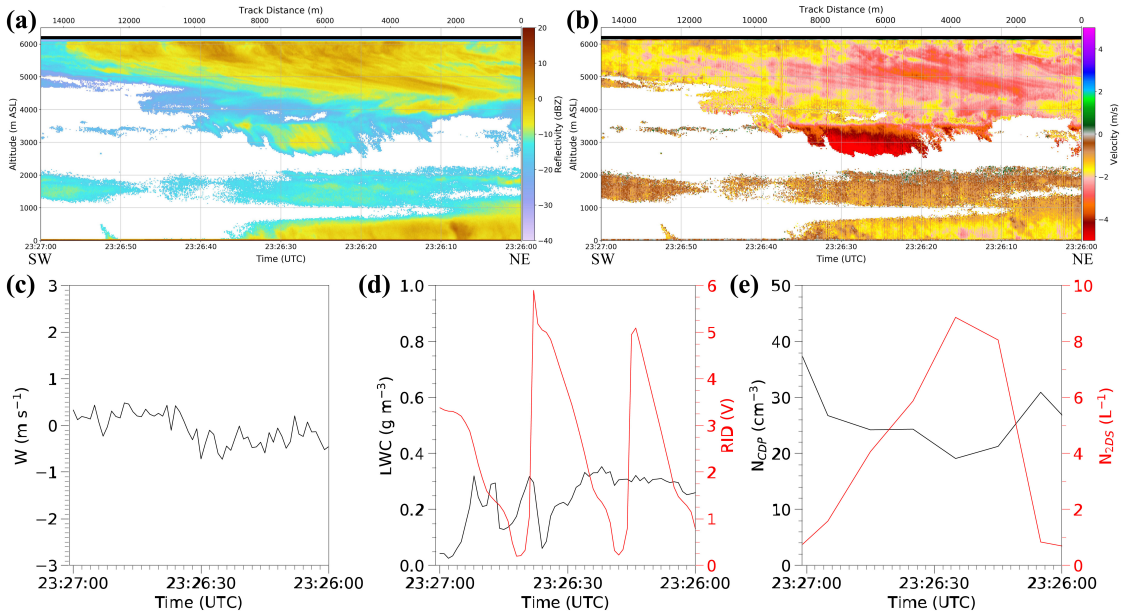

Figure 4.14: As in Fig. 4.9, but for the area D4 in Fig. 4.10 (2326–2327 UTC 28 January).

m s^{-1}, suggesting that supercooled droplets were lofted from lower altitudes through the 0 °C level. Greater droplet concentrations of 15 cm^{-3} (Fig. 4.18e), having a greater fall speed than ice crystals and aggregates of similar size, may explain why more negative V_r values were observed at altitudes above the melting layer. When a greater concentration of small droplets were observed following the updraft, ice particles were primarily limited to those larger in size with apparent riming suggested by the 2D-S images (Fig. 4.18c).

As the aircraft continued its descent and temperatures increased to values outside of the zone favorable for rime splintering, concentrations of ice particles decreased to 5–20 L^{-1} associated with aggregation. By 055440 UTC, temperatures within the cloud were around -1 °C and the aircraft was within 300 m of the melting level (Fig. 4.6). Figure 4.19 shows that aggregation was occurring at this level, with larger hydrometeors observed by the 2D-S and PHIPS. The mean N(D) for the period shows particles as large as 3 mm, but larger particles may have been present since the imaging view of the 2D-S is limited in its sampling of larger particles.

4.5 Microphysical characteristics of the mid-latitude-sourced feeder region

The aircraft descended below the melting level by 055530 UTC, and by 055540 UTC all ice was melted as temperatures were warmer than 1 °C (Figs. 4.20a,b). Larger particles at this altitude (4.3 km) represent those seeded from the primarily tropical-sourced moisture above the 0 °C level (section 4.4). The drop size distribution (DSD) during this time was characterized by a broad distribution of particle sizes with the largest drops around 1 mm and LWC values of around 0.05 g m^{-3} (Fig. 4.6d).

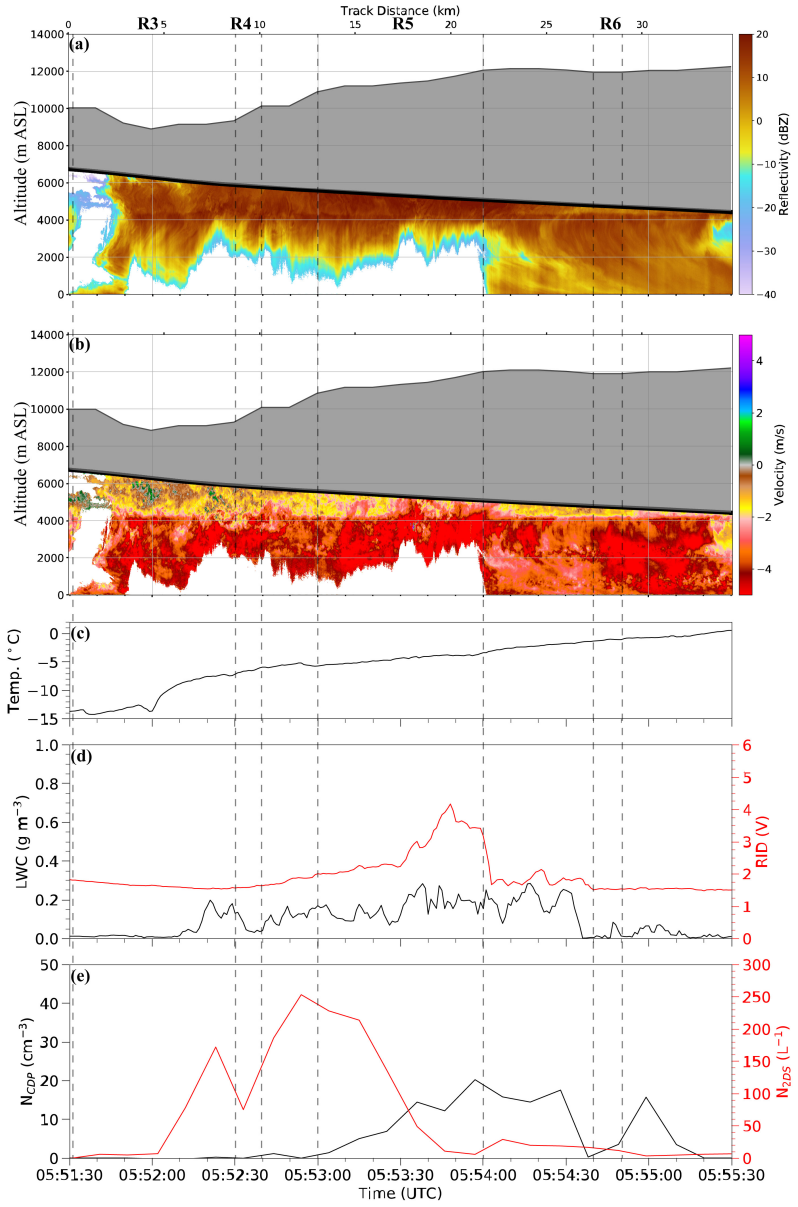

Figure 4.15: As in Fig. 4.6, but for 055130–055530 UTC 29 January. Regions R4–R7 indicate time segments used for expanded radar cross sections and detailed microphysical analyses.

The model results of Rauber et al. (2019) show that the vertical distribution of the total mixing ratio was largely confined to the feeder region below 4 km (Fig. 4.1a). This moisture allowed for the production of many small droplets, with concentrations averaging 47.2 $\pm$ 30.2 cm^{-3} between 0 and 10 °C and values up to 104 cm^{-3}, that were collected by lower concentrations of larger drops (1.1 $\leq N_{2DS} \leq$ 5.3 L^{-1}). Deeper within the feeder region, the presence of drops approaching 3 mm (Figs. 4.20c,d) coincided with an increase in LWC values as high as 0.9 g m^{-3} (Fig. 4.6d). The presence of larger drops at lower altitudes permitted drop growth through collision with and coalescence of cloud droplets as the hydrometeors precipitated towards the surface. Maximum drop sizes of 3 mm were present until 0600

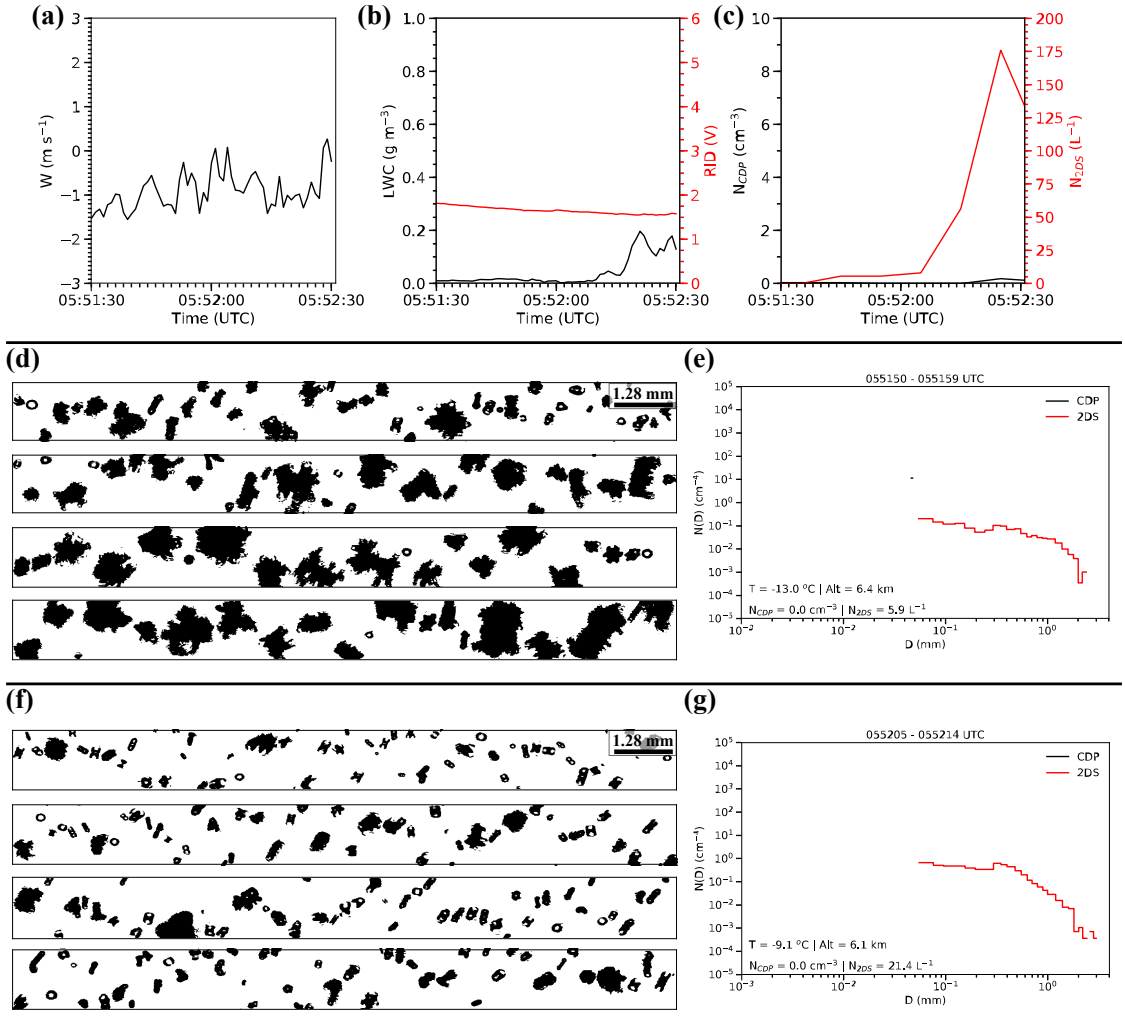

Figure 4.16: Time series of (a–c) w, LWC, RID voltage, N_{CDP} and N_{2DS} for region R3 in Fig. 4.15 (055130–055230 UTC 29 January). Particle images from the (d,f) 2D-S and (e,g) 10-s averaged N(D) for the (d,e) 055150–055159 UTC and (f,g) 055205–055214 UTC 29 January periods.

UTC when the G-V exited the main precipitation band.

4.6 Discussion

A schematic summarizing the microphysical processes occurring within the AR based on radar and microphysical observations presented herein is provided in Fig. 4.21. The AR consisted of a prefrontal band, frontal band, and anvil region with cloud top heights extending above 12 km and cloud top temperatures as low as -50 °C. The seeder region between cloud top and the melting layer (4 km) represented particles that were seeded from the primarily tropical-sourced moisture originating from northwest Australia above 0 °C and the feeder region between the melting layer and surface consisted of mid-latitude-sourced moisture. Post-frontal convection was also observed behind the frontal

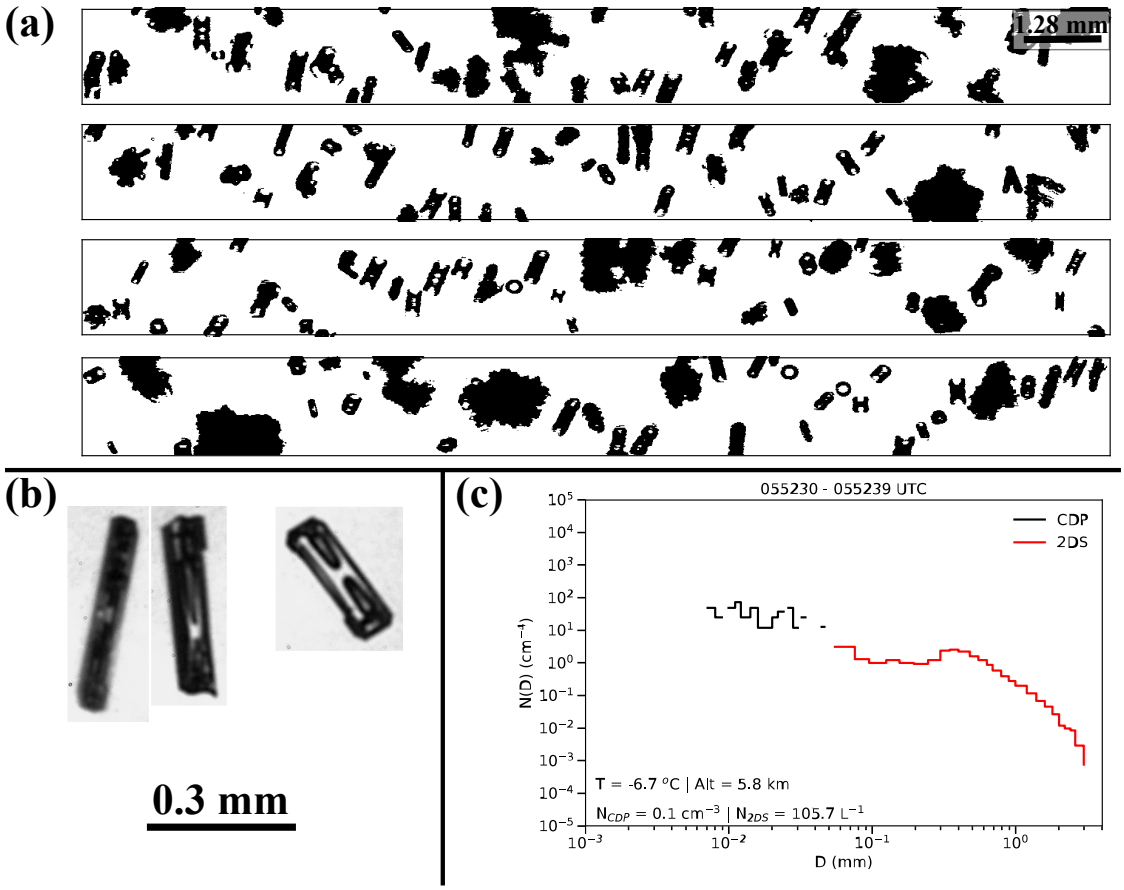

Figure 4.17: As in Fig. 4.7, but for area R4 in Fig. 4.15 (055230–055239 UTC 29 January). Note the different scale for the PHIPS images.

boundary.

Within the seeder region, ice crystals originating near cloud top at temperatures below -40 °C consisted of columns and bullet rosettes. At -20 °C, these columns and rosettes exhibited plate-like features consistent with previous laboratory studies (e.g., Bailey and Hallett, 2009). Vapor deposition was the primary growth process at -20 °C particularly for regions where SLW was negligible, such as within the frontal and anvil regions as the G-V returned to Hobart. A greater presence of SLW at the -10 °C flight level allowed for the riming of ice crystals, including capped columns and dendrites, as particles continued to fall within regions where the vertical velocities were small ($w < 1$ m s^{-1}). Regions of stronger updrafts were occasionally observed at the aircraft level and greater concentrations of supercooled droplets either formed or were transported from lower altitudes. Observations through the depth of the prefrontal band from -14 to 0 °C as the G-V returned from the Southern Ocean highlight changes in key microphysical processes. Ice multiplication within the Hallett-Mossop region (-8 to -3 °C) was suggested by the types of particles typically associated with the rime splintering process present and ice number concentrations increased from 5 to 175 L^{-1} as the aircraft descended. An increase in aggregation near the melting layer allowed particles to grow to 3 mm before

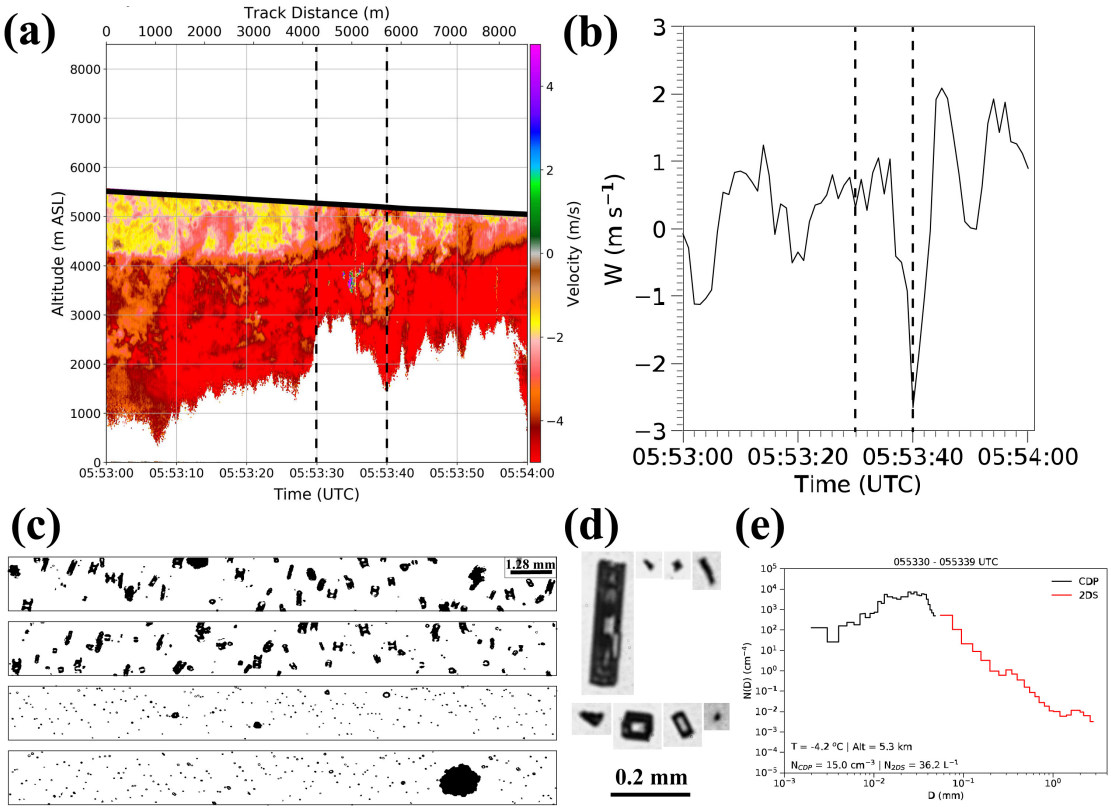

Figure 4.18: Similar to Fig. 4.9, but for area R5 in Fig. 4.15 (0553–0554 UTC 29 January).

melting as they fell into the mid-latitude-sourced feeder region.

Within the feeder region, surface moisture promoted the production of small droplets with mean concentrations of 47.2 ± 30.2 cm^{-3} that were collected by lower concentrations of larger drops. Drop growth to diameters larger than 3 mm through collision and coalescence continued as the hydrometeors precipitated towards the surface.

4.7 Conclusions

This chapter presented microphysical observations from a target-of-opportunity flight within an atmospheric river (AR) during the Southern Ocean Clouds, Radiation, Aerosol Transport Experimental Study (SOCRATES). The AR originated from northwest Australia at 10°S and flowed southeastward over Tasmania, Australia where the NSF/NCAR Gulfstream-V (G-V) High-performance Instrumented Airborne Platform for Environmental Research (HIAPER) aircraft made two passes through the AR during its departure from and return to Hobart airport. Measurements of reflectivity Z and vertical radial velocity V_r from the airborne, nadir-directed HIAPER cloud radar (HCR) provided detailed information on the fine-scale features of the prefrontal and frontal precipitation bands associated with the AR while a suite of microphysical instruments provided measurements of the concentration, size and morphological

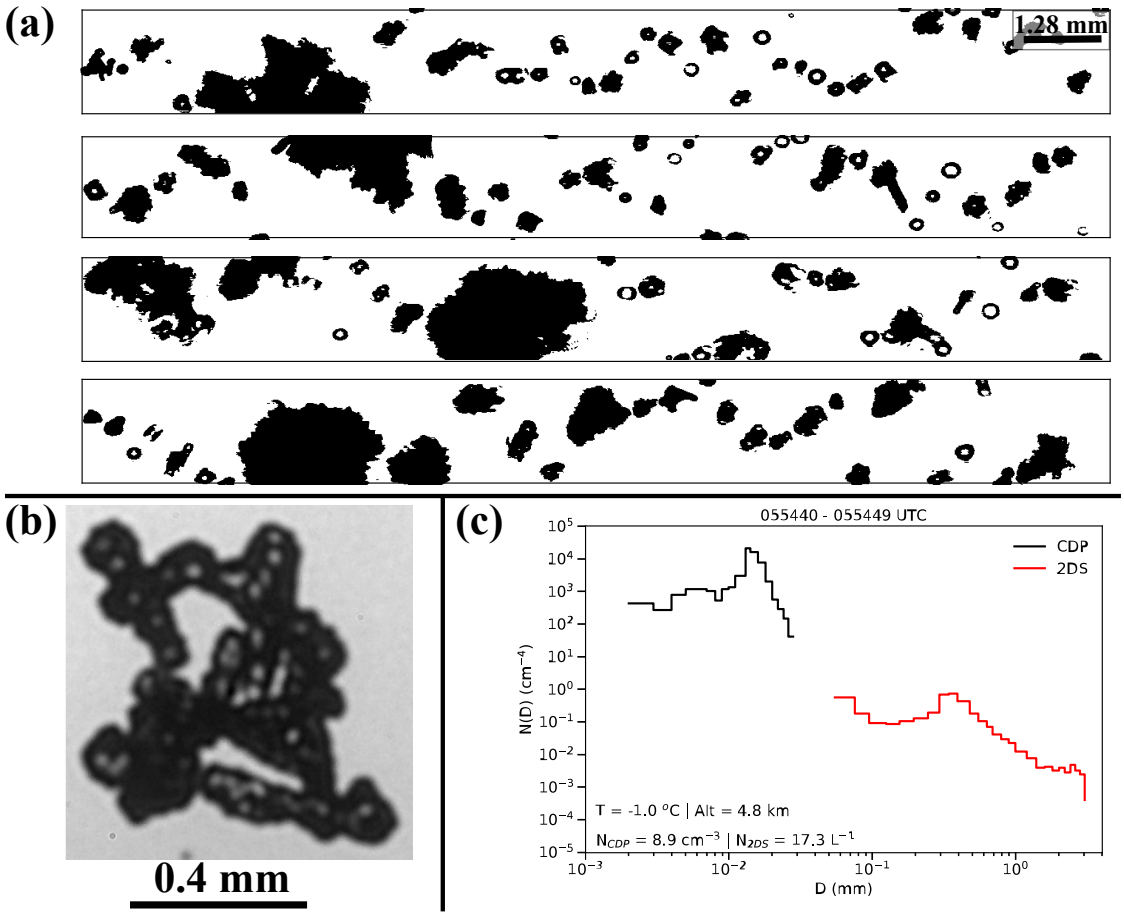

Figure 4.19: As in Fig. 4.7, but for area R6 in Fig. 4.15 (055440–055449 UTC 29 January).

properties of liquid- and ice-phase particles, and particle size distributions (PSDs) spanning from 1 μm to 3.2 mm.

A key finding of this study is that the distribution of particle sizes, shapes, and habits are closely tied to the dominant microphysical processes occurring for a given temperature and the vertical motions that transport these hydrometeors into the regions of cloud where measurements were made. The vertical evolution of microphysical characteristics within the AR and presence of a radar bright band in this study are consistent with observations from past AR studies where the seeder-feeder process was present (section 4.1). While many of these studies analyzed the seeder-feeder mechanism with respect to the influence of orographic lift within East Pacific ARs (e.g., White et al., 2003, 2015; Kingsmill et al., 2016), European ARs (Browning, 2018), and South American ARs (Viale et al., 2013), frontal-scale ascent can also produce a feeder region (Rutledge et al., 1983) as is the case with this event. Modeling results (Fan et al., 2014) during the CalWater experiment suggest that seeding by aerosols transported over large distances increased precipitation by 10–20% due to a 40% increase in ice production in the seeder region. Given that the AR in this study had tropical origins that traversed the Australian continent before entering the SOCRATES region of study (Part I), dust and other aerosols upwind of the G-V flight path could have played a role in seeding ice particles

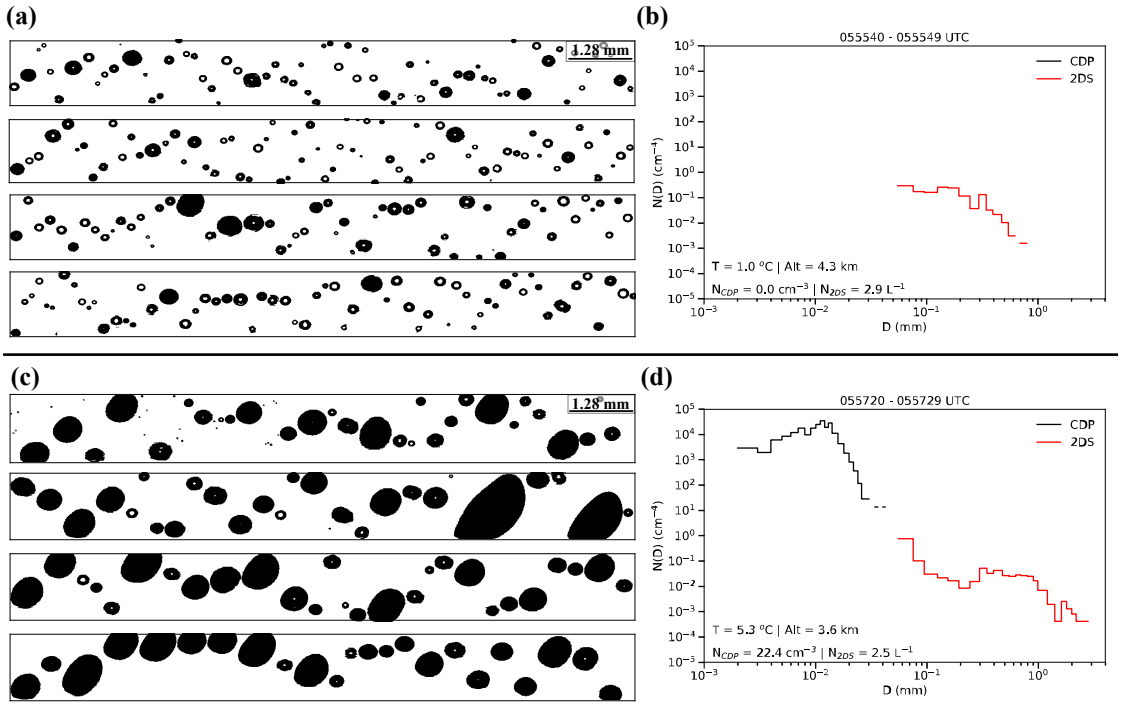

Figure 4.20: As in Fig. 4.7, but for area R7 in Fig. 4.6 (055540–055549 and 055720–055729 UTC 29 January).

aloft.

The particle sizes and habits tied to the microphysical processes presented here represent one of the first studies detailing the microphysical characteristics of a Southern Hemisphere AR at different depths through the cloud. Collocation of radar and microphysical data offers a unique link between the precipitation structure and microphysical properties of number concentration, particle sizes, and habit not widely available from previous AR field experiments. Further, simultaneous measurements from an airborne radar provide a complementary profile of the precipitation structure below the aircraft, signifying where regions of updrafts and downdrafts are present, the altitude at which the onset of melting occurs, and where more substantial liquid water attenuates the radar signal, among other things. Comparing the radar and microphysical observations provided in this study to future modeling studies of ARs in the Southern Hemisphere may highlight model shortcomings and offer improvements to the microphysical parameterizations specific to this region of the world.

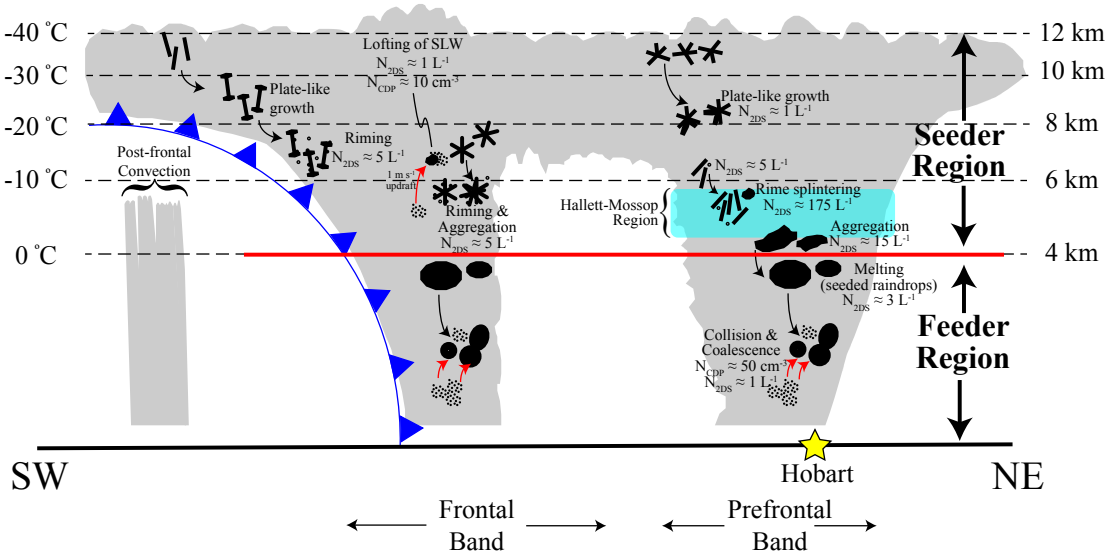

Figure 4.21: Schematic depicting the precipitation structure and processes observed within the AR. Number concentrations broadly represent values observed at the temperature indicated. Arrows denote the general transport of particles within the cloud.

Chapter 5

Conclusions

5.1 Overview of work

This dissertation focuses on (1) the development and implementation of a framework that considers multiple solutions from an ice particle mass-dimension relationship as equally valid for similar environments, and (2) the processes influencing the phase, habits, and distribution of particle sizes within a Southern Hemisphere AR. The key research questions pertaining to the first area of focus is (1) how temperature or other environmental variables, such as IWC, influence the set of a and b coefficients considered equally realizable for an m-D relationship and (2) how the variability in cloud conditions or the measurement uncertainties are related to these different environments and the m-D relations derived therein. The key research questions pertaining to the second area of focus is (1) how the microphysical properties within the seeder region of a Southern Hemisphere AR are linked to the microphysical processes and vertical motions within the cloud and (2) how the feeder region produces cloud droplets that promote raindrop growth through collision and coalescence to form the precipitation bands that were observed.

To answer the first research question, the approach of McFarquhar et al. (2015) was adapted for application to a and b parameters from an m-D relationship (Chapter 2). The technique allowed for a set of equally plausible a and b coefficients, represented as a surface in (a,b) phase space, to be derived for near-constant temperature flight legs for 3 events during MC3E. The technique was extended to 19 flights during MC3E, GCPEx, and OLYMPEX and m-D surfaces were derived for multiple ranges of temperature and IWC (Chapter 3). Analyses from both studies show that the co-variability of a and b and the variability of cloud conditions influence the range of a and b coefficients considered equally plausible for an environment.

To answer the second research question, a suite of airborne microphysical instruments measuring liquid water properties and sizes and shapes of particles were placed in the context of radar cross-sections of Z and V_{r}. Measurements of temperature, altitude, and vertical velocity were meaningful in explaining the temperatures where the observed particles may have originated and were placed into the context of typical habits that are observed at these temperatures. The vertical evolution of microphysical properties and presence of a radar bright band within the AR

are consistent with AR studies documenting the seeder-feeder process and complement the conclusions stated in the modeling study of Rauber et al. (2019) for the same AR event analyzed in chapter 4.

5.2 Contributions

Key advances in characterizing *m-D* relationships

The χ^2 minimization technique described in Chapters 2 and 3 is the first to employ an allowable tolerance considering the variability of cloud conditions and uncertainties due to statistical counting of particles and the measurements themselves. All *m-D* parameters with a χ^2 within the allowable tolerance of the minimum χ^2 should be regarded as equally plausible for an environment. These parameters, provided as a surface in (*a,b*) phase space, can be translated into probability distribution functions (PDFs) of *a* and *b* such that values closer to the centroid of the surface have a greater likelihood of begin chosen at random from the distribution. Presentation of these parameters as a surface or PDF allow for the results to be implemented in a stochastic framework of a microphysical parameterization or remote sensing retrieval. This is further discussed in chapter 5.3.

Key advances in microphysical observations through an AR

The results presented in Chapter 4 represent a unique dataset among AR studies from a microphysical prospective, particularly in the Southern Ocean region. These observations provide insight into the microphysical processes occurring at various temperatures in the cloud, and are combined with data from a vertically-pointing, high-frequency radar to detail the fine-scale precipitation features. These results can be beneficial to modeling efforts in the Southern Ocean region and may highlight biases or deficiencies in the parameterizations.

5.3 Directions for future work

Applying *m-D* surfaces to a stochastic model framework

Given that a stochastic representation allows variability within a high-resolution numerical model to be represented in a physically-based manner, determining empirical parameters at random, such as *a* and *b* coefficients from an *m-D* relationship, is a viable step towards assessing potential improvement of simulated cloud properties.

Ongoing collaboration with scientists at the University of Illinois, Cooperative Institute for Mesoscale Meteorological Studies, National Center for Atmospheric Research, University of Utah, and the Pacific Northwest National Laboratory involves implementation of a stochastic framework within a version of the predicted particle properties (P3) microphysics scheme (Morrison and Milbrandt, 2015). The modeling study of Stanford et al. (2019) investigated

the impact of randomly selecting *m-D* and fall-speed–dimension *V-D* parameters from a prescribed range of values on the modeled simulations for MCS events during MC3E and compared the modeled fields to observed fields. Key takeaways from the study were that inclusion of natural variability in the *m-D* relationship may impact radiation budgets in climate models, and inclusion of natural variability in the *V-D* relationship may have hydrological impacts. Thus, implementation of *m-D* surfaces and an autocorrelation scale (Berner et al., 2015) determined using observational data is the next step in evaluating the stochastic framework in the P3 scheme. Future work on evaluating the spatial autocorrelation of bulk microphysical properties such as number concentration, IWC, and D_{mm} based on PSD measurements is also planned.

Evaluating the impact of ice nuclei on ARs over the Southern Ocean

The results presented in Chapter 4 highlight the usefulness of radar and microphysical measurements at various depths within an AR to examine the various microphysical processes that influence the concentration, size, and morphological characteristics of ice- and liquid-phase particles. However, the impact that low concentrations of ice nucleating particles (INPs) may have had on the seeder region of the AR was not addressed as it was beyond the scope of the study. Future modeling efforts that consider long-range aerosol transport from primarily tropical regions *and* low INP concentrations observed over the Southern Ocean (McCluskey et al., 2018) may address the aerosol impact on primary ice formation within the seeder region of ARs over the Southern Ocean.

References

Abdelmonem, A., E. Järvinen, D. Duft, E. Hirst, S. Vogt, T. Leisner, and M. Schnaiter, 2016: PHIPS–HALO: the airborne Particle Habit Imaging and Polar Scattering probe – Part 1: Design and operation. *Atmos. Meas. Tech.*, **9 (7)**, 3131–3144, doi:10.5194/amt-9-3131-2016.

Bailey, M. P., and J. Hallett, 2004: Growth Rates and Habits of Ice Crystals between -20° and -70°C. *J. Atmos. Sci.*, **61 (5)**, 514–544, doi:10.1175/1520-0469(2004)061<0514:GRAHOI>2.0.CO;2.

Bailey, M. P., and J. Hallett, 2009: A Comprehensive Habit Diagram for Atmospheric Ice Crystals: Confirmation from the Laboratory, AIRS II, and Other Field Studies. *J. Atmos. Sci.*, **66 (9)**, 2888–2899, doi:10.1175/2009JAS2883.1.

Bao, J.-W., S. A. Michelson, P. J. Neiman, F. M. Ralph, and J. M. Wilczak, 2006: Interpretation of Enhanced Integrated Water Vapor Bands Associated with Extratropical Cyclones: Their Formation and Connection to Tropical Moisture. *Mon. Weather Rev.*, **134 (4)**, 1063–1080, doi:10.1175/MWR3123.1.

Barnes, S. L., 1964: A Technique for Maximizing Details in Numerical Weather Map Analysis. *Journal of Applied Meteorology*, **3 (4)**, 396–409, doi:10.1175/1520-0450(1964)003<0396:ATFMDI>2.0.CO;2, URL http://journals.ametsoc.org/doi/abs/10.1175/1520-0450%281964%29003%3C0396%3AATFMDI%3E2.0.CO%3B2#.WKz-Eb_dSWU.mendeley.

Baumgardner, D., and J. E. Dye, 1983: The 1982 Cloud Particle Measurement Symposium 4-7 May 1982, Boulder, Colo. *Bull. Am. Meteorol. Soc.*, **64 (4)**, 366–370, doi:10.1175/1520-0477-64.4.366.

Baumgardner, D., and A. Korolev, 1997: Airspeed Corrections for Optical Array Probe Sample Volumes. *J. Atmos. Ocean. Technol.*, **14 (5)**, 1224–1229, doi:10.1175/1520-0426(1997)014<1224:ACFOAP>2.0.CO;2.

Baumgardner, D., and A. Rodi, 1989: Laboratory and Wind Tunnel Evaluations of the Rosemount Icing Detector. *J. Atmos. Ocean. Technol.*, **6 (6)**, 971–979, doi:10.1175/1520-0426(1989)006<0971:LAWTEO>2.0.CO;2.

Baumgardner, D., and Coauthors, 2017: Cloud Ice Properties: In Situ Measurement Challenges. *Meteorol. Monogr.*, **58**, 9.1–9.23, doi:10.1175/AMSMONOGRAPHS-D-16-0011.1.

Bergeron, T., 1950: Über der mechanismum der ausgeibigen Niederschläge. *Ber. Dtsch. Wetterdienstes*, **12**, 225–232.

Berner, J., and Coauthors, 2015: Increasing the Skill of Probabilistic Forecasts: Understanding Performance Improvements from Model-Error Representations. *Mon. Weather Rev.*, **143 (4)**, 1295–1320, doi:10.1175/MWR-D-14-00091.1, URL http://journals.ametsoc.org/doi/10.1175/MWR-D-14-00091.1.

Bringi, V. N., and V. Chandrasekar, 2001: *Polarimetric Doppler Weather Radar: Principles and Applications*. Cambridge University Press, URL http://books.google.com/books?id=KvJvfP9t5Y8C.

Bringi, V. N., V. Chandrasekar, N. Balakrishnan, and D. S. Zrnić, 1990: An Examination of Propagation Effects in Rainfall on Radar Measurements at Microwave Frequencies. *J. Atmos. Ocean. Technol.*, **7 (6)**, 829–840, doi:10.1175/1520-0426(1990)007<0829:AEOPEI>2.0.CO;2.

Brown, P. R. A., and P. N. Francis, 1995: Improved Measurements of the Ice Water Content in Cirrus Using a Total-Water Probe. *Journal of Atmospheric and Oceanic Technology*, **12 (2)**, 410–414, doi:10.1175/1520-0426(1995)012<0410:IMOTIW>2.0.CO;2, URL http://dx.doi.org/10.1175/1520-0426(1995)012%3C0410:IMOTIW%3E2.0.CO%5Cn2.

Browning, K., 2018: Atmospheric rivers in the U.K. *Bull. Am. Meteorol. Soc.*, **99 (6)**, 1108–1109, doi:10.1175/BAMS-D-17-0291.1.

Browning, K. A., and C. W. Pardoe, 1973: Structure of low-level jet streams ahead of mid-latitude cold fronts. *Q. J. R. Meteorol. Soc.*, **99 (422)**, 619–638, doi:10.1002/qj.49709942204.

Cannon, F., F. M. Ralph, A. M. Wilson, and D. P. Lettenmaier, 2017: GPM Satellite Radar Measurements of Precipitation and Freezing Level in Atmospheric Rivers: Comparison With Ground-Based Radars and Reanalyses. *J. Geophys. Res. Atmos.*, **122 (23)**, 12,747–12,764, doi:10.1002/2017JD027355.

Cazenave, F., M. Gosset, M. Kacou, M. Alcoba, E. Fontaine, C. Duroure, and B. Dolan, 2016: Characterization of Hydrometeors in Sahelian Convective Systems with an X-Band Radar and Comparison with In Situ Measurements. Part I: Sensitivity of Polarimetric Radar Particle Identification Retrieval and Case Study Evaluation. *Journal of Applied Meteorology and Climatology*, **55 (2)**, 231–249, doi:10.1175/JAMC-D-15-0013.1, URL http://dx.doi.org/10.1175/JAMC-D-15-0013.1.

Chase, R. J., and Coauthors, 2018: Evaluation of Triple-Frequency Radar Retrieval of Snowfall Properties Using Coincident Airborne In Situ Observations During OLYMPEX. *Geophys. Res. Lett.*, **45 (11)**, 5752–5760, doi:10.1029/2018GL077997.

Cober, S. G., G. A. Isaac, A. V. Korolev, S. G. Cober, G. A. Isaac, and A. V. Korolev, 2001: Assessing the Rosemount Icing Detector with In Situ Measurements. *J. Atmos. Ocean. Technol.*, **18 (4)**, 515–528, doi:10.1175/1520-0426(2001)018<0515:ATRIDW>2.0.CO;2.

Cotton, R. J., and Coauthors, 2013: The effective density of small ice particles obtained from in situ aircraft observations of mid-latitude cirrus. *Q. J. R. Meteorol. Soc.*, **139 (676)**, 1923–1934, doi:10.1002/qj.2058.

Crosier, J., and Coauthors, 2014: Microphysical properties of cold frontal rainbands. *Q. J. R. Meteorol. Soc.*, **140 (681)**, 1257–1268, doi:10.1002/qj.2206.

Delanoë, J., and R. J. Hogan, 2010: Combined CloudSat-CALIPSO-MODIS retrievals of the properties of ice clouds. *Journal of Geophysical Research*, **115 (D4)**, D00H29–D00H29, doi:10.1029/2009JD012346, URL http://doi.wiley.com/10.1029/2009JD012346.

Dettinger, M. D., F. M. Ralph, T. Das, P. J. Neiman, and D. R. Cayan, 2011: Atmospheric Rivers, Floods and the Water Resources of California. *Water*, **3 (4)**, 445–478, doi:10.3390/w3020445.

Ellis, S., E. Loew, C. Burghart, P. Tsai, M. Dixon, J. Vivekanandan, and W.-C. Lee, 2017: Use of the Earth's Surface As a Reference to Correct Airborne Radar Radial Velocity Measurements for Platform Motion. *38th Conf. Radar Meteorol.*, American Meteorological Society, Chicago, IL, URL https://ams.confex.com/ams/38RADAR/webprogram/Paper321171.html.

Erfani, E., and D. L. Mitchell, 2016: Developing and bounding ice particle mass- and area-dimension expressions for use in atmospheric models and remote sensing. *Atmospheric Chemistry and Physics*, **16 (7)**, 4379–4400, doi:10.5194/acp-16-4379-2016, URL http://www.atmos-chem-phys.net/16/4379/2016/.

Fan, J., and Coauthors, 2014: Aerosol impacts on California winter clouds and precipitation during CalWater 2011: local pollution versus long-range transported dust. *Atmos. Chem. Phys.*, **14 (1)**, 81–101, doi:10.5194/acp-14-81-2014.

Field, P. R., 1999: Aircraft Observations of Ice Crystal Evolution in an Altostratus Cloud. *J. Atmos. Sci.*, **56 (12)**, 1925–1941, doi:10.1175/1520-0469(1999)056<1925:AOOICE>2.0.CO;2.

Field, P. R., A. J. Heymsfield, and A. Bansemer, 2006: Shattering and Particle Interarrival Times Measured by Optical Array Probes in Ice Clouds. *J. Atmos. Ocean. Technol.*, **23 (10)**, 1357–1371, doi:10.1175/JTECH1922.1.

Field, P. R., R. Wood, P. R. A. Brown, P. H. Kaye, E. Hirst, R. Greenaway, and J. A. Smith, 2003: Ice Particle Interarrival Times Measured with a Fast FSSP. *J. Atmos. Ocean. Technol.*, **20 (2)**, 249–261, doi:10.1175/1520-0426(2003)020<0249:IPITMW>2.0.CO;2.

Field, P. R., and Coauthors, 2016: Chapter 7. Secondary Ice Production - current state of the science and recommendations for the future. *Meteorol. Monogr.*, AMSMONOGRAPHS–D–16–0014.1, doi:10.1175/AMSMONOGRAPHS-D-16-0014.1.

Finlon, J. A., G. M. McFarquhar, S. W. Nesbitt, R. M. Rauber, H. Morrison, W. Wu, and P. Zhang, 2019: A novel approach to characterize the variability in mass-Dimension relationships: results from MC3E. *Atmos. Chem. Phys.*, **19 (6)**, 3621–3643, doi:10.5194/acp-2018-795.

Finlon, J. A., G. M. McFarquhar, R. M. Rauber, D. M. Plummer, B. F. Jewett, D. Leon, and K. R. Knupp, 2016: A Comparison of X-Band Polarization Parameters with In Situ Microphysical Measurements in the Comma Head of Two Winter Cyclones. *J. Appl. Meteorol. Climatol.*, **55 (12)**, 2549–2574, doi:10.1175/JAMC-D-16-0059.1.

Fontaine, E., A. Schwarzenboeck, J. Delanoë, W. Wobrock, D. Leroy, R. Dupuy, C. Gourbeyre, and A. Protat, 2014: Constraining mass-diameter relations from hydrometeor images and cloud radar reflectivities in tropical continental and oceanic convective anvils. *Atmos. Chem. Phys.*, **14 (20)**, 11 367–11 392, doi:10.5194/acp-14-11367-2014.

Fridlind, A. M., and Coauthors, 2017: Derivation of aerosol profiles for MC3E convection studies and use in simulations of the 20 May squall line case. *Atmos. Chem. Phys.*, **17 (9)**, 5947–5972, doi:10.5194/acp-17-5947-2017.

Gettelman, A., and Coauthors, 2010: Global simulations of ice nucleation and ice supersaturation with an improved cloud scheme in the Community Atmosphere Model. *J. Geophys. Res.*, **115 (D18)**, D18 216, doi:10.1029/2009JD013797.

Giangrande, S. E., T. Toto, A. Bansemer, M. R. Kumjian, S. Mishra, and A. V. Ryzhkov, 2016: Insights into riming and aggregation processes as revealed by aircraft, radar, and disdrometer observations for a 27 April 2011 widespread precipitation event. *Journal of Geophysical Research: Atmospheres*, **121 (10)**, 5846–5863, doi:10.1002/2015JD024537, URL https://agupubs.onlinelibrary.wiley.com/doi/abs/10.1002/2015JD024537.

Hallett, J., 2003: *Handbook of Weather, Climate, and Water*. John Wiley & Sons, Inc., Hoboken, NJ, USA, doi:10.1002/0471721603, URL http://onlinelibrary.wiley.com/resolve/doi?DOI=10.1002%2F0471721603.ch35#.WKnnG2yKXto.mendeley.

Hallett, J., and S. C. Mossop, 1974: Production of secondary ice particles during the riming process. *Nature*, **249 (5452)**, 26–28, doi:10.1038/249026a0.

Hassan, D., P. A. Taylor, and G. A. Isaac, 2017: Snowfall rate estimation using C-band polarimetric radars. *Meteorol. Appl.*, **24 (1)**, 142–156, doi:10.1002/met.1613.

Helmus, J., and S. Collis, 2016: The Python ARM Radar Toolkit (Py-ART), a Library for Working with Weather Radar Data in the Python Programming Language. *Journal of Open Research Software*, **4 (1)**, doi:10.5334/jors.119, URL http://openresearchsoftware.metajnl.com/articles/10.5334/jors.119/.

Heymsfield, A., 1972: Ice Crystal Terminal Velocities. *Journal of the Atmospheric Sciences*, **29 (7)**, 1348–1357, doi:10.1175/1520-0469(1972)029<1348:ICTV>2.0.CO;2.

Heymsfield, A. J., A. Bansemer, C. Schmitt, C. Twohy, and M. R. Poellot, 2004: Effective Ice Particle Densities Derived from Aircraft Data. *J. Atmos. Sci.*, **61 (9)**, 982–1003, doi:10.1175/1520-0469(2004)061<0982:EIPDDF>2.0.CO;2.

Heymsfield, A. J., A. Bansemer, and C. H. Twohy, 2007: Refinements to Ice Particle Mass Dimensional and Terminal Velocity Relationships for Ice Clouds. Part I: Temperature Dependence. *J. Atmos. Sci.*, **64 (4)**, 1047–1067, doi:10.1175/JAS3890.1.

Heymsfield, A. J., and D. Baumgardner, 1985: Summary of a workshop on processing 2–D probe data. *Bull. Am. Meteorol. Soc.*, **66 (4)**, 437–440.

Heymsfield, A. J., P. R. Field, M. Bailey, D. Rogers, J. Stith, C. Twohy, Z. Wang, and S. Haimov, 2011: Ice in Clouds Experiment—Layer Clouds. Part I: Ice Growth Rates Derived from Lenticular Wave Cloud Penetrations. *J. Atmos. Sci.*, **68 (11)**, 2628–2654, doi:10.1175/JAS-D-11-025.1.

Heymsfield, A. J., S. Lewis, A. Bansemer, J. Iaquinta, L. M. Miloshevich, M. Kajikawa, C. Twohy, and M. R. Poellot, 2002: A General Approach for Deriving the Properties of Cirrus and Stratiform Ice Cloud Particles. *Journal of the Atmospheric Sciences*, **59 (1)**, 3–29, doi:10.1175/1520-0469(2002)059<0003:AGAFDT>2.0.CO;2, URL http://dx.doi.org/10.1175/1520-0469(2002)059%3C0003:AGAFDT%3E2.0.CO.

Heymsfield, A. J., C. Schmitt, and A. Bansemer, 2013: Ice Cloud Particle Size Distributions and Pressure-Dependent Terminal Velocities from In Situ Observations at Temperatures from 0° to -86°C. *J. Atmos. Sci.*, **70 (12)**, 4123–4154, doi:10.1175/JAS-D-12-0124.1.

Heymsfield, A. J., C. Schmitt, A. Bansemer, and C. H. Twohy, 2010: Improved Representation of Ice Particle Masses Based on Observations in Natural Clouds. *J. Atmos. Sci.*, **67 (10)**, 3303–3318, doi:10.1175/2010JAS3507.1.

Hobbs, P. V., and A. L. Rangno, 1998: Microstructures of low and middle-level clouds over the Beaufort Sea. *Q. J. R. Meteorol. Soc.*, **124 (550)**, 2035–2071, doi:10.1002/qj.49712455012.

Hogan, R. J., A. J. Illingworth, and H. Sauvageot, 2000: Measuring crystal size in cirrus using 35- and 94-GHz radars. *Journal of Atmospheric and Oceanic Technology*, **17 (1)**, 27–37, doi:10.1175/1520-0426(2000)017<0027:MCSICU>2.0.CO;2.

Hogan, R. J., M. P. Mittermaier, and A. J. Illingworth, 2006: The Retrieval of Ice Water Content from Radar Reflectivity Factor and Temperature and Its Use in Evaluating a Mesoscale Model. *J. Appl. Meteorol. Climatol.*, **45 (2)**, 301–317, doi:10.1175/JAM2340.1.

Hogan, R. J., L. Tian, P. R. a. Brown, C. D. Westbrook, A. J. Heymsfield, and J. D. Eastment, 2012: Radar Scattering from Ice Aggregates Using the Horizontally Aligned Oblate Spheroid Approximation. *J. Appl. Meteorol. Climatol.*, **51 (3)**, 655–671, doi:10.1175/JAMC-D-11-074.1.

Houze, R. A., and Coauthors, 2017: The Olympic Mountains Experiment (OLYMPEX). *Bull. Am. Meteorol. Soc.*, **98 (10)**, 2167–2188, doi:10.1175/BAMS-D-16-0182.1.

Ice, R. L., A. K. Heck, J. G. Cunningham, W. D. Zittel, R. R. Lee, L. M. Richardson, and B. J. McGuire, 2015: Polarimetric Weather Radar Calibration Using Solar Scans. *31st Conf. Environ. Inf. Process. Technol.*, American Meteorological Society, Phoenix, AZ, 11.4, URL https://ams.confex.com/ams/95Annual/webprogram/Paper262780.html.

Ice, R. L., and Coauthors, 2017: Monitoring the Performance of the Polarimetric WSR-88D–Calibration and Sensitivity. *33rd Conf. Environ. Inf. Process. Technol.*, American Meteorological Society, Seattle, WA, 9A.2, URL https://ams.confex.com/ams/97Annual/webprogram/Paper302880.html.

Intergovernmental Panel on Climate Change, 2014: *Clouds and Aerosols*, 571–658. Cambridge University Press, doi:10.1017/CBO9781107415324.016.

International Telecommunication Union, 2013: Attenuation by atmospheric gases. Recommendation ITU-R P.676-10, Radiocommunication Sector of International Telecommunication Union. URL https://www.itu.int/dms_pubrec/itu-r/rec/p/R-REC-P.676-10-201309-S!!PDF-E.pdf, retrieved March 25, 2019.

Jackson, R. C., G. M. Mcfarquhar, J. Stith, M. Beals, R. A. Shaw, J. Jensen, J. Fugal, and A. Korolev, 2014: An Assessment of the Impact of Antishattering Tips and Artifact Removal Techniques on Cloud Ice Size Distributions Measured by the 2D Cloud Probe. *J. Atmos. Ocean. Technol.*, **31 (12)**, 2567–2590, doi:10.1175/JTECH-D-13-00239.1.

Jackson, R. C., and Coauthors, 2012: The dependence of ice microphysics on aerosol concentration in arctic mixed-phase stratus clouds during ISDAC and M-PACE. *J. Geophys. Res. Atmos.*, **117 (D15)**, doi:10.1029/2012JD017668.

Järvinen, E., and Coauthors, 2016: Quasi-Spherical Ice in Convective Clouds. *J. Atmos. Sci.*, **73 (10)**, 3885–3910, doi:10.1175/JAS-D-15-0365.1.

Jensen, M. P., S. E. Giangrande, and P. Kollias, 2014: The Mid-latitude Continental Convective Clouds Experiment (MC3E) Final Campaign Report. Tech. Rep. April, DOE Atmospheric Radiation Measurement, 1–13 pp. URL https://www.arm.gov/publications/programdocs/doe-sc-arm-14-012.pdf.

Jensen, M. P., and Coauthors, 2016: The Midlatitude Continental Convective Clouds Experiment (MC3E). *Bull. Am. Meteorol. Soc.*, **97 (9)**, 1667–1686, doi:10.1175/BAMS-D-14-00228.1.

Kingsmill, D. E., P. J. Neiman, F. M. Ralph, and A. B. White, 2006: Synoptic and Topographic Variability of Northern California Precipitation Characteristics in Landfalling Winter Storms Observed during CALJET. *Mon. Weather Rev.*, **134 (8)**, 2072–2094, doi:10.1175/MWR3166.1.

Kingsmill, D. E., P. J. Neiman, and A. B. White, 2016: Microphysics Regime Impacts on the Relationship between Orographic Rain and Orographic Forcing in the Coastal Mountains of Northern California. *J. Hydrometeorol.*, **17 (11)**, 2905–2922, doi:10.1175/JHM-D-16-0103.1.

Knippertz, P., H. Wernli, and G. Gläser, 2013: A global climatology of tropical moisture exports. *J. Clim.*, **26 (10)**, 3031–3045, doi:10.1175/JCLI-D-12-00401.1.

Knollenberg, R. G., and R. G. Knollenberg, 1970: The Optical Array: An Alternative to Scattering or Extinction for Airborne Particle Size Determination. *J. Appl. Meteorol.*, **9 (1)**, 86–103, doi:10.1175/1520-0450(1970)009<0086:TOAAAT>2.0.CO;2.

Korolev, A., E. Emery, and K. Creelman, 2013a: Modification and Tests of Particle Probe Tips to Mitigate Effects of Ice Shattering. *J. Atmos. Ocean. Technol.*, **30 (4)**, 690–708, doi:10.1175/JTECH-D-12-00142.1.

Korolev, A., and P. R. Field, 2015: Assessment of the performance of the inter-arrival time algorithm to identify ice shattering artifacts in cloud particle probe measurements. *Atmospheric Measurement Techniques*, **8 (2)**, 761–777, doi:10.5194/amt-8-761-2015, URL http://www.atmos-meas-tech.net/8/761/2015/.

Korolev, A., J. W. Strapp, G. A. Isaac, and E. Emery, 2013b: Improved Airborne Hot-Wire Measurements of Ice Water Content in Clouds. *J. Atmos. Ocean. Technol.*, **30 (9)**, 2121–2131, doi:10.1175/JTECH-D-13-00007.1.

Korolev, A. V., E. F. Emery, J. W. Strapp, S. G. Cober, G. A. Isaac, M. Wasey, and D. Marcotte, 2011: Small Ice Particles in Tropospheric Clouds: Fact or Artifact? Airborne Icing Instrumentation Evaluation Experiment. *Bull. Am. Meteorol. Soc.*, **92 (8)**, 967–973, doi:10.1175/2010BAMS3141.1.

Korolev, A. V., J. W. Strapp, G. A. Isaac, A. V. Korolev, J. W. Strapp, and G. A. Isaac, 1998: Evaluation of the Accuracy of PMS Optical Array Probes. *J. Atmos. Ocean. Technol.*, **15 (3)**, 708–720, doi:10.1175/1520-0426(1998)015<0708:EOTAOP>2.0.CO;2.

Krajewski, W. F., and G. J. Ciach, 2003: Towards Probabilistic Quantitative Precipitation WSR88d Algorithms: Preliminary Studies and Problem Formulation. Tech. Rep. DG133W-02-CN-0089, NOAA/NWS. URL http://www.nws.noaa.gov/oh/hrl/papers/wsr88d/PQPE-Year1-FinalReport_v2.pdf.

Lance, S., C. A. Brock, D. Rogers, and J. A. Gordon, 2010: Water droplet calibration of the Cloud Droplet Probe (CDP) and in-flight performance in liquid, ice and mixed-phase clouds during ARCPAC. *Atmos. Meas. Tech.*, **3 (6)**, 1683–1706, doi:10.5194/amt-3-1683-2010.

Lavers, D. A., and G. Villarini, 2013: Atmospheric Rivers and Flooding over the Central United States. *J. Clim.*, **26 (20)**, 7829–7836, doi:10.1175/JCLI-D-13-00212.1.

Lawson, R. P., S. Woods, and H. Morrison, 2015: The Microphysics of Ice and Precipitation Development in Tropical Cumulus Clouds. *Journal of the Atmospheric Sciences*, **72 (6)**, 2429–2445, doi:10.1175/JAS-D-14-0274.1, URL https://journals.ametsoc.org/doi/10.1175/JAS-D-14-0274.1.

Lemke, H. M., and M. Quante, 1999: Backscatter characteristics of nonspherical ice crystals: Assessing the potential of polarimetric radar measurements. *Journal of Geophysical Research: Atmospheres*, **104 (D24)**, 31 739–31 751, doi:10.1029/1999JD900490, URL http://doi.wiley.com/10.1029/1999JD900490.

Leroy, D., E. Fontaine, A. Schwarzenboeck, and J. W. Strapp, 2016: Ice Crystal Sizes in High Ice Water Content Clouds. Part I: On the Computation of Median Mass Diameter from In Situ Measurements. *Journal of Atmospheric and Oceanic Technology*, **33 (11)**, 2461–2476, doi:10.1175/JTECH-D-15-0151.1, URL http://journals.ametsoc.org/doi/10.1175/JTECH-D-15-0151.1.

Li, L., G. M. Heymsfield, L. Tian, P. E. Racette, L. Li, G. M. Heymsfield, L. Tian, and P. E. Racette, 2005: Measurements of Ocean Surface Backscattering Using an Airborne 94-GHz Cloud Radar—Implication for Calibration of Airborne and Spaceborne W-Band Radars. *J. Atmos. Ocean. Technol.*, **22 (7)**, 1033–1045, doi:10.1175/JTECH1722.1.

Liebe, H. J., 1985: An updated model for millimeter wave propagation in moist air. *Radio Sci.*, **20 (5)**, 1069–1089, doi:10.1029/RS020i005p01069.

Liu, G., and J. a. Curry, 2000: Determination of Ice Water Path and Mass Median Particle Size Using Multichannel Microwave Measurements. *Journal of Applied Meteorology*, **39**, 1318–1329, doi:10.1175/1520-0450(2000)039<1318:DOIWPA>2.0.CO;2.

Locatelli, J. D., and P. V. Hobbs, 1974: Fall speeds and masses of solid precipitation particles. *Journal of Geophysical Research*, **79 (15)**, 2185–2197, doi:10.1029/JC079i015p02185, URL http://onlinelibrary.wiley.com/doi/10.1029/JC079i015p02185/abstract%5Cnhttp://onlinelibrary.wiley.com/store/10.1029/JC079i015p02185/asset/jgr14894.pdf?v=1&t=i1h8td42&s=bea840a363a286e28adb6368e5b7ef447d7e173f.

Ma, Z., Y.-H. Kuo, F. M. Ralph, P. J. Neiman, G. A. Wick, E. Sukovich, and B. Wang, 2011: Assimilation of GPS Radio Occultation Data for an Intense Atmospheric River with the NCEP Regional GSI System. *Mon. Weather Rev.*, **139 (7)**, 2170–2183, doi:10.1175/2011MWR3342.1.

Maahn, M., U. Löhnert, P. Kollias, R. C. Jackson, and G. M. McFarquhar, 2015: Developing and Evaluating Ice Cloud Parameterizations for Forward Modeling of Radar Moments Using in situ Aircraft Observations. *J. Atmos. Ocean. Technol.*, **32 (5)**, 880–903, doi:10.1175/JTECH-D-14-00112.1.

Magono, C., and C. W. Lee, 1966: Meteorological classification of natural snow crystals. *J. Fac. Sci., Hokkaido Univ., Ser. 7*, **2 (4)**, 321–335, URL http://hdl.handle.net/2115/8672.

Magono, C., and T. Nakamura, 1965: Aerodynamic Studies of Falling Snowflakes. *Journal of the Meteorological Society of Japan*, **43 (June)**, 139–147.

Maneewongvatana, S., and D. M. Mount, 1999: It's okay to be skinny, if your friends are fat. *4th Annual CGC Workshop on Computational Geometry*.

Marchand, R., and Coauthors, 2014: The Southern Ocean Clouds, Radiation Aerosol Transport Experimental Study (SOCRATES). Whitepaper, University of Washington, Seattle, WA. URL http://www.atmos.washington.edu/socrates/SOCRATES_white_paper_Final_Sep29_2014.pdf.

Martner, B. E., and Coauthors, 2008: Raindrop Size Distributions and Rain Characteristics in California Coastal Rainfall for Periods with and without a Radar Bright Band. *J. Hydrometeorol.*, **9 (3)**, 408–425, doi:10.1175/2007JHM924.1.

Mascio, J., and G. G. Mace, 2017: Quantifying uncertainties in radar forward models through a comparison between CloudSat and SPartICus reflectivity factors. *J. Geophys. Res. Atmos.*, **122 (3)**, 1665–1684, doi:10.1002/2016JD025183.

Mascio, J., Z. Xu, and G. G. Mace, 2017: The Mass-Dimensional Properties of Cirrus Clouds During TC4. *Journal of Geophysical Research: Atmospheres*, **122 (19)**, 10,402–10,417, doi:10.1002/2017JD026787, URL http://doi.wiley.com/10.1002/2017JD026787.

Matrosov, S. Y., 2007: Modeling Backscatter Properties of Snowfall at Millimeter Wavelengths. *Journal of the Atmospheric Sciences*, **64 (2003)**, 1727–1736, doi:10.1175/JAS3904.1, URL http://journals.ametsoc.org/doi/full/10.1175/JAS3904.1%5Cnhttp://journals.ametsoc.org/doi/pdf/10.1175/JAS3904.1.

Matrosov, S. Y., 2008: Assessment of Radar Signal Attenuation Caused by the Melting Hydrometeor Layer. *IEEE Transactions on Geoscience and Remote Sensing*, **46 (4)**, 1039–1047, doi:10.1109/TGRS.2008.915757.

Matrosov, S. Y., 2012: Observations of Wintertime U.S. West Coast Precipitating Systems with W-Band Satellite Radar and Other Spaceborne Instruments. *J. Hydrometeorol.*, **13 (1)**, 223–238, doi:10.1175/JHM-D-10-05025.1.

Matrosov, S. Y., 2013: Characteristics of Landfalling Atmospheric Rivers Inferred from Satellite Observations over the Eastern North Pacific Ocean. *Mon. Weather Rev.*, **141 (11)**, 3757–3768, doi:10.1175/MWR-D-12-00324.1.

Matrosov, S. Y., R. Cifelli, P. J. Neiman, and A. B. White, 2016: Radar Rain-Rate Estimators and Their Variability due to Rainfall Type: An Assessment Based on Hydrometeorology Testbed Data from the Southeastern United States. *J. Appl. Meteorol. Climatol.*, **55 (6)**, 1345–1358, doi:10.1175/JAMC-D-15-0284.1.

McCluskey, C. S., and Coauthors, 2018: Observations of Ice Nucleating Particles Over Southern Ocean Waters. *Geophys. Res. Lett.*, **45 (21)**, 11,989–11,997, doi:10.1029/2018GL079981.

McCumber, M., and Coauthors, 1991: Comparison of Ice-Phase Microphysical Parameterization Schemes Using Numerical Simulations of Tropical Convection. *Journal of Applied Meteorology*, **30 (7)**, 985–1004, doi:10.1175/1520-0450-30.7.985, URL http://journals.ametsoc.org/doi/abs/10.1175/1520-0450-30.7.985.

McFarquhar, G. M., J. A. Finlon, D. M. Stechman, W. Wu, R. C. Jackson, and M. Freer, 2018a: University of Illinois/Oklahoma Optical Array Probe (OAP) Processing Software. URL https://doi.org/10.5281/zenodo.1285969, doi:10.5281/zenodo.1285969.

McFarquhar, G. M., J. A. Finlon, D. M. Stechman, W. Wu, R. C. Jackson, and M. Freer, 2018b: University of Illinois/Oklahoma Optical Array Probe (OAP) Processing Software. Version 3.2, doi:10.5281/ZENODO.1285969.

McFarquhar, G. M., and A. J. Heymsfield, 1996: Microphysical Characteristics of Three Anvils Sampled during the Central Equatorial Pacific Experiment. *Journal of the Atmospheric Sciences*, **53 (17)**, 2401–2423, doi:10.1175/1520-0469(1996)053<2401:MCOTAS>2.0.CO;2, URL http://dx.doi.org/10.1175/1520-0469(1996)053%3C2401:MCOTAS%3E2.0.CO.

McFarquhar, G. M., T.-L. Hsieh, M. Freer, J. Mascio, and B. F. Jewett, 2015: The Characterization of Ice Hydrometeor Gamma Size Distributions as Volumes in N0–λ–μ Phase Space: Implications for Microphysical Process Modeling. *J. Atmos. Sci.*, **72 (2)**, 892–909, doi:10.1175/JAS-D-14-0011.1.

McFarquhar, G. M., M. S. Timlin, T. Nousiainen, and P. Yang, 2005: A New Representation of the Single-Scattering Properties for Mid-latitude Clouds and its Impacts. URL http://www.arm.gov/publications/proceedings/conf15/extended{_}abs/mcfarquhar{_}gm2.pdf?id=26.

McFarquhar, G. M., M. S. Timlin, R. M. Rauber, B. F. Jewett, J. A. Grim, and D. P. Jorgensen, 2007a: Vertical Variability of Cloud Hydrometeors in the Stratiform Region of Mesoscale Convective Systems and Bow Echoes. *Mon. Weather Rev.*, **135 (10)**, 3405–3428, doi:10.1175/MWR3444.1.

McFarquhar, G. M., G. Zhang, M. R. Poellot, G. L. Kok, R. McCoy, T. Tooman, A. Fridlind, and A. J. Heymsfield, 2007b: Ice properties of single-layer stratocumulus during the Mixed-Phase Arctic Cloud Experiment: 1. Observations. *J. Geophys. Res. Atmos.*, **112 (24)**, 1–19, doi:10.1029/2007JD008633.

McFarquhar, G. M., and Coauthors, 2017: Processing of Ice Cloud In Situ Data Collected by Bulk Water, Scattering, and Imaging Probes: Fundamentals, Uncertainties, and Efforts toward Consistency. *Meteorol. Monogr.*, **58**, 11.1–11.33, doi:10.1175/AMSMONOGRAPHS-D-16-0007.1.

Minnis, P., and Coauthors, 2008: Near-real time cloud retrievals from operational and research meteorological satellites. *SPIE Remote Sens. Clouds Atmos. XIII*, R. H. Picard, A. Comeron, K. Schäfer, A. Amodeo, and M. van Weele, Eds., International Society for Optics and Photonics, Vol. 7107, 710703, doi:10.1117/12.800344.

Minnis, P., and Coauthors, 2011: CERES Edition-2 Cloud Property Retrievals Using TRMM VIRS and Terra and Aqua MODIS Data—Part I: Algorithms. *IEEE Trans. Geosci. Remote Sens.*, **49 (11)**, 4374–4400, doi:10.1109/TGRS.2011.2144601.

Mitchell, D. L., 1996: Use of Mass- and Area-Dimensional Power Laws for Determining Precipitation Particle Terminal Velocities. *Journal of the Atmospheric Sciences*, **53 (12)**, 1710–1723, doi:10.1175/1520-0469(1996)053<1710:UOMAAD>2.0.CO;2.

Mitchell, D. L., and W. P. Arnott, 1994: A Model Predicting the Evolution of Ice Particle Size Spectra and Radiative Properties of Cirrus Clouds. Part II: Dependence of Absorption and Extinction on Ice Crystal Morphology. *Journal of the Atmospheric Sciences*, **51 (6)**, 817–832, doi:10.1175/1520-0469(1994)051<0817:AMPTEO>2.0.CO;2, URL https://journals.ametsoc.org/doi/abs/10.1175/1520-0469%281994%29051%3C0817%3AAMPTEO%3E2.0.CO%3B2.

Mitchell, D. L., R. Zhang, and R. L. Pitter, 1990: Mass-Dimensional Relationships for Ice Particles and the Influence of Riming on Snowfall Rates. *J. Appl. Meteorol.*, **29 (2)**, 153–163, doi:10.1175/1520-0450(1990)029<0153:MDRFIP>2.0.CO;2.

Moore, B. J., P. J. Neiman, F. M. Ralph, and F. E. Barthold, 2012: Physical Processes Associated with Heavy Flooding Rainfall in Nashville, Tennessee, and Vicinity during 1–2 May 2010: The Role of an Atmospheric River and Mesoscale Convective Systems*. *Mon. Weather Rev.*, **140 (2)**, 358–378, doi:10.1175/MWR-D-11-00126.1.

Morrison, H., J. Milbrandt, H. Morrison, and J. Milbrandt, 2011: Comparison of Two-Moment Bulk Microphysics Schemes in Idealized Supercell Thunderstorm Simulations. *Mon. Weather Rev.*, **139 (4)**, 1103–1130, doi:10.1175/2010MWR3433.1.

Morrison, H., and J. A. Milbrandt, 2015: Parameterization of Cloud Microphysics Based on the Prediction of Bulk Ice Particle Properties. Part I: Scheme Description and Idealized Tests. *J. Atmos. Sci.*, **72 (1)**, 287–311, doi:10.1175/JAS-D-14-0065.1.

Nakamura, J., U. Lall, Y. Kushnir, A. W. Robertson, and R. Seager, 2013: Dynamical Structure of Extreme Floods in the U.S. Midwest and the United Kingdom. *J. Hydrometeorol.*, **14 (2)**, 485–504, doi:10.1175/JHM-D-12-059.1.

Nakaya, U., and T. J. Terada, 1935: Simultaneous Observations of the Mass, Falling Velocity and Form of Individual Snow Crystals. *Journal of the Faculty of Science, Hokkaido Imperial University*, **1 (7)**, 191–200, URL http://hdl.handle.net/2115/34452.

Neiman, P. J., B. J. Moore, A. B. White, G. A. Wick, J. Aikins, D. L. Jackson, J. R. Spackman, and F. M. Ralph, 2016: An Airborne and Ground-Based Study of a Long-Lived and Intense Atmospheric River with Mesoscale Frontal Waves Impacting California during CalWater-2014. *Mon. Weather Rev.*, **144 (3)**, 1115–1144, doi:10.1175/MWR-D-15-0319.1.

Neiman, P. J., F. M. Ralph, G. A. Wick, Y.-H. Kuo, T.-K. Wee, Z. Ma, G. H. Taylor, and M. D. Dettinger, 2008a: Diagnosis of an Intense Atmospheric River Impacting the Pacific Northwest: Storm Summary and Offshore Vertical Structure Observed with COSMIC Satellite Retrievals. *Mon. Weather Rev.*, **136 (11)**, 4398–4420, doi:10.1175/2008MWR2550.1.

Neiman, P. J., F. M. Ralph, G. A. Wick, J. D. Lundquist, and M. D. Dettinger, 2008b: Meteorological Characteristics and Overland Precipitation Impacts of Atmospheric Rivers Affecting the West Coast of North America Based on Eight Years of SSM/I Satellite Observations. *J. Hydrometeorol.*, **9 (1)**, 22–47, doi:10.1175/2007JHM855.1.

Neiman, P. J., and Coauthors, 2017: An Analysis of Coordinated Observations from NOAA's Ronald H. Brown Ship and G-IV Aircraft in a Landfalling Atmospheric River over the North Pacific during CalWater-2015. *Mon. Weather Rev.*, **145 (9)**, 3647–3669, doi:10.1175/MWR-D-17-0055.1.

Nesbitt, S., N. Guy, T. Lang, A. Lyons, and J. Finlon, 2019: Airborne Weather Observation Toolkit (AWOT). URL https://doi.org/10.5281/zenodo.2587168{\#}.XIGOaMKkKx8.mendeley, doi:10.5281/ZENODO.2587168.

Nevzorov, A. N., 1980: Aircraft cloud water content meter. *Communications a la VIIIeme Conference Internationale sur la Physique des Nuages*, AIMPA, 701–703.

Olson, W. S., and Coauthors, 2016: The Microwave Radiative Properties of Falling Snow Derived from Nonspherical Ice Particle Models. Part II: Initial Testing Using Radar, Radiometer and In Situ Observations. *Journal of Applied Meteorology and Climatology*, **55 (3)**, 709–722, doi:10.1175/JAMC-D-15-0131.1, URL http://dx.doi.org/10.1175/JAMC-D-15-0131.1.

Park, S.-G. S.-G., and Coauthors, 2005: Correction of Radar Reflectivity and Differential Reflectivity for Rain Attenuation at X Band. Part I: Theoretical and Empirical Basis. *J. Atmos. Ocean. Technol.*, **22 (11)**, 1621–1632, doi:10.1175/JTECH1803.1.

Petersen, W. A., and M. R. Schwaller, 2008: Global Precipitation Mission (GPM) Ground Validation Science Implementation Plan. Tech. rep., NASA Goddard Space Flight Center, Greenbelt, Maryland, 1–37 pp. URL https://pmm.nasa.gov/resources/documents/gpm-ground-validation-science-implementation-plan.

Pruppacher, H. R., and J. D. Klett, 1997: *Microphysics of Clouds and Precipitation*. Kluwer Academic Press, 954 pp.

Purnell, D. J., D. J. Kirshbaum, D. J. Purnell, and D. J. Kirshbaum, 2018: Synoptic Control over Orographic Precipitation Distributions during the Olympics Mountains Experiment (OLYMPEX). *Mon. Weather Rev.*, **146 (4)**, 1023–1044, doi:10.1175/MWR-D-17-0267.1.

Ralph, F. M., M. C. L. Dettinger, M. M. Cairns, T. J. Galarneau, and J. Eylander, 2018: Defining "Atmospheric river" : How the glossary of meteorology helped resolve a debate. *Bull. Am. Meteorol. Soc.*, **99 (4)**, 837–839, doi:10.1175/BAMS-D-17-0157.1.

Ralph, F. M., P. J. Neiman, and R. Rotunno, 2005: Dropsonde Observations in Low-Level Jets over the Northeastern Pacific Ocean from CALJET-1998 and PACJET-2001: Mean Vertical-Profile and Atmospheric-River Characteristics. *Mon. Weather Rev.*, **133 (4)**, 889–910, doi:10.1175/MWR2896.1.

Ralph, F. M., P. J. Neiman, and G. A. Wick, 2004: Satellite and CALJET Aircraft Observations of Atmospheric Rivers over the Eastern North Pacific Ocean during the Winter of 1997/98. *Mon. Weather Rev.*, **132 (7)**, 1721–1745, doi:10.1175/1520-0493(2004)132<1721:SACAOO>2.0.CO;2.

Ralph, F. M., P. J. Neiman, G. A. Wick, S. I. Gutman, M. D. Dettinger, D. R. Cayan, and A. B. White, 2006: Flooding on California's Russian River: Role of atmospheric rivers. *Geophys. Res. Lett.*, **33 (13)**, 3–7, doi:10.1029/2006GL026689.

Ralph, F. M., and Coauthors, 2017: Dropsonde Observations of Total Integrated Water Vapor Transport within North Pacific Atmospheric Rivers. *J. Hydrometeorol.*, **18 (9)**, 2577–2596, doi:10.1175/JHM-D-17-0036.1.

Rauber, R. M., S. M. Ellis, J. Vivekanandan, J. Stith, W.-C. Lee, G. M. McFarquhar, B. F. Jewett, and A. Janiszeski, 2017: Finescale Structure of a Snowstorm over the Northeastern United States: A First Look at High-Resolution HIAPER Cloud Radar Observations. *Bull. Am. Meteorol. Soc.*, **98 (2)**, 253–269, doi:10.1175/BAMS-D-15-00180.1.

Rauber, R. M., H. Hu, F. Dominguez, S. W. Nesbitt, G. M. McFarquhar, T. Zaremba, and J. A. Finlon, 2019: Analysis of an atmospheric river over Australia and the Southern Ocean, Part II: Structure and tropical vs mid-latitude water vapor fluxes. *J. Atmos. Sci.*

Ruby Leung, L., and Y. Qian, 2009: Atmospheric rivers induced heavy precipitation and flooding in the western U.S. simulated by the WRF regional climate model. *Geophys. Res. Lett.*, **36 (3)**, 1–6, doi:10.1029/2008GL036445.

Rutledge, S. A., P. Hobbs, S. A. Rutledge, and P. Hobbs, 1983: The Mesoscale and Microscale Structure and Organization of Clouds and Precipitation in Midlatitude Cyclones. VIII: A Model for the "Seeder-Feeder" Process in Warm-Frontal Rainbands. *J. Atmos. Sci.*, **40 (5)**, 1185–1206, doi:10.1175/1520-0469(1983)040<1185:TMAMSA>2.0.CO;2.

Rutz, J. J., W. J. Steenburgh, and F. M. Ralph, 2014: Climatological Characteristics of Atmospheric Rivers and Their Inland Penetration over the Western United States. *Mon. Weather Rev.*, **142 (2)**, 905–921, doi:10.1175/MWR-D-13-00168.1.

Schmitt, C. G., and A. J. Heymsfield, 2010: The Dimensional Characteristics of Ice Crystal Aggregates from Fractal Geometry. *Journal of the Atmospheric Sciences*, **67 (5)**, 1605–1616, doi:10.1175/2009JAS3187.1, URL http://dx.doi.org/10.1175/2009JAS3187.1.

Skofronick-Jackson, G., and Coauthors, 2015: Global precipitation measurement cold season precipitation experiment (GCPEX): For measurement's sake, let it snow. *Bull. Am. Meteorol. Soc.*, **96 (10)**, 1719–1741, doi:10.1175/BAMS-D-13-00262.1.

Skofronick-Jackson, G., and Coauthors, 2017: The Global Precipitation Measurement (GPM) Mission for Science and Society. *Bull. Am. Meteorol. Soc.*, **98 (8)**, 1679–1695, doi:10.1175/BAMS-D-15-00306.1.

Sodemann, H., and A. Stohl, 2013: Moisture Origin and Meridional Transport in Atmospheric Rivers and Their Association with Multiple Cyclones. *Mon. Weather Rev.*, **141 (8)**, 2850–2868, doi:10.1175/MWR-D-12-00256.1.

Stanford, M. W., H. Morrison, A. Varble, J. Berner, W. Wu, G. M. McFarquhar, and J. A. Milbrandt, 2019: Sensitivity of Simulated Deep Convection to a Stochastic Ice Microphysics Framework. *J. Adv. Model. Earth Syst.*

Stoelinga, M. T., and Coauthors, 2003: Improvement of Microphysical Parameterization through Observational Verification Experiment. *Bull. Am. Meteorol. Soc.*, **84 (12)**, 1807–1826, doi:10.1175/BAMS-84-12-1807.

Szyrmer, W., and I. Zawadzki, 2010: Snow Studies. Part II: Average Relationship between Mass of Snowflakes and Their Terminal Fall Velocity. *Journal of the Atmospheric Sciences*, **67 (10)**, 3319–3335, doi:10.1175/2010JAS3390.1, URL http://journals.ametsoc.org/doi/abs/10.1175/2010JAS3390.1.

Trenberth, K. E., J. T. Fasullo, K. E. Trenberth, and J. T. Fasullo, 2010: Simulation of Present-Day and Twenty-First-Century Energy Budgets of the Southern Oceans. *J. Clim.*, **23 (2)**, 440–454, doi:10.1175/2009JCLI3152.1.

UCAR/NCAR - Earth Observing Laboratory, 2014: HIAPER Cloud Radar (HCR). Tech. rep., UCAR/NCAR - Earth Observing Laboratory. doi:10.5065/D6BP00TP, retrieved March 25, 2019.

UCAR/NCAR - Earth Observing Laboratory, 2018a: SOCRATES HCR noise source calibration. UCAR/NCAR - Earth Observing Laboratory, URL https://www.eol.ucar.edu/node/14065, retrieved March 25, 2019.

UCAR/NCAR - Earth Observing Laboratory, 2018b: SOCRATES HCR ocean scan calibration. UCAR/NCAR - Earth Observing Laboratory, URL https://www.eol.ucar.edu/node/14066, retrieved March 25, 2019.

Viale, M., R. A. Houze, and K. L. Rasmussen, 2013: Upstream Orographic Enhancement of a Narrow Cold-Frontal Rainband Approaching the Andes. *Mon. Weather Rev.*, **141 (5)**, 1708–1730, doi:10.1175/MWR-D-12-00138.1.

Waliser, D., and B. Guan, 2017: Extreme winds and precipitation during landfall of atmospheric rivers. *Nat. Geosci.*, **10 (3)**, 179–183, doi:10.1038/ngeo2894.

Wang, J., X. Dong, and B. Xi, 2015: Investigation of ice cloud microphysical properties of DCSs using aircraft in situ measurements during MC3E over the ARM SGP site. *J. Geophys. Res. Atmos.*, **120 (8)**, 3533–3552, doi:10.1002/2014JD022795.

Weickmann, H. K., 1945: Formen und Bildung atmosphaerischer Eiskristalle. *Beitr. Phys. Atmos.*, **28**, 12–52.

White, A. B., P. J. Neiman, F. M. Ralph, D. E. Kingsmill, and P. O. G. Persson, 2003: Coastal Orographic Rainfall Processes Observed by Radar during the California Land-Falling Jets Experiment. *J. Hydrometeorol.*, **4 (2)**, 264–282, doi:10.1175/1525-7541(2003)4<264:CORPOB>2.0.CO;2.

White, A. B., and Coauthors, 2015: The Impacts of California's San Francisco Bay Area Gap on Precipitation Observed in the Sierra Nevada during HMT and CalWater. *J. Hydrometeorol.*, **16 (3)**, 1048–1069, doi:10.1175/JHM-D-14-0160.1.

Wick, G. A., P. J. Neiman, and F. M. Ralph, 2013: Description and validation of an automated objective technique for identification and characterization of the integrated water vapor signature of atmospheric rivers. *IEEE Trans. Geosci. Remote Sens.*, **51 (4)**, 2166–2176, doi:10.1109/TGRS.2012.2211024.

Wu, W., and G. M. McFarquhar, 2016: On the Impacts of Different Definitions of Maximum Dimension for Nonspherical Particles Recorded by 2d Imaging Probes. *Journal of Atmospheric and Oceanic Technology*, **33 (5)**, 1057–1072, doi:10.1175/JTECH-D-15-0177.1, URL http://dx.doi.org/10.1175/JTECH-D-15-0177.1.

Xu, Z., and G. G. Mace, 2017: Ice Particle Mass–Dimensional Relationship Retrieval and Uncertainty Evaluation Using the Optimal Estimation Methodology Applied to the MACPEX Data. *Journal of Applied Meteorology and Climatology*, **56 (3)**, 767–788, doi:10.1175/JAMC-D-16-0222.1, URL http://journals.ametsoc.org/doi/10.1175/JAMC-D-16-0222.1.

Zagrodnik, J. P., L. A. McMurdie, and R. A. Houze, 2018: Stratiform Precipitation Processes in Cyclones Passing over a Coastal Mountain Range. *J. Atmos. Sci.*, **75 (3)**, 983–1004, doi:10.1175/JAS-D-17-0168.1.

Zhang, P., D. Zrnić, and A. Ryzhkov, 2013: Partial Beam Blockage Correction Using Polarimetric Radar Measurements. *J. Atmos. Ocean. Technol.*, **30 (5)**, 861–872, doi:10.1175/JTECH-D-12-00075.1.

Zhu, Y., and R. E. Newell, 1998: A Proposed Algorithm for Moisture Fluxes from Atmospheric Rivers. *Mon. Weather Rev.*, **126 (3)**, 725–735, doi:10.1175/1520-0493(1998)126<0725:APAFMF>2.0.CO;2.

Zikmunda, J., and G. Vali, 1972: Fall Patterns and Fall Velocities of Rimed Ice Crystals. *Journal of the Atmospheric Sciences*, **29 (7)**, 1334–1347, doi:10.1175/1520-0469(1972)029<1334:FPAFVO>2.0.CO;2.

Appendix A

List of variables and their descriptions

Table A.1: List of variables and their descriptions.

a	Prefactor component in mass-Dimension relationship
A	Particle cross-sectional area
b	Exponent component in mass-Dimension relationship
χ^2	Chi-square statistic for each (a,b) over a flight leg
${\chi^2}_{\min}$	Lowest χ^2 value in (a,b) phase space for a flight leg
$\Delta\chi_1^2$	Threshold determined from uncertainty in the particle size distribution due to sampling statistics
$\Delta\chi_2^2$	Threshold determined from combined uncertainty due to measurement errors
$\Delta\chi^2$	Maximum value of ${\chi^2}_{\min}$, $\Delta\chi_1^2$, or $\Delta\chi_2^2$
D	Particle maximum dimension
D_{mm}	Median mass diameter
IWC	Ice water content
J	Jaccard similarity coefficient
K_{DP}	Specific differential phase
$\lvert K_{\mathrm{ice}}\rvert^2$	Dielectric constant for ice
$\lvert K_w\rvert^2$	Dielectric constant for water
$M(D)$	Mass distribution function
N_{2DS}	Number concentration from the 2D-S for $0.15 \leq D \leq 3.2$ mm
N_{CDP}	Number concentration from the CDP for $1 \leq D \leq 50$ μm
$N(D)$	Number distribution function
N_{t}	Total number concentration
ρ_e	Effective density
T	Environmental temperature
TWC	Total water content measurement
TWC_{diff}	Measure of normalized difference between the Nevzorov *TWC* and that derived from the $N(D)$ for a given (a,b) defined by Eq. (2.3)
TWC_{SD}	*TWC* derived from the $N(D)$ for a given (a,b)
V_{r}	Radial velocity
w	Vertical velocity measurement
ζ	Particle sphericity
Z	Radar reflectivity factor
$Z_c(D)$	Cumulative reflectivity distribution function up to size D'
$Z(D)$	Reflectivity distribution function
Z_{diff}	Measure of normalized difference between the radar Z and that derived from the $N(D)$ for a given (a,b) defined by Eq. (2.4)
Z_{DR}	Differential reflectivity
Z_{SD}	Z derived from the $N(D)$ for a given (a,b)
Z_t	Derived total reflectivity from the mean $N(D)$ for a given (a,b)